



CHALMERS
UNIVERSITY OF TECHNOLOGY

Volume Density Structure of the Central Molecular Zone NGC 253 through ALCHEMI Excitation Analysis

Downloaded from: <https://research.chalmers.se>, 2024-05-05 22:27 UTC

Citation for the original published paper (version of record):

Tanaka, K., Mangum, J., Viti, S. et al (2024). Volume Density Structure of the Central Molecular Zone NGC 253 through ALCHEMI Excitation Analysis. *Astrophysical Journal*, 961(1). <http://dx.doi.org/10.3847/1538-4357/ad0e64>

N.B. When citing this work, cite the original published paper.



Volume Density Structure of the Central Molecular Zone NGC 253 through ALCHEMI Excitation Analysis

Kunihiko Tanaka¹, Jeffrey G. Mangum², Serena Viti^{3,4}, Sergio Martín^{5,6}, Nanase Harada^{7,8,9}, Kazushi Sakamoto⁸,
Sebastien Muller¹⁰, Yuki Yoshimura¹¹, Kouichiro Nakanishi^{7,9}, Rubén Herrero-Illana^{5,12}, Kimberly L. Emig^{2,22},
S. Mühle¹³, Hiroyuki Kaneko^{14,15}, Tomoka Tosaki¹⁵, Erica Behrens¹⁶, Víctor M. Rivilla^{17,18}, Laura Colzi¹⁷,
Yuri Nishimura^{7,11}, P. K. Humire¹⁹, Mathilde Bouvier³, Ko-Yun Huang³, Joshua Butterworth³,
David S. Meier^{20,21}, and Paul P. van der Werf³

¹ Department of Physics, Faculty of Science and Technology, Keio University, 3-14-1 Hiyoshi, Yokohama, Kanagawa 223-8522, Japan; ktanaka@phys.keio.ac.jp

² National Radio Astronomy Observatory, 520 Edgemont Road, Charlottesville, VA 22903-2475, USA

³ Leiden Observatory, Leiden University, P.O. Box 9513, 2300 RA Leiden, The Netherlands

⁴ Department of Physics and Astronomy, University College London, Gower Street, London WC1E6BT, UK

⁵ European Southern Observatory, Alonso de Córdova, 3107, Vitacura, Santiago 763-0355, Chile

⁶ Joint ALMA Observatory, Alonso de Córdova, 3107, Vitacura, Santiago 763-0355, Chile

⁷ National Astronomical Observatory of Japan, 2-21-1 Osawa, Mitaka, Tokyo 181-8588, Japan

⁸ Institute of Astronomy and Astrophysics, Academia Sinica, 11F of AS/NTU Astronomy-Mathematics Building, No.1, Sec. 4, Roosevelt Road, Taipei 10617, Taiwan

⁹ Department of Astronomy, School of Science, The Graduate University for Advanced Studies (SOKENDAI), 2-21-1 Osawa, Mitaka, Tokyo 181-8555, Japan

¹⁰ Department of Space, Earth and Environment, Chalmers University of Technology, Onsala Space Observatory, SE-43992 Onsala, Sweden

¹¹ Institute of Astronomy, Graduate School of Science, The University of Tokyo, 2-21-1 Osawa, Mitaka, Tokyo 181-0015, Japan

¹² Institute of Space Sciences (ICE, CSIC), Campus UAB, Carrer de Magrans, E-08193 Barcelona, Spain

¹³ Argelander-Institut für Astronomie, Universität Bonn, Auf dem Hügel 71, D-53121 Bonn, Germany

¹⁴ Institute of Science and Technology, Niigata University, 8050 Ikarashi 2-no-cho, Nishi-ku, Niigata 950-2181, Japan

¹⁵ Joetsu University of Education, 1, Yamayashiki-machi, Joetsu, Niigata 943-8512, Japan

¹⁶ Department of Astronomy, University of Virginia, P.O. Box 400325, 530 McCormick Road, Charlottesville, VA 22904-4325, USA

¹⁷ Centro de Astrobiología (CSIC-INTA), Ctra. de Ajalvir Km. 4, Torrejón de Ardoz, E-28850 Madrid, Spain

¹⁸ INAF-Osservatorio Astrofisico di Arcetri, Largo Enrico Fermi 5, I-50125, Florence, Italy

¹⁹ Max-Planck-Institut für Radioastronomie, Auf dem Hügel 69, D-53121 Bonn, Germany

²⁰ New Mexico Institute of Mining and Technology, 801 Leroy Place, Socorro, NM 87801, USA

²¹ National Radio Astronomy Observatory, P.O. Box O, 1003 Lopezville Road, Socorro, NM 87801, USA

Received 2023 September 1; revised 2023 November 15; accepted 2023 November 19; published 2024 January 11

Abstract

We present a spatially resolved excitation analysis for the central molecular zone (CMZ) of the starburst galaxy NGC 253 using the data from the Atacama Large Millimeter/submillimeter Array Comprehensive High-resolution Extragalactic Molecular Inventory, whereby we explore parameters distinguishing NGC 253 from the quiescent Milky Way's Galactic center (GC). Non-LTE analyses employing a hierarchical Bayesian framework are applied to Band 3–7 transitions from nine molecular species to delineate the position–position–velocity distributions of column density (N_{H_2}), volume density (n_{H_2}), and temperature (T_{kin}) at 27 pc resolution. Two distinct components are detected: a low-density component with ($n_{\text{H}_2}, T_{\text{kin}}$) $\sim (10^{3.3} \text{ cm}^{-3}, 85 \text{ K})$ and a high-density component with ($n_{\text{H}_2}, T_{\text{kin}}$) $\sim (10^{4.4} \text{ cm}^{-3}, 110 \text{ K})$, separated at $n_{\text{H}_2} \sim 10^{3.8} \text{ cm}^{-3}$. NGC 253 has ~ 10 times the high-density gas mass and ~ 3 times the dense-gas mass fraction of the GC. These properties are consistent with their HCN/CO ratio but cannot alone explain the factor of ~ 30 difference in their star formation efficiencies (SFEs), contradicting the dense-gas mass to star formation rate scaling law. The n_{H_2} histogram toward NGC 253 exhibits a shallow declining slope up to $n_{\text{H}_2} \sim 10^6 \text{ cm}^{-3}$, while that of the GC steeply drops in $n_{\text{H}_2} \gtrsim 10^{4.5} \text{ cm}^{-3}$ and vanishes at 10^5 cm^{-3} . Their dense-gas mass fraction ratio becomes consistent with their SFEs when the threshold n_{H_2} for the dense gas is taken at $\sim 10^{4.2-4.6} \text{ cm}^{-3}$. The rich abundance of gas above this density range in the NGC 253 CMZ, or its scarcity in the GC, is likely to be the critical difference characterizing the contrasting star formation in the centers of the two galaxies.

Unified Astronomy Thesaurus concepts: Star formation (1569); Giant molecular clouds (653); Starburst galaxies (1570); Galactic center (565); Interstellar medium (847)

1. Introduction

NGC 253 is an archetypal starburst galaxy in the nearby universe, whose relative closeness ($D = 3.5 \text{ Mpc}$; Rekola et al.

2005) makes it an ideal target to study the physical and chemical environments for highly active star formation (SF). In particular, a comparison between the central molecular zone (CMZ) of NGC 253 and the Galactic center (GC) of the Milky Way (MW) provides insights into the conditions distinguishing starburst and quiescent galaxies (Paglione et al. 1995; Sakamoto et al. 2011; Leroy et al. 2015; Krieger et al. 2020). While they exhibit contrasting SF activities, they are similar in total stellar mass (Bailin et al. 2011; Licquia & Newman 2015) and share many common physical characteristics. The

²² Jansky Fellow of the National Radio Astronomy Observatory.



molecular gas in their central region, and the giant molecular clouds (GMCs) in their central regions are both in a barred potential and characterized by high temperature and density (Nagai et al. 2007; Mangum et al. 2013, 2019; Rosenberg et al. 2014; Gorski et al. 2017; Pérez-Beaupuits et al. 2018; Tanaka et al. 2018), an elevated degree of turbulence (Tsuboi et al. 1999; Shetty et al. 2012; Rathborne et al. 2014; Krieger et al. 2020; Tanaka et al. 2020; Harada et al. 2022; Huang et al. 2023), and enhanced cosmic-ray ionization rate (CRIR; Oka et al. 2005; Goto et al. 2008; Belloche et al. 2013; Harada et al. 2021; Holdship et al. 2021, 2022; Behrens et al. 2022). However, the dense-gas content with molecular hydrogen volume density (n_{H_2}) of $\gtrsim 10^4 \text{ cm}^{-3}$ of the GC is dominated by quiescent gas lacking cluster formation, in stark contrast to the NGC 253 CMZ, which harbors 14 embedded young massive clusters (Leroy et al. 2018). The overall star formation rate (SFR) of the CMZ of NGC 253 is 2 orders of magnitude higher than that of the GC (Ott et al. 2005; Kauffmann et al. 2013), which is approximately an order of magnitude higher than the molecular gas mass ratio of the NGC 253 CMZ to the GC (Dahmen et al. 1998).

The dispersion of star formation efficiencies (SFEs) of molecular clouds and galaxies, where SFE refers to the SFR per unit molecular gas mass, are observationally related to the difference in dense-gas fraction (f_{DG}), which represents the mass fraction of gas immediately responsible for SF (Solomon et al. 1992; Gao & Solomon 2004; Lada et al. 2012). The HCN/CO luminosity ratio is the most commonly used measure of f_{DG} , as HCN 1–0 luminosity was considered to trace the dense-gas mass with $n_{\text{H}_2} \gtrsim 3 \times 10^4 \text{ cm}^{-3}$ (Gao & Solomon 2004; Lada et al. 2012). The HCN/CO ratio of NGC 253 is a few times that of the GC (Paglione et al. 1995; Sakamoto et al. 2011), being qualitatively consistent with the higher SFE of NGC 253. However, this difference in f_{DG} is still by an order of magnitude smaller than that in their difference in SFE, apparently contradicting the scaling relation between the dense-gas mass and SFR. This case with the NGC 253 CMZ and the GC can be regarded as a striking example of the ~ 1 dex dispersion of the SFR/HCN ratio among extragalactic sources (e.g., Usero et al. 2015; Bigiel et al. 2016; Gallagher et al. 2018; Jiménez-Donaire et al. 2019; Neumann et al. 2023). Such dispersion is attributed to the environmental dependence of the threshold n_{H_2} for SF based on the turbulent cloud model (e.g., Krumholz & McKee 2005) and deficiency of the HCN/CO ratio as an accurate measure of the dense-gas fraction (e.g., Kauffmann et al. 2017; Barnes et al. 2020; Jones et al. 2023).

Accurate measurement of n_{H_2} is crucial to addressing the above issues. Luminosity-based measurements of n_{H_2} based on multiline excitation analysis have been reported toward NGC 253 (Rosenberg et al. 2014; Pérez-Beaupuits et al. 2018; hereafter R14 and P18, respectively) and the GC (Nagai et al. 2007; Mills et al. 2018; Tanaka et al. 2018). These studies consistently indicate that both NGC 253 and the GC have multicomponent molecular gas consisting of a relatively low-density ($n_{\text{H}_2} \sim \text{a few } 10^3 \text{ cm}^{-3}$) component mainly traced by low- to mid- J CO lines and a higher-density ($n_{\text{H}_2} \sim \text{a few } 10^4\text{--}10^5 \text{ cm}^{-3}$) component visible in high-density tracers such as HCN and high- J CO lines. A multicomponent gas was also detected in measurements of the gas kinetic temperature (T_{kin}) both for NGC 253 (Mangum et al. 2013; Gorski et al. 2017) and for the GC (Arai et al. 2016) from excitation analysis of the

NH_3 inversion lines. However, the n_{H_2} values and mass fractions of the dense-gas components differ among the authors depending on the analysis method, the tracer lines used, and the spatial resolution, leaving the comparison of the dense-gas properties in NGC 253 and the GC not straightforward.

Further spatially resolved measurement of n_{H_2} was performed for the GC. Tanaka et al. (2018; hereafter T18) conducted spatially resolved excitation analysis using GC survey data of 13 transitions from nine molecular species (^{13}CO 2–1, HCN 1–0 and 4–3, H^{13}CN 1–0, HCO^+ 1–0, H^{13}CO^+ 1–0, HNC 1–0, $p - \text{H}_2\text{CO}$ $2_{0,2}-1_{0,1}$ and $3_{0,3}-2_{0,2}$, CS 2–1, N_2H^+ 1–0, SiO 2–1, and HC_3N 10–9). They constructed position–position–velocity (P – P – V) cubes of the physical condition parameters and molecular abundances at a spatial resolution of $60'' = 2.4 \text{ pc}$. They found that signatures of SF were limited to dense-gas clumps with typical $n_{\text{H}_2} \gtrsim 10^{4.6} \text{ cm}^{-3}$ and argued that the scarcity of such high-density clumps is one reason for the suppressed SF in the GC (Tanaka et al. 2020). For the NGC 253 CMZ, however, the previous n_{H_2} measurements (R14 and P18) were performed with the luminosity-based CO spectral line energy distribution (SLED), and hence the spatial distribution of n_{H_2} and its correlation with SF activities remain yet to be fully investigated.

By exploiting large-scale molecular line survey data at millimeter–submillimeter wavelengths accessible with the Atacama Large Millimeter/submillimeter Array (ALMA), it is now possible to simultaneously delineate the spatial variation of n_{H_2} , T_{kin} , and hydrogen column density (N_{H_2}) even in relatively distant sources. In this paper, we apply the same analysis as T18 to the NGC 253 CMZ by utilizing the unprecedentedly rich spectral data from the ALMA Comprehensive High-resolution Extragalactic Molecular Inventory (ALCHEMI) program (Barrientos et al. 2021; Harada et al. 2021, 2022; Holdship et al. 2021, 2022; Martín et al. 2021; Behrens et al. 2022; Haasler et al. 2022; Huang et al. 2023; Humire et al. 2022). The ALCHEMI survey (Martín et al. 2021) covers the 84–373 GHz frequency range at a $1''.6 (=27 \text{ pc})$ spatial and 10 km s^{-1} velocity resolution, including all tracers used in the T18 analysis. The richness of the spectral data with high enough spatial resolution ensures a reliable comparison of the P – P – V distributions of N_{H_2} , T_{kin} , and n_{H_2} to those of the GC with less ambiguity due to differences in the analysis settings. With this analysis, we discuss the fundamental differences that distinguish starburst and quiescent GMCs based on the physical condition parameters, not only on the line intensities.

The remainder of this paper is structured as follows. Section 2 outlines two statistical models for parameter inference: the hierarchical Bayesian (HB) method and the standard nonhierarchical Bayesian (NHB) method. We also use four different input data sets from ALCHEMI and T18, which are described in Section 3. The results of the analysis are presented in Section 4. A comparative study with previous works, including a comparison between NGC 253 and the GC, is made in Section 5. The final section (Section 6) summarizes the important results of this article.

2. Method

2.1. Outline of the Analysis

Different molecular lines probe different T_{kin} and n_{H_2} ranges depending on their upper-state energies and transitional critical

densities. Physical conditions can be constrained by solving the equations of molecular line excitation of multitransition data. GMC complexes generally consist of multiple components with different physical conditions, making the results of the excitation analysis dependent on the choice of input lines when the spatial resolution is insufficient to resolve the multi-component gas. The analysis is also affected by the statistical modeling employed in the parameter inference.

In this paper, we perform five different analyses for the NGC 253 CMZ using three input data sets (Low-density, High-density, and Minimal data sets) and two statistical frameworks (HB and NHB). The Low- and High-density data sets probe molecular gas components with $n_{\text{H}_2} \sim 10^3 \text{ cm}^{-3}$ and $\gtrsim 10^4 \text{ cm}^{-3}$, respectively. We can approximately decompose multiple component molecular gas in the NGC 253 CMZ by applying excitation analyses independently for these two data sets. We will perform both the HB and NHB analyses for them to examine the effect of the choice of the statistical framework on the outputs. In addition to the main analyses using the Low- and High-density data sets, we perform a supplementary analysis using the “Minimal” data set. This data set is a common subset of the above two data sets for the NGC 253 and the data set used for the GC in the T18. It consists of five molecular lines that are barely sufficient to determine T_{kin} and n_{H_2} simultaneously. By using the same data set for the NGC 253 and the GC, we can exclude bias due to the selection of tracer lines in comparing their results.

In addition to the above five analyses for the NGC 253 CMZ, we also perform a reanalysis for the GC using the Minimal data set. The GC result is used for comparison with the result of the Minimal data set for the NGC 253 CMZ.

The following subsections describe the model parameters, non-LTE excitation analysis, statistical frameworks, and data sets used in these analyses.

2.2. Model Parameters and Non-LTE Excitation Analysis

Table 1 lists the parameters required to calculate model line intensities that can be directly compared to the observed data. The parameter space includes the physical and chemical conditions, T_{kin} , n_{H_2} , dN_{H_2}/dv , fractional abundances of the molecules involved (x_{mol}), and $^{12}\text{C}/^{13}\text{C}$ isotopic abundance ratio (R_{13}). We assume R_{13} is common for all ^{13}C -bearing species except for ^{13}CO , though the $^{12}\text{C}/^{13}\text{C}$ isotopic ratio may differ among species due to chemical fractionation and selective photodissociation effects. The assumption of common R_{13} is supported by the ALCHEMI compact array data (Martín et al. 2021), which show a consistent $^{12}\text{C}/^{13}\text{C}$ isotopic ratio for the high dipole moment molecules used in the present analysis. The ^{13}CO is treated differently from other ^{13}C -bearing species. We fix $x_{\text{mol}}(^{13}\text{CO})$ at the value taken from Martín et al. (2019), as $x_{\text{mol}}(^{13}\text{CO})$ cannot be accurately constrained from our input data set as we describe later in Section 3.2.

The line intensities are calculated by solving the non-LTE rate equations, where the large velocity gradient (LVG) approximation (Goldreich & Kwan 1974) is employed to evaluate the opacity effect. The coefficients of the radiative and collisional transitions are taken from the Leiden Molecular and Atomic Database (LAMDA; Schöier et al. 2005). The collision coefficients of HCN, $p - \text{H}_2\text{CO}$, and HC_3N are not provided for temperatures high enough to cover the full T_{kin} range of the present analysis, which is 1000 K. We applied constant extrapolation for the coefficients outside the temperature range given in the tables. References for the collision rates of

Table 1
Model Parameters and Hyperparameters

Parameter	Description
\mathbf{p}_i (parameter vector at i th voxel)	
$\log_{10} dN_{\text{H}_2}/dv$	hydrogen column density per unit velocity width in units of $\text{cm}^{-2} (\text{km s}^{-1})^{-1}$
$\log_{10} T_{\text{kin}}$	gas kinetic temperature in units of K
$\log_{10} n_{\text{H}_2}$	hydrogen volume density in units of cm^{-3}
$\log_{10} x_{\text{mol}}(X)$	fractional abundance of molecule X relative to H_2
$\log_{10} R_{13}$	$^{12}\text{C}/^{13}\text{C}$ isotopic abundance ratio
$\log_{10} \phi_i$	ϕ -parameter; related to the beam-filling factor Φ by $\Phi = 1 - e^{-\phi}$
ϵ_i (nonstatistical error vector at i th voxel)	
ϵ_{ik}	nonstatistical relative error of the k th line intensity/ratio
θ (hyperparameter)	
μ	location vector of the multivariate log-student prior of \mathbf{p}_i
Σ	scale matrix of the multivariate log-student prior of \mathbf{p}_i
σ	scale parameters of the log-normal prior of ϵ_i

individual species are provided in Table 2. The escape probabilities are calculated assuming spherical geometry. We do not consider excitation through IR pumping, as the analysis of the HCN and HNC intensity ratio has shown that IR pumping is unlikely to be the dominant excitation mechanism in the ALCHEMI data (Behrens et al. 2022). We will also examine the effect of the IR pumping independently later in this paper (Section 4.8.4). The LVG-calculated intensities are converted into the observable intensities by multiplying by the beam-filling factor (Φ). We introduce the ϕ parameter, which is related to Φ as $\Phi = 1 - e^{-\phi}$, so that Φ is constrained to the range 0–1 for $\phi > 0$. We represent the above parameters at the i th spaxel by the parameter vector $\mathbf{p}_i = (p_{ij})$, where j indexes the individual parameter elements. All parameters are in the base-10 logarithm scale. We fix a few parameters to obtain reliable results from currently available observational information, of which details are given in Section 3.5.

The observed intensities are also practically dependent on nonstatistical errors, which may arise from calibration uncertainties and model deficiencies, such as the breakdown of the ideal LVG approximation. We assume the nonstatistical errors to be multiplicative and represent the relative errors by the vector $\epsilon_i = (\epsilon_{ik})$, where subscripts i, k index the spaxels and lines, respectively.

In addition to the above fundamental parameters, we also use a composite parameter representing the beam-diluted column density: $\langle N_{\text{H}_2} \rangle_{\text{beam}} \equiv \Phi \cdot N_{\text{H}_2}$, which is a direct measure of the gas mass contained within a spaxel. This paper uses simplified symbols for the primary parameters dN_{H_2}/dv , $\frac{d\langle N_{\text{H}_2} \rangle_{\text{beam}}}{dv}$, n_{H_2} , T_{kin} , R_{13} , and ϕ , represented by N , $\langle N \rangle$, n , T , R , and ϕ , respectively. They are primarily used in subscript indices of vectors and matrices; for instance, p_{iN} denotes the dN_{H_2}/dv value at i th spaxel.

2.3. Hierarchical Bayesian Analysis

The HB analysis (Kelly et al. 2012, T18) can handle problems including nonstatistical errors, whose values are difficult to infer with the standard maximum-likelihood (ML)

Table 2
Input Data Sets

Data Set	Molecule	Transitions	Frequency (GHz)	E_u/k_B (K)	$\log_{10} n_{\text{crit}}^c$ (cm^{-3})	Collisional Excitation Rate References
Low-density	CO	^d 1–0	115.2712	5.5	3.3	Yang et al. (2010)
		^d 2–1	230.5380	16.6	3.8	
		^d 3–2	345.7960	33.2	4.2	
	¹³ CO	^d 1–0	110.2014	5.3	3.3	Yang et al. (2010)
		^d 2–1	220.3987	15.9	3.8	
		^d 3–2	330.5880	31.7	4.2	
	C ¹⁸ O	1–0	109.7822	5.3	3.3	Yang et al. (2010)
		2–1	219.5604	15.8	3.8	
		3–2	329.3306	31.6	4.2	
High-density	HCN	1–0	88.6316	4.3	6.4	Dumouchel et al. (2010) ^a
		^e 3–2	265.8864	25.5	7.0	
		4–3	354.5055	42.5	7.3	
	HCO ⁺	1–0	89.1885	4.3	5.4	Flower (1999)
		^e 3–2	267.5576	25.7	6.4	
		4–3	356.7343	42.8	6.6	
	HNC	^e 3–2	271.9811	26.1	6.8	Dumouchel et al. (2010) ^a
	CS	^e 3–2	146.9690	14.1	5.8	Turner et al. (1992)
		6–5	293.9121	49.4	6.6	
	SiO	3–2	130.2686	12.5	5.8	Balanca et al. (2018)
		5–4	217.1050	31.3	6.4	
	HC ₃ N	14–13	127.3677	45.8	5.4	Faure et al. (2016) ^b
	N ₂ H ⁺	17–16	154.6573	66.8	5.6	Flower (1999)
		3–2	279.5117	26.8	6.3	
	$p - \text{H}_2\text{CO}$	4–3	372.6725	44.7	6.6	Wiesenfeld & Faure (2013) ^b
		2 _{0,2} –1 _{0,1}	145.6029	10.5	5.7	
		^e 3 _{0,3} –2 _{0,2}	218.2222	21.0	6.1	
	H ¹³ CN	3 _{2,1} –2 _{2,0}	218.7601	68.1	5.6	Green & Thaddeus (1974)
		3–2	259.0118	24.9	7.0	
		4–3	345.3398	41.4	7.2	
	H ¹³ CO ⁺	3–2	260.2553	25.0	6.3	Flower (1999)
		4–3	346.9983	41.6	6.6	
	¹³ CS	3–2	138.7393	13.3	5.7	Turner et al. (1992)
Minimal	HCN	^e 1–0				
		^e 4–3				
	$p - \text{H}_2\text{CO}$	^e 3 _{0,3} –2 _{0,2}				
		3 _{2,1} –2 _{2,0}				
	¹³ CO	^e 2–1				

Notes.^a Collision coefficients are provided for temperatures up to 500 K.^b Collision coefficients are provided for temperatures up to 300 K.^c According to the definition of n_{crit} given in Equation (4) of Shirley (2015); $n_{\text{crit}} \equiv A_{ij}/\sum_{k \neq i} \gamma_{i,k}$ for the $i \rightarrow j$ level transition, where A and γ are the Einstein A coefficient and collisional excitation rate, respectively.^d Used for the pre-analysis filtering of low-S/N spaxels. The cutoff level is 3.^e Same as (d), but the cutoff level is 2.

analysis. The inclusion of nonstatistical errors often makes the number of degrees of freedom less than zero. The HB analysis can also explicitly forbid artificial (anti)correlation among the parameters by using appropriate hyperprior functions. The following outlines the HB framework we utilized in this paper; we refer readers to T18 for details on the method.

Let $\mathcal{V} = \{v_i\}$, where the elements of vector $v_i = \{v_{ik}\}$ represent the k th line intensity at the i th spaxel. The present analysis uses raw line intensities or intensity ratios as v_{ik} . Then the hierarchical posterior probability is given by Bayes' theorem;

$$\Pr(\mathcal{P}, \mathcal{E}, \theta | \mathcal{V}) = \Pr(\mathcal{V} | \mathcal{P}, \mathcal{E}) \cdot \Pr(\mathcal{P}, \mathcal{E} | \theta) \cdot \Pr(\theta), \quad (1)$$

where $\Pr(\cdot | \cdot)$ denotes the conditional probability density function (PDF), $\mathcal{P} = \{p_i\}$, and $\mathcal{E} = \{e_i\}$. The function $\Pr(\mathcal{P}, \mathcal{E} | \theta)$ is the prior probability, which is the conditional PDF of \mathcal{P} and \mathcal{E} when the hyperparameter θ is given. The hyperparameter θ consists of the location (μ) and scale parameters (Σ) of the prior function. The scale parameter Σ is further decomposed into the scaling diagonal matrix S and correlation matrix R as $\Sigma = SRS$. The PDFs of the hyperparameters are given by the hyperprior function $\Pr(\theta)$. Here and henceforth, normalization constants of PDFs are omitted whenever possible. The function forms of $\Pr(\mathcal{V} | \mathcal{P}, \mathcal{E})$, $\Pr(\mathcal{P}, \mathcal{E} | \theta)$, and $\Pr(\theta)$ adopted in the present analysis are described in Appendix A.

The final product of the HB inference is the marginal posterior $\Pr(\mathcal{P}|\mathcal{V})$, which describes the probability distribution of the model parameters. The marginal posterior is obtained by integrating $\Pr(\mathcal{P}, \mathcal{E}, \theta|\mathcal{V})$ over the nuisance parameters, i.e., (hyper)parameters not of immediate interest;

$$\Pr(\mathcal{P}|\mathcal{V}) = \int d\mathcal{E} d\theta \cdot \Pr(\mathcal{P}, \mathcal{E}, \theta|\mathcal{V}). \quad (2)$$

2.4. Nonhierarchical Analysis

We compare the results of the HB analysis with those obtained from a more conservative analysis adopting the nonhierarchical posterior function. The posterior probability in the NHB framework is

$$\Pr(\mathcal{P}, \mathcal{E}|\mathcal{V}) = \Pr(\mathcal{V}|\mathcal{P}, \mathcal{E}) \cdot \Pr(\mathcal{P}, \mathcal{E}). \quad (3)$$

The likelihood function $\Pr(\mathcal{V}|\mathcal{P}, \mathcal{E})$ is the same as that used in the HB analysis. The prior function $\Pr(\mathcal{P}, \mathcal{E})$ is not hierarchical, i.e., not parameterized by variable hyperparameters. The function form $\Pr(\mathcal{P}, \mathcal{E})$ is chosen to be noninformative so that the analysis becomes essentially identical to the standard maximum-likelihood method. The details of the nonhierarchical posterior are given in Appendix B.

3. Data

3.1. Two-component Model

The physical condition parameters deduced from the excitation analysis for a nonuniform medium depend on the critical density (n_{crit}) and the upper-state energy (E_u) of the input lines. Figure 1 shows the posterior PDFs calculated using the median intensities from two different data sets chosen from the ALCHEMI survey. One is calculated from the line intensity ratios among the 1–0, 2–1, and 3–2 transitions of C^{18}O (labeled “ C^{18}O ” in the figure), and the other is from the median 4–3/3–2 ratios of H^{13}CN and H^{13}CO^+ , and the $3_{2,1}-2_{2,0}/3_{0,3}-2_{0,2}$ ratio of $p\text{-H}_2\text{CO}$ (labeled “High-density” in the figure). A relative uncertainty of 15% is conservatively assumed for all line intensities (Martín et al. 2021). The posterior PDFs were calculated using the nonhierarchical model, where T_{kin} and n_{H_2} are taken as the free parameters and the other parameters are fixed at typical GC values given in the figure caption. The 95% credible intervals of the two results do not overlap in the given parameter space, strongly suggesting that the two data sets trace different components of molecular gas, which likely corresponds to multiple components found in the dust and molecular line SEDs (R14; P18; Gorski et al. 2017; Mangum et al. 2019; Humire et al. 2022). A similar multicomponent gas was also reported for the GC (Nagai et al. 2007; Mills et al. 2015; Arai et al. 2016; Krieger et al. 2017, and T18).

In the present analysis, we separate the input data into two groups, i.e., the Low-density and High-density data sets, and apply a one-zone model for each. We adopt this simplified approach because a bona-fide multicomponent analysis requires too many free parameters to constrain from the available observational information. The Low-density and High-density data sets comprise CO lines and high-density tracer lines, respectively, whose details are given in the next subsections (Sections 3.2, 3.3). This method assumes that the lines in the Low- and High-density data strictly trace the low- and high-density components, respectively, such that no line

has significant emission from both components. This is a reasonable approximation for the high-density tracer lines (e.g., T18). The CO lines may have intense emission both from the low- and high-excitation gas when they are optically thick, which may cause an overestimate of n_{H_2} of the low-density component; however, the previous CO SLED analyses (R14; P18) show that the lowest-density component dominates the $J \leq 3$ transitions of CO. Although the CO SLED analyses show a third component with $T_{\text{kin}}, n_{\text{H}_2} \sim 110\text{--}160$ K, $10^{5.5\text{--}6.4} \text{ cm}^{-3}$ (R14; P18), we do not consider this highest-excitation component in this analysis, as its mass is approximately 2 orders of magnitude smaller than the second component mass. In addition, we exclude transitions with high E_u ($E_u/k_B > 70$ K) from the High-density data set to suppress the contamination from the highest-excitation component (Section 3.3).

It should also be noted that the validity of the one-zone approximation needs verification, in particular for the high-density component. For example, star-forming dense gas generally consists of multiple components with different physical characteristics probed by different molecular lines, which cannot be spatially resolved with the ALCHEMI beam size of 27 pc. The present analysis treats the breakdown of the one-zone model by introducing the error parameter ϵ in the Hierarchical analysis, which enables us to estimate averaged physical conditions over multiple physical components co-existing in a beam. This also means that the results of the HB analysis may differ from the physical conditions deduced from fewer molecular lines; we will investigate the species-to-species difference in their excitation conditions in a later section (Section 4.8.4).

In addition to the Low- and High-density data sets, we use a subset consisting of five transitions commonly included in the two data sets and the transitions used in the T18 analysis. We refer to this data set as the “Minimal data set” hereafter. In addition to the main analysis using the High-density data set, we perform the HB analyses utilizing the Minimal data set both for NGC 253 and the GC. Their results are expected to be more suitable for comparisons between the NGC 253 CMZ and the GC than the main analysis and the T18, as they are free from the potential bias arising from the selection of tracer lines.

In the following, we describe the details of the three data sets. All of the data cubes for the NGC 253 CMZ are taken from the ALCHEMI survey data (2017.1.00161.L; Martín et al. 2021). The data cubes are convolved into an angular resolution of $1''.6$ at a $0''.45$ grid spacing and velocity channel bins of 20 km s^{-1} width. We show the integrated intensity maps of the used transitions in Appendix D.

3.2. Low-density Data Set

The Low-density data set consists of the $J = 1\text{--}0$, $2\text{--}1$, and $3\text{--}2$ transitions of CO, ^{13}CO , and C^{18}O . Their optically thin critical densities and upper-state energies are $\log_{10} n_{\text{crit}}/\text{cm}^{-3} \sim 3\text{--}4$, and $E_u/k_B \sim 5\text{--}30$ K, respectively. To limit the analysis to emissions detected with sufficient signal quality, we applied a signal-to-noise ratio (S/N) cutoff of 3 to all CO and ^{13}CO measurements. Only spaxels with both CO and ^{13}CO intensities above this S/N cutoff are included in the analysis.

The present analysis approximates that the beam-filling factor Φ is common for all lines at each spaxel; however, the ^{12}CO lines are expected to have significantly large Φ because of their large optical depths of ~ 10 . The breakdown of the

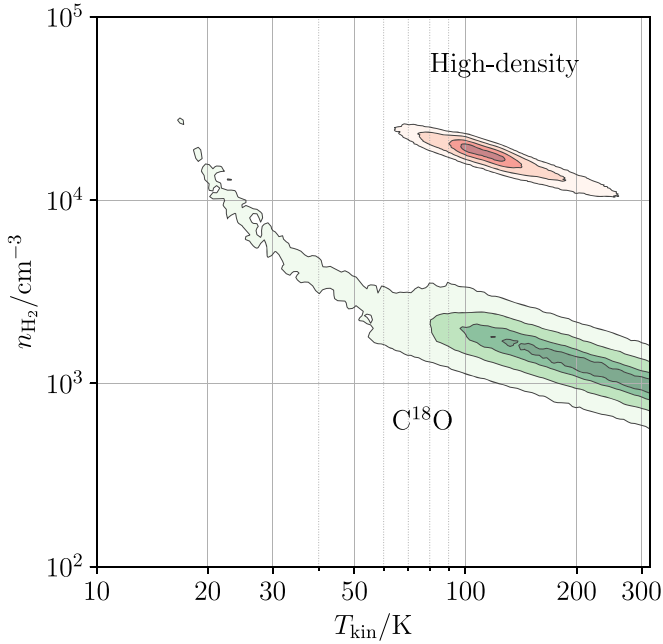


Figure 1. Posterior probabilities calculated from the intensity ratios of the C^{18}O lines (green contours; labeled “ C^{18}O ”) and those from the H^{13}CN , H^{13}CO^+ , and $p\text{-H}_2\text{CO}$ lines (red contours; labeled “High-density”). Contours indicate 20%, 50%, 80%, and 95% credible intervals. Parameters other than T_{kin} and n_{H_2} are fixed at typical values in the GC (Tanaka et al. 2018): $\phi = 0.1$, $\frac{dN_{\text{H}_2}}{dV} = 10^{22} \text{ cm}^{-2}(\text{km s}^{-1})^{-1}$, $x_{\text{mol}}(\text{CO}) = 10^{-4}$, $x_{\text{mol}}(\text{H}^{13}\text{CN}) = 10^{-8.1}$, $x_{\text{mol}}(\text{H}^{13}\text{CO}^+) = 10^{-9.5}$, and $x_{\text{mol}}(p\text{-H}_2\text{CO}) = 10^{-8.3}$. The two line groups represent two independent physical components whose n_{H_2} differ by ~ 1 dex.

approximation of common Φ may lead to a significant underestimation of the ^{12}CO beam-filling factor, and hence an overestimation of their undiluted intensities. This is problematic because the undiluted $^{12}\text{CO } J = 1\text{--}0$ intensity almost directly determines T_{kin} because of its high opacity and low n_{crit} . To avoid this problem, we use the $3\text{--}2/1\text{--}0$ and $3\text{--}2/2\text{--}1$ intensity ratios as the input data for the ^{12}CO lines instead of their absolute intensities. As a drawback, we cannot determine the isotopic abundances with sufficient accuracy because of the lack of absolute ^{12}CO intensities. Hence, we fix R_{13} at 21 according to Martín et al. (2019) in the analysis using the Low-density data set. We also assume a constant $[\text{CO}]/[\text{C}^{18}\text{O}]$ isotopic abundance of 130 (Martín et al. 2019) for consistency.

Figure 2 shows an example of the excitation analysis using the Low-density data set, which includes the marginal posterior $\text{Pr}(\mathcal{P}|\mathcal{V})$ calculated using the NHB method. The input intensities \mathcal{V} are averages over the central $10''$ radius. The posterior probability shows a highly elongated shape on the $T_{\text{kin}}\text{--}n_{\text{H}_2}$ plane, indicating the strong degeneracy of the two parameters.

3.3. High-density Data Set

The High-density data set is selected from the transitions of the molecules used in the T18 analysis (HCN, HCO^+ , HNC, CS, SiO, HC_3N , N_2H^+ , $p\text{-H}_2\text{CO}$, and their ^{13}C isotopologues) using the following criteria:

1. $n_{\text{crit}} \gtrsim 10^5 \text{ cm}^{-3}$ in the optically thin limit and the upper-state energy $E_u/k_B \lesssim 70 \text{ K}$,
2. negligible confusion from adjacent lines,

3. spatial distribution widespread over the entire CMZ (not applied to ^{13}C isotopologues),
4. no prominent self-absorption dips toward the TH2 position, and
5. more than one transition or isotopologue line that satisfies criteria 1–4 in the ALCHEMI data.

The selected lines are shown in Table 2. Criterion 1 is used to select high-density tracers while avoiding potential contamination from local high-temperature spots such as embedded hot cores. Criterion 4 is necessary to avoid confusion with self-absorption features. TH2 is an intense nonthermal continuum source (Turner & Ho 1985; Ulvestad & Antonucci 1997), toward which deep self-absorption dips are detected in low-frequency bands of the ALCHEMI data. All optically thin transitions of the molecules in the High-density data set in Band-3 do not satisfy criterion 4. As an exception to the above criteria, we include HNC 3–2 in the data set to use it as a proxy of H_2 though it does not satisfy criterion 5. Low-S/N measurements were excluded in the same manner as in the Low-density data set. The lines used in the pre-analysis filtering of the low-emission spaxels are marked in Table 2; relatively abundant species in Bands 4 and 6 were chosen for the filtering. The cutoff S/N level is set to be 2, though the cutoff level of 3 is used for the Low-density data set. We adopt a lower cutoff level so that the High-density data set has a $P\text{--}P\text{--}V$ coverage close to the Low-density data set while keeping sufficient quality.

The problem of the coupling between T_{kin} and the beam-filling factor Φ is not critical in the High-density data set, as the High-density set does not contain high- Φ and low- n_{crit} lines such as $\text{CO } J = 1\text{--}0$. With the High-density data set, T_{kin} is mainly determined by the $p\text{-H}_2\text{CO } 3_{2,1}\text{--}2_{2,0}/3_{0,3}\text{--}2_{0,2}$ intensity ratio (Mangum et al. 2019), which is unaffected by Φ when Φ is common for the two transitions. Hence, the absolute intensities are used as the input for all lines in the High-density set. As the absolute intensities of HCN, HCO^+ , CS, and their ^{13}C isotopologues are available, we do not fix the R_{13} value and treat it as a probability variable in the analysis with the High-density data set.

Figure 3 shows an example of excitation analysis using the High-density data set averaged over the central $\pm 10''$ region. The optimal T_{kin} and n_{H_2} values are relatively well determined compared with the Low-density analysis (Figure 2), owing to the inclusion of the two $p\text{-H}_2\text{CO}$ lines, whose intensity ratio only weakly depends on n_{H_2} . However, parameter degeneracy is still identified in the $N_{\text{H}_2}\text{--}n_{\text{H}_2}$ and $T_{\text{kin}}\text{--}n_{\text{H}_2}$ planes, which can cause artificial anticorrelation between $P\text{--}P\text{--}V$ distributions of these parameters.

3.4. Minimal Data Set

From the lines commonly included in the High-density data set and T18 data sets, we selected five lines ($^{13}\text{CO } 2\text{--}1$, HCN 1–0 and 4–3, and $p\text{-H}_2\text{CO } 3_{0,3}\text{--}2_{0,2}$ and $3_{2,1}\text{--}2_{2,0}$; listed in Table 2). The $p\text{-H}_2\text{CO } 3_{2,1}\text{--}2_{2,0}/3_{0,3}\text{--}2_{0,2}$ intensity ratio is a good T_{kin} probe as mentioned above, which effectively resolves the $T_{\text{kin}}\text{--}n_{\text{H}_2}$ degeneracy in the HCN 4–3/1–0 ratio. Thus, this data set is expected to allow physical condition measurements of the high-density component with low degeneracy. Note that this is not the unique selection of the smallest data set required for a nondegenerate solution in general; however, we refer to this data set as “Minimal” as it

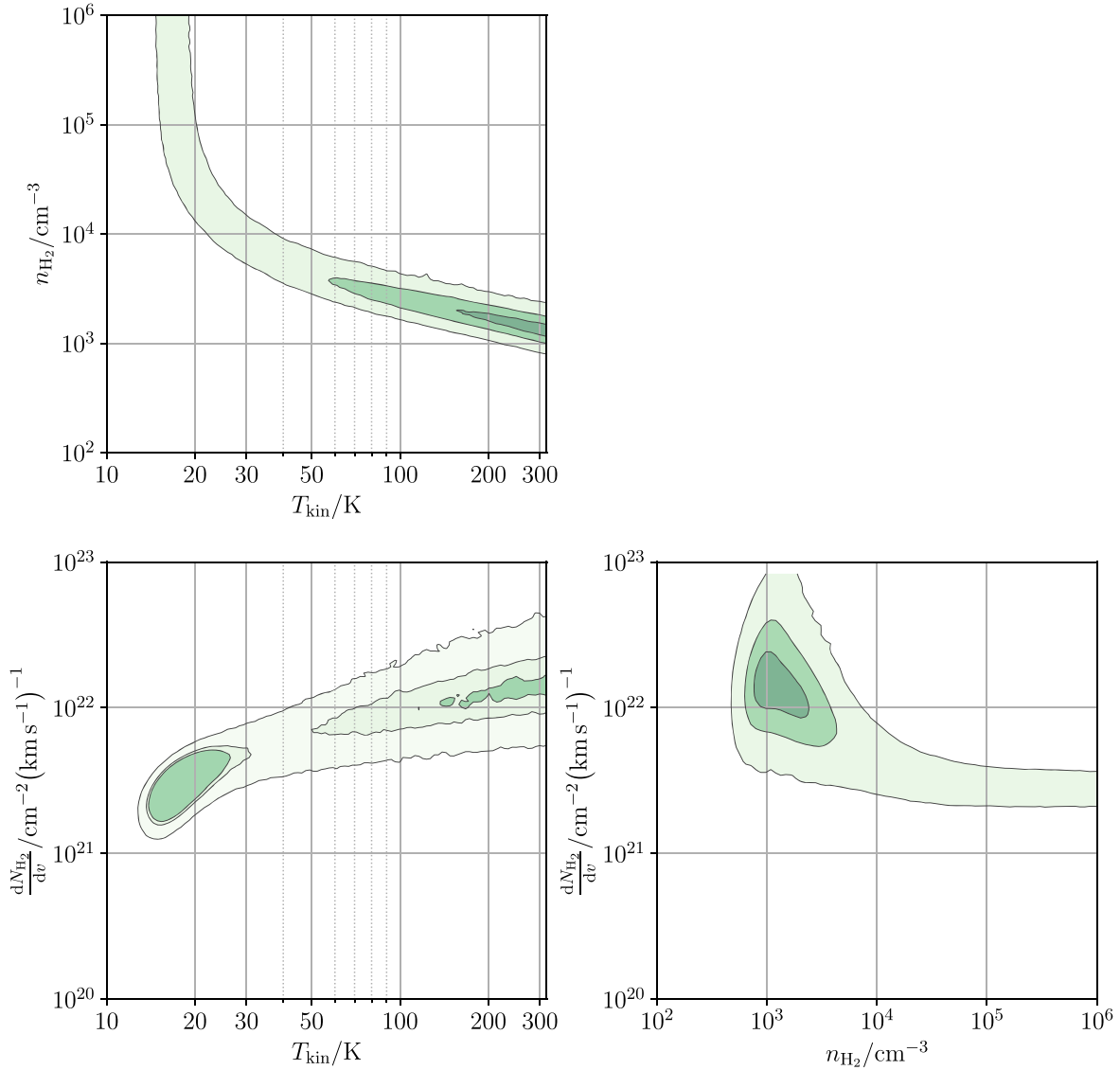


Figure 2. Example of the excitation analysis using the Low-density data set averaged over the central $10''$ radius. The posterior probability calculated using the NHB analysis is shown in the dN_{H_2}/dv – T_{kin} – n_{H_2} parameter space, with contours drawn at 20%, 50%, and 90% credible intervals. The molecular abundances are fixed at $x_{\text{mol}}(^{13}\text{CO}, \text{C}^{18}\text{O}) = 10^{-5.32}, 10^{-6.11}$ assuming $x_{\text{mol}}(\text{CO}) = 10^{-4}$. A relative uncertainty of 15% is assumed for all line intensities according to Martín et al. (2021).

comprises the minimum necessary transitions that can be constructed from the intersection of the High-density data set and the T18 data set.

All transitions qualify the same criteria for the High-density data set except for ^{13}CO 2–1, which does not satisfy criteria 1 and 2. We include ^{13}CO 2–1 to use it as an approximate N_{H_2} tracer independent of the HCN and H_2CO intensities, similar to the T18 analysis. Although the ^{13}CO 2–1 line may not be an ideal tracer of the high-density component due to its low $n_{\text{crit}} \sim 10^{3.8} \text{ cm}^{-3}$, it is still useful for an approximate measure of N_{H_2} on the assumption that the high-density and low-density components have similar large-scale mass distribution patterns in the P – P – V space. Indeed, T18 found good correlations between intensities of representative high-density tracer lines (HNC 1–0 and HCO^+ 1–0) and ^{13}CO 2–1-based column density for the GC. We will verify the correlation between N_{H_2} of the low- and high-density components for the NGC 253 CMZ, based on the analyses using the Low- and High-density data sets in a later section (Section 4.5). More accurate N_{H_2}

tracers, such as higher- J ^{13}CO lines or ^{13}C isotopologues of high-density tracer lines, are not available for the GC or do not satisfy criterion 5.

The Minimal data set for the GC is prepared using the data compiled from Jones et al. (2012), Ginsburg et al. (2016), and T18. All GC data are re-gridded to the same angular and velocity griddings and resolutions as those in T18, i.e., $30'' \times 30'' \times 10 \text{ km s}^{-1}$ and $60'' \times 60'' \times 10 \text{ km s}^{-1}$, respectively. The angular resolution of $60''$ corresponds to 2.4 pc at the distance to the GC (8.18 kpc; Gravity Collaboration et al. 2019). We refer readers to T18 for a detailed data description.

Figure 4 shows an example of the joint posterior probability of N_{H_2} , T_{kin} , and n_{H_2} calculated using the averaged intensities of the Minimal data sets over the central $10''$ region. The posterior probability shows two local maxima. The lower- N_{H_2} solution at $dN_{\text{H}_2}/dv \sim 10^{20} \text{ cm}^{-2} (\text{km s}^{-1})^{-1}$ is not consistent with the High-density result (Figure 3), and hence the higher- N_{H_2} peak at $dN_{\text{H}_2}/dv \sim 10^{21.5} \text{ cm}^{-2} (\text{km s}^{-1})^{-1}$ is likely to represent the true physical conditions of the high-density component. The

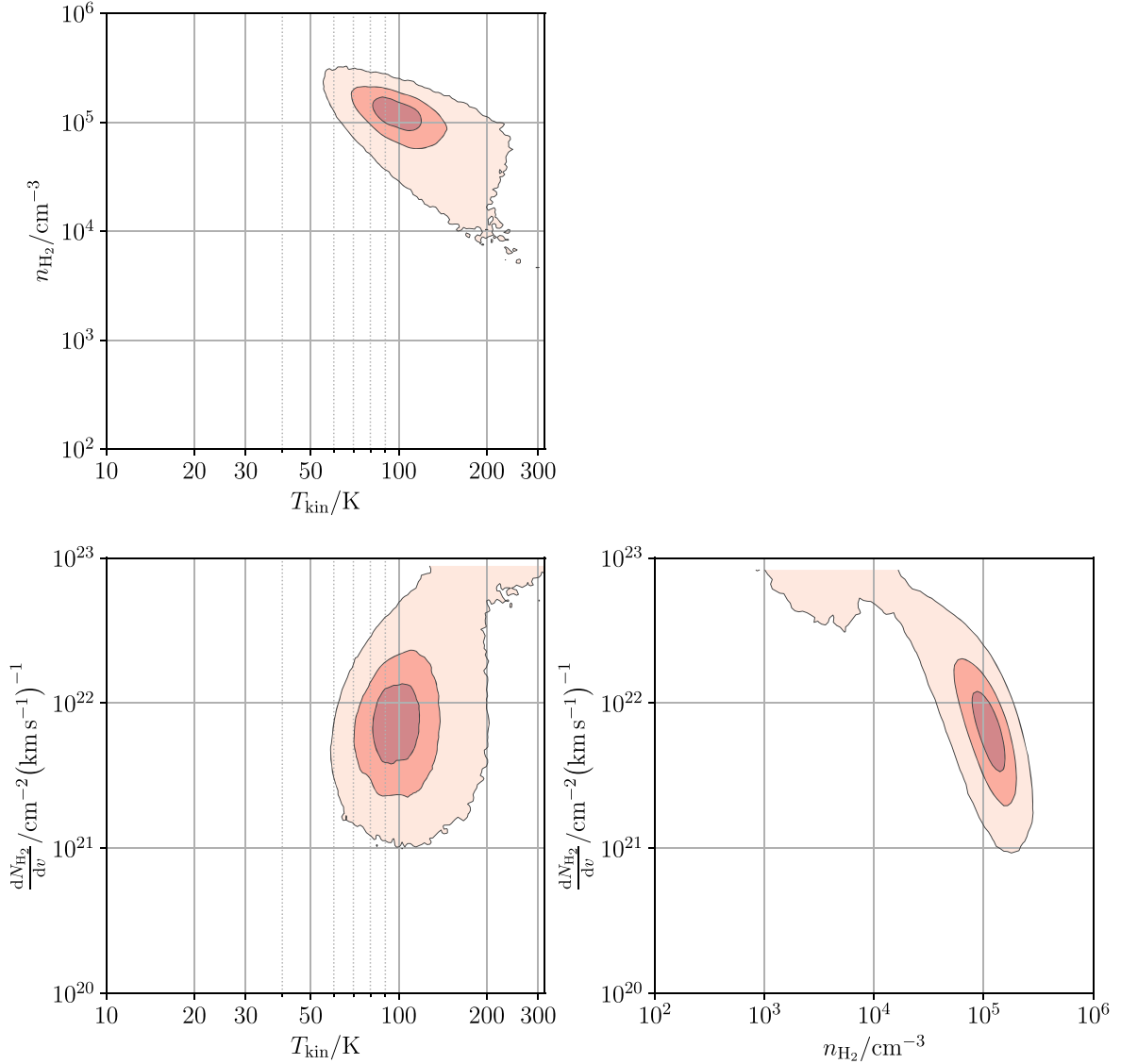


Figure 3. Same as Figure 2, but for the NHB analysis with the High-density data set.

higher- N_{H_2} solution shows $T_{\text{kin}} \sim 100$ K, which is approximately consistent with the High-density analysis, as T_{kin} values are predominantly determined by the $p - \text{H}_2\text{CO}$ lines for both analyses. The n_{H_2} value is relatively poorly determined, and its 50% interval spans over more than an order of magnitude around the higher- N_{H_2} solution. Hence, analysis using the Minimal data set is less accurate than that using the High-density data set, reflecting the limited number of input transitions in the former. We also note that the HCN and $p - \text{H}_2\text{CO}$ lines may be biased to relatively high-temperature gas likely associated with turbulence (T18). In this sense, the High-density data set better represents the entire high-density component that includes both turbulent and quiescent regions than the Minimal data set.

3.5. Fixed Parameters

We have to fix the abundance of one molecular species in each data set to use it as a proxy for H_2 . We assume $x_{\text{mol}}(\text{CO}) = 10^{-4}$ in the analysis with Low-density and Minimal data sets, i.e., the same assumption as in T18. We

use HNC to measure N_{H_2} for the High-density data set as HNC is considered as a “neutral” species in the GC, in the sense that HNC 1–0 is the best correlated with the dust 500 μm flux in the Band-3 lines of the high dipole moment molecules analyzed by T18 (HNC, HCN, HCO^+ , CS, SiO, HC_3N , N_2H^+ , and $p - \text{H}_2\text{CO}$). T18 has also shown that HNC is one of the species with the least spatial variation in the fractional abundance (~ 0.1 dex in rms at a 27 pc resolution) in the GC. For the NGC 253 CMZ, Behrens et al. (2022) reported a factor of ~ 2 variation in the $[\text{HCN}]/[\text{HNC}]$ abundance ratio among the major GMCs. This $[\text{HCN}]/[\text{HNC}]$ variation is similar to that in the GC (T18), which would allow us to assume that the $x_{\text{mol}}(\text{HNC})$ variation in the NGC 253 CMZ is also similar to that in the GC. We assume $x_{\text{mol}}(\text{HNC}) = 4 \times 10^{-8}$ for the NGC 253 CMZ, which is estimated by multiplying the typical $x_{\text{mol}}(\text{HNC})$ in the GC, 2×10^{-8} (T18), by the NGC 253-to-GC ratio of the HNC 1–0/ ^{13}CO 2–1 intensity ratio, 2. We will verify this assumption by comparing the derived dense-gas mass to the previous CO SLED results (Section 5.2.1). Breakdown of the constant $x_{\text{mol}}(\text{HNC})$ approximation is a potential source of systematic errors in N_{H_2} , but it does not

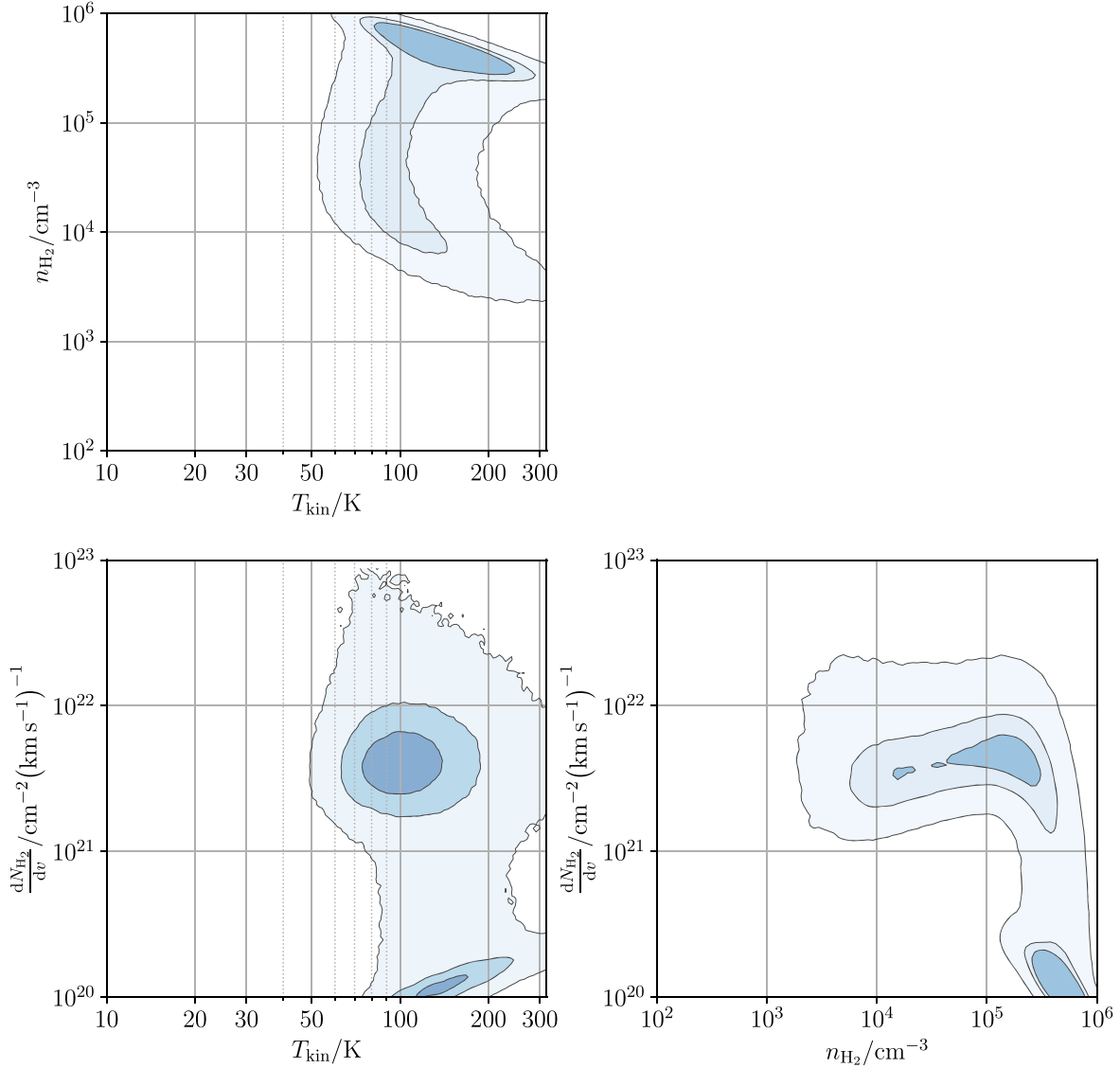


Figure 4. Same as Figure 2, but for the NHB analysis with the Minimal data set.

critically affect the excitation analysis as the line intensities depend on the column densities of individual molecules, not on N_{H_2} .

We fix $R_{13} = 21$ in the analysis using the Low-density data set as already mentioned in Section 3.2. The same R_{13} value is applied to the Minimal data sets both for NGC 253 and the GC, which is used to translate $N(^{13}\text{CO})$ into N_{H_2} . Although the GC has a slightly higher R_{13} value of ~ 25 (Langer & Penzias 1990, 1993; T18), we ignore the difference to make the comparison between the two galaxies easier. We have to consider this simplification and the uncertainty in $x_{\text{mol}}(\text{CO})$ when we compare N_{H_2} of NGC 253 and the GC. We also fix the $[\text{C}^{18}\text{O}]/[\text{C}^{12}\text{CO}]$ abundance in NGC 253 at the value in Martín et al. (2019), i.e., $x_{\text{mol}}(\text{C}^{18}\text{O}) = 7.8 \times 10^{-7}$, for the purpose of consistency.

4. Results

4.1. Analysis Runs

We ran six analyses using the two statistical modelings (HB and NHB) and three data sets (High-density, Low-density, and Minimal; abbreviated as High, Low, and Min, respectively)

described in the previous sections. Table 3 tabulates the combination of the statistical modelings and data sets used in individual analysis runs. We conducted both HB and NHB analyses for each of the High- and Low-density sets to verify the effect of the prior probability. Only the HB analysis was applied to the Minimal sets of the ALCHEMI and MW data; the NHB analyses were not necessary for them, as their validity can be verified through comparison with the results with the High-density data set and the T18 results. We refer to individual analysis runs by the combination of the abbreviations of the names of the data set and the statistical framework used, e.g., “High-HB” for the HB analysis with the High-density data set, and so on. Table 3 also summarizes the fixed parameters in individual analysis runs described in Section 3.5.

For each analysis run, the marginal posterior function $\text{Pr}(\mathcal{P}|\mathcal{V})$ (Equations (2) and (B2)) was numerically calculated by employing the Markov Chain Monte Carlo (MCMC) method, where the hybrid Monte Carlo method (Duane et al. 1987) was employed; details of the sampling method are provided in T18. Examples of the MCMC results including

Table 3
Analysis Runs

Run Name	Data Set	Statistical Modeling	Fixed Abundance	R_{13}
High-HB	High-Density	HB	$x_{\text{mol}}(\text{HNC}) = 4 \times 10^{-8}$	Variable
High-NHB	High-Density	NHB	$x_{\text{mol}}(\text{HNC}) = 4 \times 10^{-8}$	Variable
Low-HB	Low-Density	HB	$x_{\text{mol}}(\text{CO}) = 10^{-4}$, $x_{\text{mol}}(\text{C}^{18}\text{O}) = 7.8 \times 10^{-7}$	21
Low-NHB	Low-Density	NHB	$x_{\text{mol}}(\text{CO}) = 10^{-4}$, $x_{\text{mol}}(\text{C}^{18}\text{O}) = 7.8 \times 10^{-7}$	21
Min-HB	Minimal	HB	$x_{\text{mol}}(\text{CO}) = 10^{-4}$	21
GC-HB	Minimal (MW)	HB	$x_{\text{mol}}(\text{CO}) = 10^{-4}$	21

trace plots and corner plots of the posterior function are provided in Appendix E.

The marginal posteriors of the individual \mathcal{P} elements, i.e., all parameters at all spaxels, are calculated based on the MCMC results after convergence. The marginal posteriors are reduced into P - P - V cubes of individual parameters by adopting the medians and 50% credible intervals as the representative value and uncertainty, respectively. Poorly determined values with 50% credible intervals above 0.3, which corresponds to the relative uncertainty of $>41\%$ in the linear scale, are excluded from the final cubes.

Table 4 shows the flux coverage of the Low-HB and High-HB analyses, which we define as the fraction of molecular line fluxes included in the region where the HB analyses were successful (i.e., the credible interval of $\langle N_{\text{H}_2} \rangle_{\text{beam}}$ is less than 0.3 dex) to the total fluxes. The total fluxes were measured over the spaxels where the CO 1–0 intensity is above 5σ . We find that $\gtrsim 90\%$ of the fluxes of the primary gas mass tracers (the ^{13}CO and HNC transitions) and 77%–89% of the fluxes of the CO transitions and the $J \geq 3-2$ transitions of major high-density tracers (HCN, HCO^+ , and HNC) were covered by the present analysis, with the lower excitation transitions having the lower flux coverages. Table 4 also shows that $\sim 35\%$ of the total flux of HCN 1–0 and HCO^+ 1–0, which are frequently used dense-gas mass tracers, are missed by the High-HB analysis.

We also evaluated the optical depths of the transitions used in the analysis from the parameters obtained from the Low-HB and High-HB analyses. Detailed descriptions of the calculation and the results are provided in Appendix F.

4.2. Hierarchical versus Nonhierarchical Analysis

In addition to the P - P - V distributions of the individual parameters, we also calculated their medians ($\tilde{\mu}_i$) and the covariance matrix (\tilde{R}_{ij}) at every MCMC step, whereby constructing their marginal posteriors. Similarly to \mathcal{P} , the median and 50% credible intervals of the marginal posteriors are adopted as the representative values and uncertainties of these statistical properties. Table 5 shows $\tilde{\mu}_i$ of dN_{H_2}/dv , $d\langle N_{\text{H}_2} \rangle_{\text{beam}}/dv$, n_{H_2} , T_{kin} , ϕ , and \tilde{R}_{ij} for important parameter pairs. Note that they are similar to, but not equal to the hyperparameters μ and R , which are the location and the correlation coefficient parts of the scale matrix Σ of the log-Student prior function (see Appendix A for their definitions), as the actual parameter distribution is not determined only by the truncated log-student prior distribution, but by the whole posterior function.

Table 5 shows that the NHB results (High-NHB and Low-NHB) show large negative correlation coefficients between several parameters: \tilde{R}_{N_n} and \tilde{R}_{T_n} in the High-NHB result, and

Table 4
Flux Coverage

Analysis	Molecule	Transition	Flux Coverage
Low-HB	CO	1–0	0.85
		2–1	0.84
		3–2	0.87
	^{13}CO	1–0	0.92
		2–1	0.94
		3–2	0.97
High-HB	HCN	1–0	0.65
		3–2	0.83
		4–3	0.89
	HCO^+	1–0	0.64
		3–2	0.83
		4–3	0.89
	HNC	3–2	0.89
		CS	0.77
	CS	3–2	0.77
		6–5	0.88

\tilde{R}_{N_ϕ} and \tilde{R}_{T_n} in the Low-NHB, reflecting their degeneracy in the excitation equations. These correlation coefficients are positive or only slightly negative in the High-HB and Low-HB analyses compared with their respective NHB counterparts, indicating that the HB analyses suppressed the anticorrelation from the parameter degeneracy.

Another significant difference is identified in $\tilde{\mu}_i$ for dN_{H_2}/dv , n_{H_2} , and ϕ of the High-HB and High-NHB results; in particular, $\tilde{\mu}_N$ and $\tilde{\mu}_n$ are 0.83 dex higher and 0.55 dex lower in High-HB than in High-NHB, respectively. This inconsistency likely originates from the N_{H_2} - n_{H_2} degeneracy in the excitation equations with the High-density set, which is exemplified in Figure 3. A similar but smaller difference in dN_{H_2}/dv and n_{H_2} is also present between the Low-HB and Low-NHB results. However, the combination of the low dN_{H_2}/dv and high n_{H_2} in the High-NHB result yields too small a spatial scale of $N_{\text{H}_2}/n_{\text{H}_2} = 3.8 \times 10^{-3} \left(\frac{\Delta v}{\text{km s}^{-1}} \right) \text{pc}$, where Δv is the typical velocity width. If we assume a typical cloud radius (r) of 0.1–10 pc, this $N_{\text{H}_2}/n_{\text{H}_2}$ yields a typical velocity dispersion (σ_v) of 26–2600 km s^{-1} , which is obviously too large compared with the r - σ_v relation for the NGC 253 CMZ (Krieger et al. 2020). The same estimate using the High-HB result yields $N_{\text{H}_2}/n_{\text{H}_2} = 9.1 \times 10^{-2} \left(\frac{\Delta v}{\text{km s}^{-1}} \right) \text{pc}$. This size scale gives σ_v of 1–100 km s^{-1} for r of 0.1–10 pc, which better fits the r - σ_v relation.

The above comparison indicates that the HB analysis was able to provide more reasonable P - P - V distributions of the physical conditions than the standard NHB analysis. Therefore, we adopt the Low-HB and High-HB results as the final results for the low- and high-excitation components in the rest of this article. However, the validity of the hierarchical framework needs verification, as the hyperprior function enforcing

Table 5
Analysis Results: Statistical Properties

i or $i j$ Unit	$\tilde{\mu}_i^a$						\tilde{R}_{ij}		
	N ($\text{cm}^{-2}(\text{km s}^{-1})^{-1}$)	$\langle N \rangle$ ($\text{cm}^{-2}(\text{km s}^{-1})^{-1}$)	n (cm^{-3})	T (K)	R	ϕ	Nn	$N\phi$	Tn
Low-NHB	21.28	20.23	3.16	1.86	1.32	−0.92	0.11	−0.73	−0.68
Low-HB	21.37	20.19	2.95	1.86	1.32	−1.18	0.84	−0.02	0.48
High-NHB	20.69	19.91	4.62	2.20	1.72	−0.69	−0.72	−0.07	−0.42
High-HB	21.52	20.56	4.07	1.99	1.78	−0.95	0.13	−0.15	0.76
Min-HB	21.10	20.18	3.86	1.96	1.32	−0.91	0.46	−0.01	0.68
GC-HB	21.25	20.68	3.99	1.92	1.32	−0.50	0.56	−0.03	0.12

Notes. Median values $\tilde{\mu}_i$ and correlation coefficients \tilde{R}_{ij} of the parameters. N , $\langle N \rangle$, n , T , and R denote dN_{H_2}/dv , $\frac{d\langle N_{\text{H}_2} \rangle_{\text{beam}}}{dv}$, n_{H_2} , T_{kin} , and R_{13} , respectively.

^a In base-10 logarithm scale.

nonnegative correlations between N_{H_2} , T_{kin} , n_{H_2} , and ϕ possibly creates artificial parameter distributions in the HB results. The Low-HB results need particularly careful verification, as the Low-HB analysis relies on the prior and hyperprior probabilities to resolve the severe parameter degeneracy shown in Figure 2. The effect of the logistic hyperprior is discussed in section Section 4.8.1.

4.3. Distributions of N_{H_2} , n_{H_2} , and T_{kin}

Figures 5–7 show the P – P – V distributions of the Low-HB, High-HB, and Min-HB results, respectively. The results of the nonhierarchical analyses for the NGC 253 CMZ (Low-NHB and High-NHB) and the HB analysis for the GC (GC-HB) are presented in Appendix G. The cubes of $\langle N_{\text{H}_2} \rangle_{\text{beam}}$, n_{H_2} , and T_{kin} are projected onto the P – P and P – V 2D images. The P – P image of $\langle N_{\text{H}_2} \rangle_{\text{beam}}$ shows a velocity integration of $\frac{d\langle N_{\text{H}_2} \rangle_{\text{beam}}}{dv}$, and the other P – P and P – V images show the $\langle N_{\text{H}_2} \rangle_{\text{beam}}$ -weighted averages of the nonblank spaxels along the respective projection axes.²³ The position axis of P – V images is taken in the major axis direction indicated in the figure, whose position angle is 55° (Leroy et al. 2015). All P – P and P – V images of the Low-HB and High-HB results show smooth continuous distribution though the analysis is on a per-spaxel basis. The Min-HB images are less smooth than the Low-HB and High-HB images, with a nonnegligible number of discontinuous pixels near emission peaks; this discontinuity is created by the blank spaxels whose 50% credible interval exceeds 0.3 due to insufficient decoupling of the model parameters.

The $\langle N_{\text{H}_2} \rangle_{\text{beam}}$ distributions basically follow the intensity distributions of the N_{H_2} tracers (^{13}CO , C^{18}O , and HNC lines). The high- $\langle N_{\text{H}_2} \rangle_{\text{beam}}$ region is concentrated in the central $\pm 10''$ region along the major axis of the CMZ, which harbors stellar clusters and star-forming dense clumps (Sakamoto et al. 2011; Leroy et al. 2018; Mills et al. 2021; referred to as the “central starburst region” hereafter). The highest $\langle N_{\text{H}_2} \rangle_{\text{beam}}$ is found toward the position of GMC6 identified by Leroy et al. (2015; denoted by an open triangle in Figures 5 and 6) in the Low-HB and High-HB results, whereas no particular $\langle N_{\text{H}_2} \rangle_{\text{beam}}$ peak is present toward the TH2 position (denoted by a cross in Figures 5–7) at the resolution of the ALCHEMI data in all

results. The central starburst region has also higher T_{kin} and n_{H_2} than the outer region. The T_{kin} enhancement in the central starburst region is approximately consistent with the spatial distribution of the CRIR measured by Behrens et al. (2022), which could support the picture that the cosmic-ray heating dominates the molecular gas heating in the NGC 253 CMZ (Behrens et al. 2022).

We may consider the possibility that the co-enhancement of n_{H_2} and T_{kin} in the high- N_{H_2} region is artificially induced by the logistic hyperprior function for R , which explicitly forbids anticorrelation between these parameters. In particular, the Low-HB result shows a remarkably tight N_{H_2} – n_{H_2} correlation coefficient of 0.84, which is close to the maximum allowed by the hyperprior function. This high correlation coefficient possibly indicates an insufficient decoupling of dN_{H_2}/dv and n_{H_2} in the excitation analysis, as the hierarchical hyperprior gives higher values for solutions with higher N_{H_2} – n_{H_2} correlation when the two parameters degenerate in the excitation equations. However, the overall n_{H_2} distribution in the Low-HB results is similar to that in the High-HB results as we will see in detail in the following subsections (Sections 4.4, 4.5). As the High-density data set does not suffer the parameter degeneracy as we have seen in Section 3.3, this similarity between the Low-HB and High-HB results suggests that the artificial effect on the n_{H_2} and T_{kin} result is limited, though the correlation coefficient between N_{H_2} and n_{H_2} is possibly overestimated for the Low-HB results. In a later subsection (Section 4.8.1), we will also show that the effect of the hierarchical prior function on the analysis results is not critical at least for the High-HB results based on analysis of the PDF of the R matrix.

4.4. High-temperature Features

Both in the Low- (Figure 5) and High-density (Figure 6) results, high- T_{kin} regions are predominantly found in the high- $\langle N_{\text{H}_2} \rangle_{\text{beam}}$ spaxels toward the central starburst region. This overall T_{kin} distribution is reasonably explained as due to cosmic-ray heating as discussed in Section 4.3. Meanwhile, we have detected several high- T_{kin} features outside the central high- N_{H_2} region either in space or velocity, which are not associated with known heating sources. In the following, we briefly describe these high- T_{kin} features commonly found in the Low-HB, High-HB, and Min-HB results, which are labeled as A1–A4, B (red and blue), and GMC1a in Figures 5–7. The P – P – V positions of A1–A4 and GMC1a are shown in both the

²³ $\langle N_{\text{H}_2} \rangle_{\text{beam}}$ -weighted average of parameter X means $\frac{\sum \Phi_i N_i X_i}{\sum \Phi_i N_i}$, where Φ_i , N_i , and X_i stand for the i th spaxel values for Φ , $\frac{d\langle N_{\text{H}_2} \rangle_{\text{beam}}}{dv}$, and X , respectively, along the projection axis.

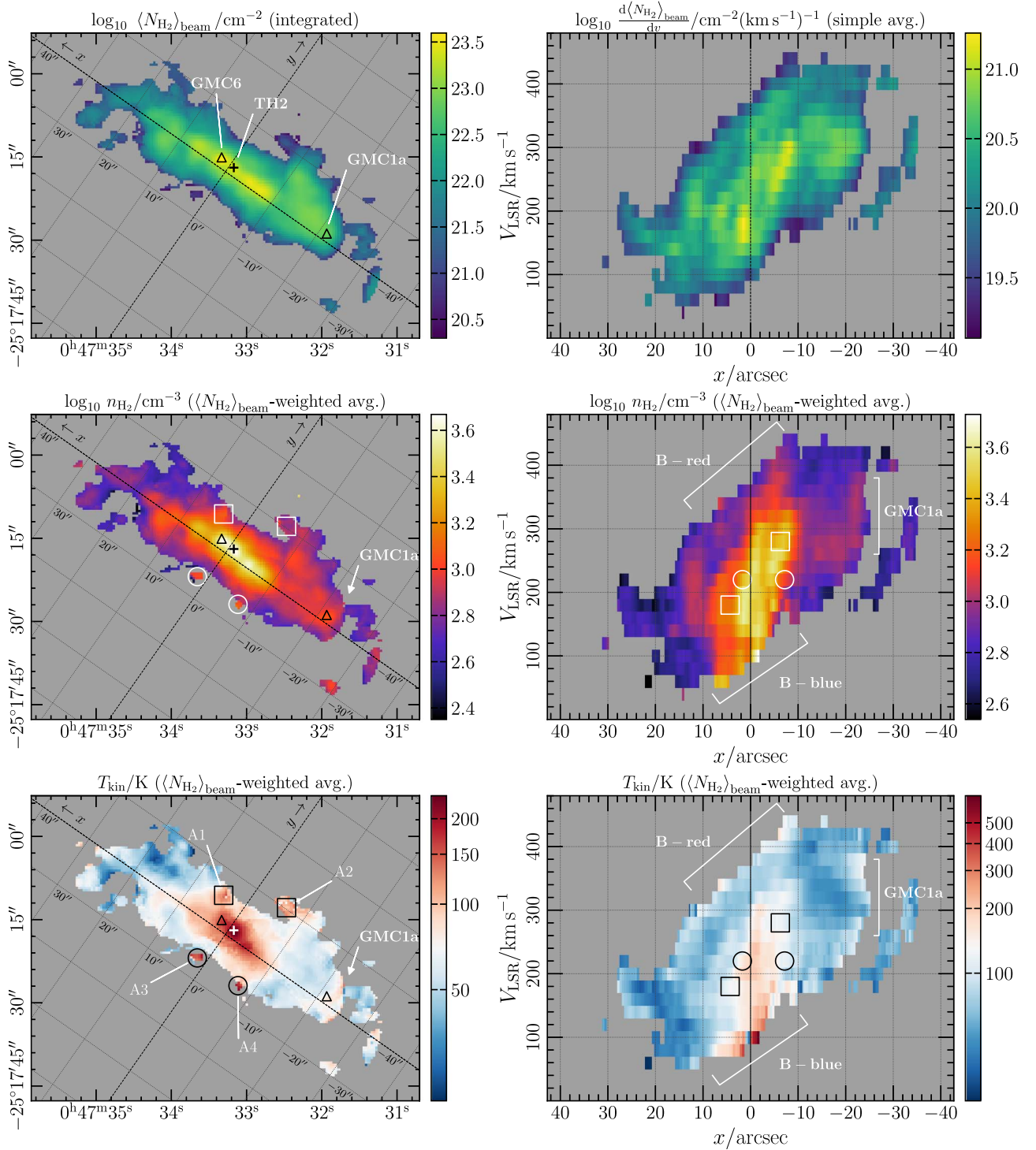


Figure 5. Position–position (left column) and position–velocity (right column) images of $\langle N_{\text{H}_2} \rangle_{\text{beam}}$, n_{H_2} , and T_{kin} of the Low-HB run (from top to bottom). The relative coordinate from the phase center of the ALCHEMI observation $(\alpha_{\text{ICRS}}, \delta_{\text{ICRS}}) = (0^{\text{h}}47^{\text{m}}33^{\text{s}}.26, -25^{\circ}17'17''.7)$ (Martín et al. 2021) along the major and minor axes is overlaid on the P – P maps with a $10''$ grid spacing. The position angle of the major axis is 55° . The P – P and P – V images of $\langle N_{\text{H}_2} \rangle_{\text{beam}}$ show the velocity integration and latitude average of $\frac{d\langle N_{\text{H}_2} \rangle}{dv}$ over nonblank P – V spaxels, respectively. The other P – P and P – V images show N_{H_2} -weighted averages along the respective projection axes. The positions of TH2 and two GMCs (GMC1a and GMC6; their positions are taken from Huang et al. 2023 and Leroy et al. 2015, respectively) are denoted by cross and open triangle marks, respectively, in the P – P images. The labels A1 through A4 show the P – P – V positions of the high- T_{kin} features described in Section 4.4. The off-plane high- T_{kin} spots are denoted by open and closed rectangles for the northern (A1 and A2) and southern (A3 and A4) spots, respectively, both in the P – P and P – V images.

P – P and P – V images, whereas B-red and -blue are shown only in the P – V images.

The P – P image of T_{kin} in Figure 5 shows four high- T_{kin} spots that are approximately $\pm 5''$ – $10''$ from the major axis of the

CMZ, which are labeled A1–4. Spot A1 also appears in the High-HB and Min-HB maps (Figures 6–7), while the other three spots are outside the spatial coverage of the High-density and Minimal data sets. Their projected locations, apparently at

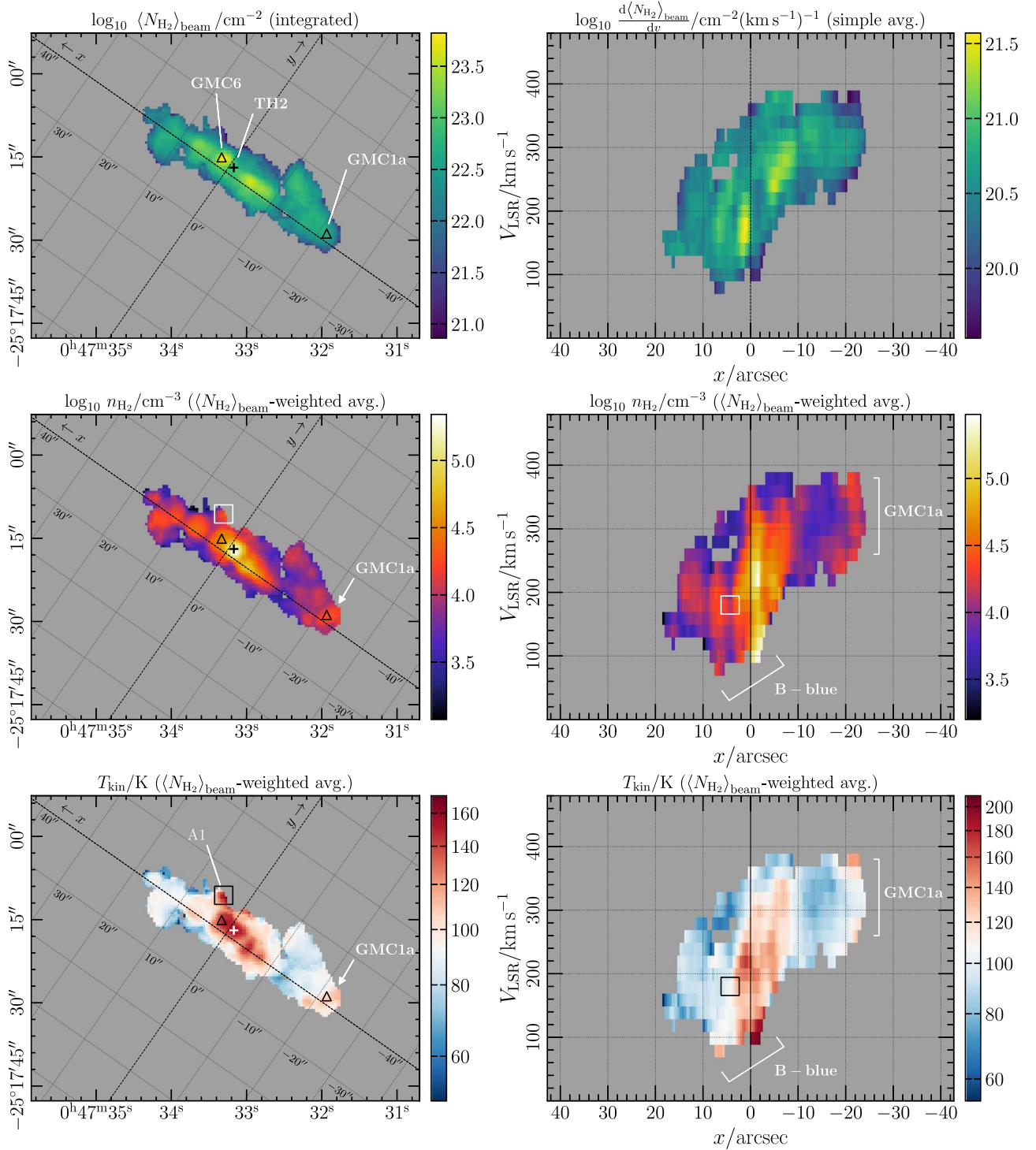


Figure 6. Same as Figure 5, but for the High-HB result.

high latitudes from the CMZ plane, may indicate that they are shocked gas at the interface between the molecular gas and the large-scale outflow (Bolatto et al. 2013). Indeed, A2 and A4 coincide with the SW and NW streamers, respectively, which consist of the western edge of the molecular outflow.

Another prominent high- T_{kin} feature is found in the lower-most LSR velocities (~ 100 – 200 km s^{-1}) in the central starburst region in the P - V diagram of the Low-HB and High-HB results, which is labeled B-blue in the figure. Its red-shifted counterpart, B-red, is also found in the Low-HB P - V diagram

of T_{kin} in 300 – 450 km s^{-1} velocities. Their spatial distributions are consistent with that of the main velocity component of the central starburst region in 200 – 300 km s^{-1} velocities, suggesting that this high-velocity warm gas is associated with the shocked GMCs detected in the SiO and HNC analyses (Huang et al. 2023).

Finally, a high- T_{kin} spot is detected toward GMC1a (Huang et al. 2023), which is near the southwestern end of the CMZ. This feature is clearly visible in the P - P and P - V images of T_{kin} of the High-HB and Min-HB results, where a pair of high-

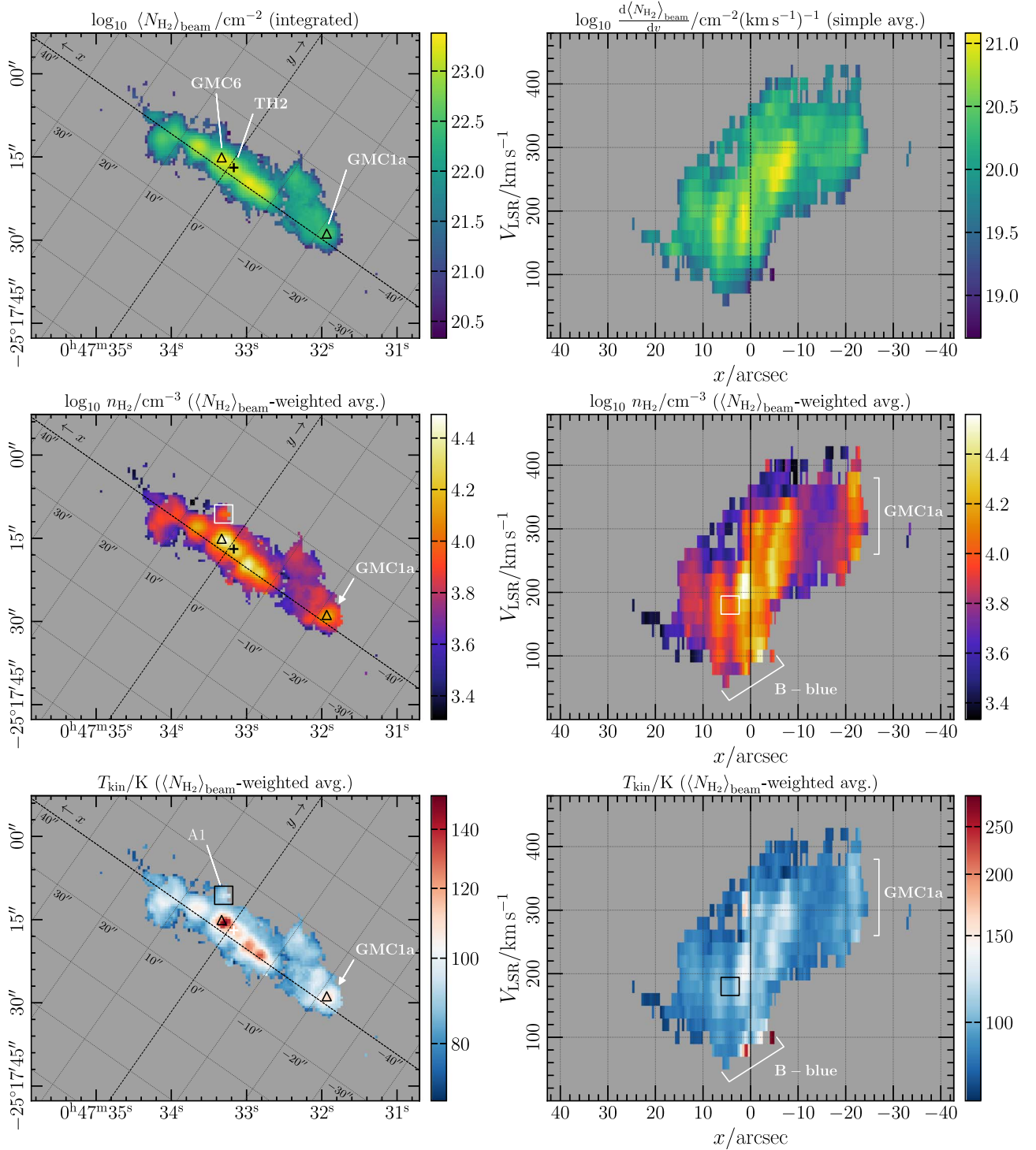


Figure 7. Same as Figure 5, but for the Min-HB result.

velocity gas with $T_{\text{kin}} \sim 100\text{--}150$ K is detected at the low- and high-velocity ends. The GMC1a was detected as the high- T_{kin} spot A7 in the NH_3 inversion line study by Gorski et al. (2017). The H_2 and HNCO column densities from the High-HB result and Huang et al. (2023), respectively, show that GMC1a has a remarkably high $[\text{HNCO}]/[\text{H}_2]$ ratio of $10^{-7.3}$, which is by more than an order of magnitude enhancement from the values in the GMCs in the central starburst region. Gorski et al. (2017) showed that the GMC1a/A7 is adjacent to an expanding shell-like structure of dense gas accompanied by class-I methanol masers. Hence, the GMC1a could be mechanically heated by a

supernova remnant shock or shocks induced by cloud–cloud collisions associated with the expanding shell. The dynamical timescale of the expanding shell estimated from the radius (30 pc) and the expanding velocity ($\sim 60 \text{ km s}^{-1}$), 0.5×10^5 yr, is approximately consistent with the shock timescale estimated by Huang et al. (2023).

4.5. Low-HB versus High-HB Analyses

Figure 8 compares the $\langle N_{\text{H}_2} \rangle_{\text{beam}}$, T_{kin} , and n_{H_2} of the Low-HB and High-HB results in scatter plots. All parameters show

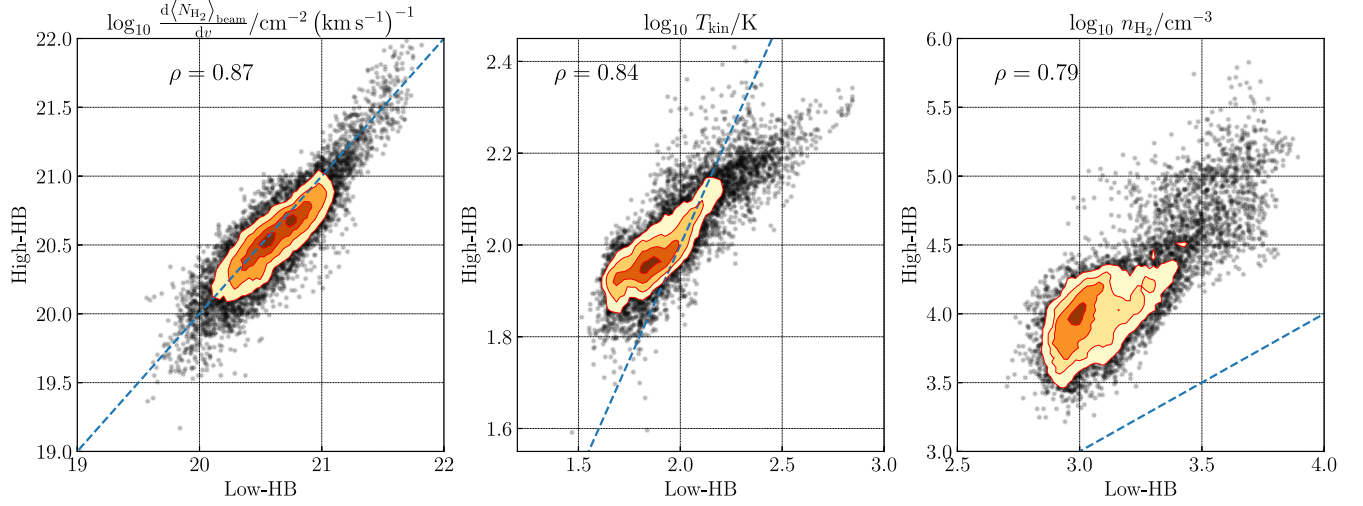


Figure 8. Spaxel-by-spaxel scatter plots of the parameters ($\langle N_{\text{H}_2} \rangle_{\text{beam}}$, T_{kin} , and n_{H_2}) from the High-HB results vs. those from the Low-HB results. The colored contours indicate 2D histograms at relative frequencies of 5%, 20%, 50%, and 70%. The correlation coefficient (ρ) is given in each panel. The dashed blue lines are for the same parameter values from the Low-HB and High-HB analyses.

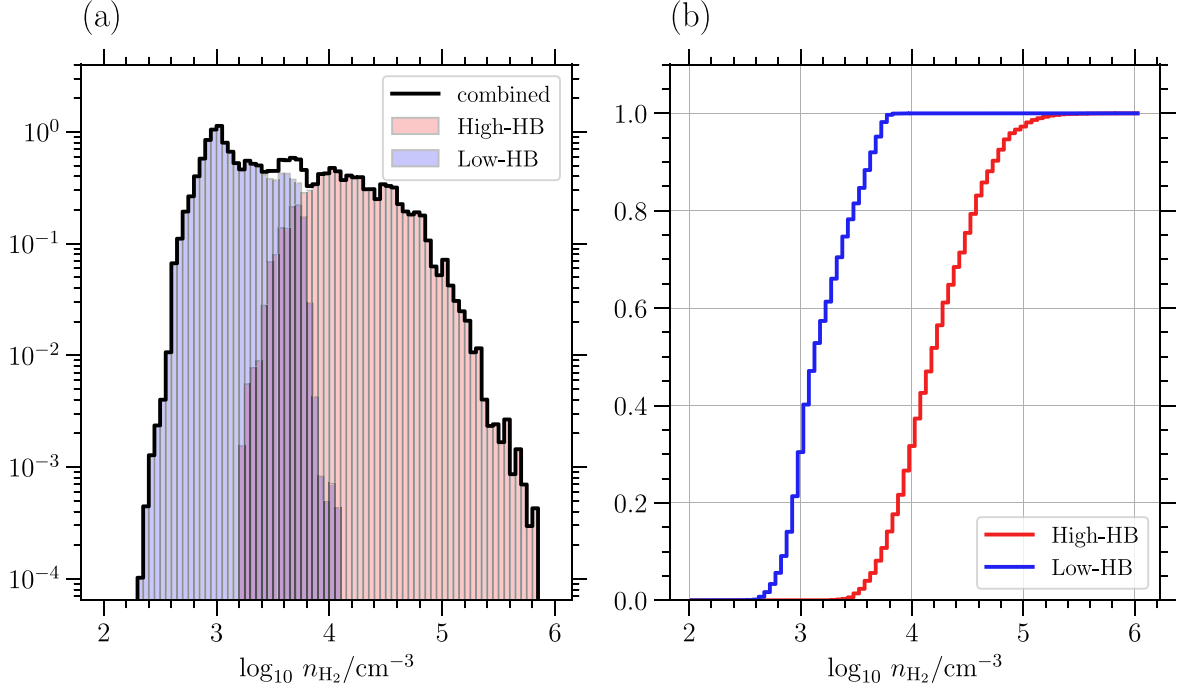


Figure 9. (a) Frequency histograms of n_{H_2} from the Low-HB (blue hatched) and High-HB (red hatched) results. The combined histogram using both results is shown in thick black lines. All histograms are weighted by $\langle N_{\text{H}_2} \rangle_{\text{beam}}$ and normalized by a common factor so that the integral of the combined histogram is unity. (b) Cumulative forms of the same n_{H_2} histograms as (a) but without the combined frequency. Normalization is independently applied to the Low-HB and High-HB plots so that the respective maxima are unity.

good spaxel-by-spaxel correlation with a correlation coefficient of $\gtrsim 0.8$, confirming the similarity in their P - P - V distributions we saw in Section 4.3. The consistency between the independent results from different data sets corroborates the validity of the HB analysis. The n_{H_2} scatter plot shows that n_{H_2} is higher for the High-HB results than for the Low-HB results at all spaxels. This confirms the assumption that the low- and high-density components do not spatially overlap in space, although they appear mixed in the 27 pc resolution. The overall similarity of the parameter behaviors indicates that the low-density and high-density components trace the consistent

molecular cloud structures, rather than being two isolated structures.

Figure 9(a) compares the histograms of n_{H_2} for the Low-HB and High-HB results along with the combined histogram for the two results, where the frequencies are weighted by $\langle N_{\text{H}_2} \rangle_{\text{beam}}$ and normalized by a common factor so that the integral of the combined histogram is unity. The figure shows that the mass fractions of the low- and high-density components are comparable at $n_{\text{H}_2} \sim 10^{3.8} \text{ cm}^{-3}$, above which n_{H_2} bins the high-density component dominates the gas mass. The cumulative n_{H_2} histograms for the Low-HB and High-HB

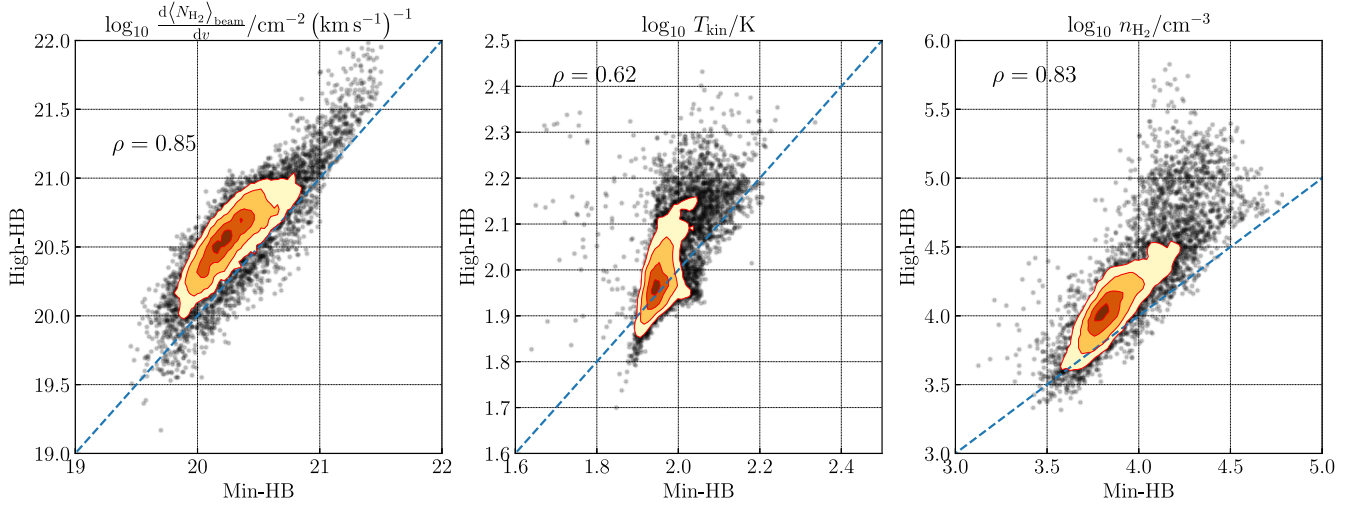


Figure 10. Same as Figure 8 but for the High-HB results vs. Min-HB results.

results are presented in Figure 9(b). The gas mass with $n_{\text{H}_2} > 10^{3.8} \text{ cm}^{-3}$ constitutes 87% of the mass traced by the High-HB result. Hence, we can consider $n_{\text{H}_2} = 10^{3.8} \text{ cm}^{-3}$ as the boundary between the two components.

4.6. High-HB versus Min-HB Analyses

Figure 10 compares $\langle N_{\text{H}_2} \rangle_{\text{beam}}$, T_{kin} , and n_{H_2} of the High-HB and Min-HB results in scatter plots. The two analyses target the same high-density component, and hence their results are ideally expected to agree with each other. The $\langle N_{\text{H}_2} \rangle_{\text{beam}}$ scatter plot follows a tight linear correlation between the High-HB and Min-HB though they use different N_{H_2} tracers (HNC 3–2 and ^{13}CO 2–1, respectively). This tight correlation confirms that ^{13}CO 2–1 can be used to *qualitatively* measure the N_{H_2} variation in the high-density component at the ALCHEMI resolution, as we assumed in Section 3.4. On the other hand, the High-HB $\langle N_{\text{H}_2} \rangle_{\text{beam}}$ values are consistently ~ 0.2 – 0.3 dex higher than the Min-HB values. This inconsistency indicates that ^{13}CO 2–1 intensity is inaccurate as a *quantitative* N_{H_2} tracer for the high-density component. We leave this inconsistency unsolved at present but will compare the masses based on the High-HB and Min-HB results with previous CO SLED and dust SED measurements in a later section (Section 5.2.1).

The T_{kin} scatter plot shows a relatively large dispersion, and the major part of the T_{kin} values are distributed in a narrow range from $10^{1.9}$ to $10^{2.1}$ K in the Min-HB result. The n_{H_2} scatter plot holds a good correlation, but the Min-HB analysis consistently yields ~ 0.2 dex lower values than the High-HB result. The n_{H_2} range is also slightly narrower in the Min-HB result. We note that the narrower variable ranges of T_{kin} and n_{H_2} in the Min-HB result may result from the stronger effect of the multivariate student prior, as the Min-HB results use a fewer number of observable intensities and hence the relative importance of the prior probability is larger. The multivariate student prior is a decreasing function of $|\Sigma|$, causing narrower parameter distributions (i.e., smaller variances or larger covariances) preferred if other conditions are equal. Hence, the High-HB result is likely to describe the dense-gas properties more reliably than the Min-HB result, as the former solution is more constrained by the observable information than by the prior probability. Indeed, a significant number of spaxels near the emission peaks were filtered out from the final physical

condition maps in the Min-HB analysis due to too broad credible intervals as we saw in Section 4.3 (Figure 7); this indicates that the Minimal data set is insufficient to fully solve the parameter degeneracy in the excitation analysis.

The two analyses for the GC, the GC-HB results and the results from T18, are compared in Appendix G.

4.7. Molecular Abundances and $[^{12}\text{C}]/[^{13}\text{C}]$ Ratios

As byproducts of the High-HB analysis, we obtained the x_{mol} distributions of HCN, HCO^+ , HNC, CS, HC_3N , N_2H^+ , SiO, $p - \text{H}_2\text{CO}$, and R_{13} in the high-density component. Figure 11 shows the P – P images of the velocity-integrated molecular abundances and R_{13} .

HCN, HCO^+ , and CS show relatively small abundance variations across the CMZ. The other four species, HC_3N , N_2H^+ , SiO, $p - \text{H}_2\text{CO}$, have similar spatial distributions, which increase outside the central starburst region and reach a maximum at the GMC1a near the southwestern edge of the CMZ. This trend is most clearly visible in SiO, which is an established tracer of fast shocks. HC_3N and $p - \text{H}_2\text{CO}$ are also tracers of slow shocks or known to be abundant in SF outflow sources (Jorgensen et al. 2004; Tafalla et al. 2010) and in widespread shocked clouds in the GC (Requena-Torres et al. 2006; T18). Hence, the outwardly increasing distribution of their abundances may indicate the relative importance of the shock chemistry in the outer region of the CMZ compared to the central starburst region, where UV and CR sources concentrate. The compact peak of $x_{\text{mol}}(\text{SiO})$ and $x_{\text{mol}}(\text{HC}_3\text{N})$ at GMC1a, in addition to the reported high HNC abundance (Huang et al. 2023), supports the suggestion that mechanical heating is important at GMC1a (Section 4.4). On the other hand, SF-related shocked gas in the inner GMCs (Huang et al. 2023) is not identified in the shock tracer distributions. Our result, however, does not necessarily indicate low abundances of shock tracer species in the inner GMCs, as it is likely that the shocked gas in the innermost region is not fully visible due to the selection criteria for the High-density data set, which exclude high-excitation transitions locally distributed in the inner GMCs. We will discuss this issue later (Section 5.1.4).

The $[^{12}\text{C}]/[^{13}\text{C}]$ isotopic ratio R_{13} is ~ 45 – 50 toward the central portion and ~ 60 for the GMCs in the outskirts regions.

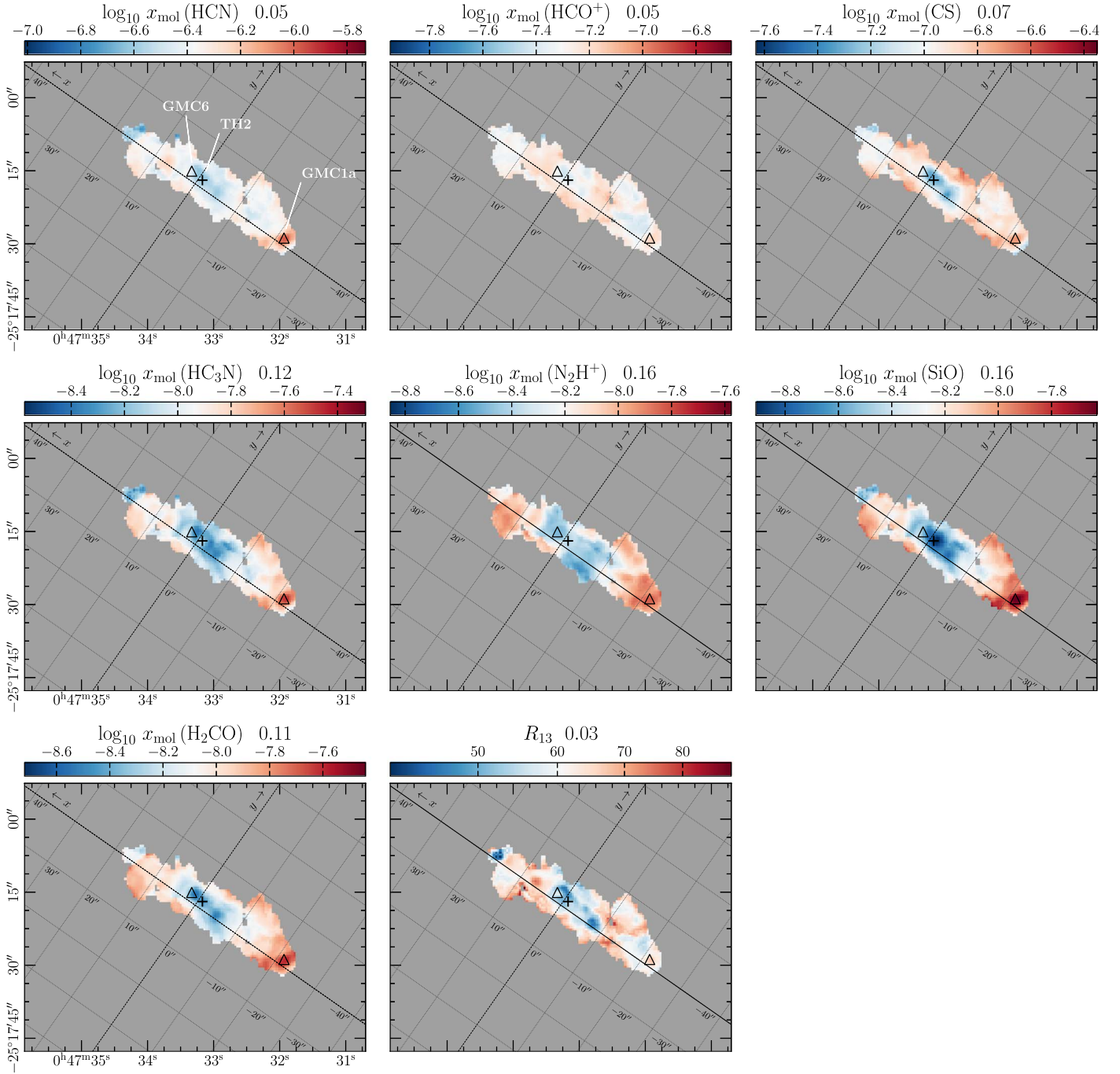


Figure 11. Velocity-integrated P - P distributions of the molecular abundances (x_{mol}) and the $^{12}\text{C}/^{13}\text{C}$ isotopic abundance (R_{13}) from the High-HB result. A common color bar range of 1.28 dex is used for all x_{mol} panels. The median absolute deviation is shown in each panel caption.

These values are close to those measured using CN (Henkel et al. 1993; Martín et al. 2010; Tang et al. 2019), CCH (Martín et al. 2010, 2021), and CH_3OH (Martín et al. 2021) transitions. The overall increasing gradient from the center to the outskirts is similar to that seen in the $^{12}\text{C}^{18}\text{O}/^{13}\text{C}^{18}\text{O}$ ratio (Martín et al. 2019). However, our R_{13} value is approximately a factor of 2–3 higher than those obtained from the $^{12}\text{C}^{18}\text{O}/^{13}\text{C}^{18}\text{O}$ ratio (Martín et al. 2019) and from individual fittings of the ALCHEMI Atacama Compact Array (ACA) data of the HCN, HCO^+ , and CS transitions (Martín et al. 2021), which range from 21 to 26. The inconsistency between the ACA result and ours, which use the same molecular transitions from the

ALCHEMI data, arises from the one-zone modeling adopted in the present analysis. The High-HB analysis yields a lower T_{kin} than the individual fittings of the HCN, HCO^+ , and CS transitions toward the central portion of the NGC 253 CMZ, as T_{kin} is primarily determined by the $p - \text{H}_2\text{CO } 3_{21-2_{03}} - 2_{02}$ ratio in the High-HB analysis. The lower T_{kin} leads to higher optical depths of the ^{12}C main isotopologues, and hence to a higher R_{13} value than the results of the individual fittings. We leave this inconsistency open to question in this paper, as our analysis is not specifically designed to accurately measure R_{13} . We just suggest that it is likely that R_{13} has a relatively high value of 45–60 when we adopt the one-zone model.

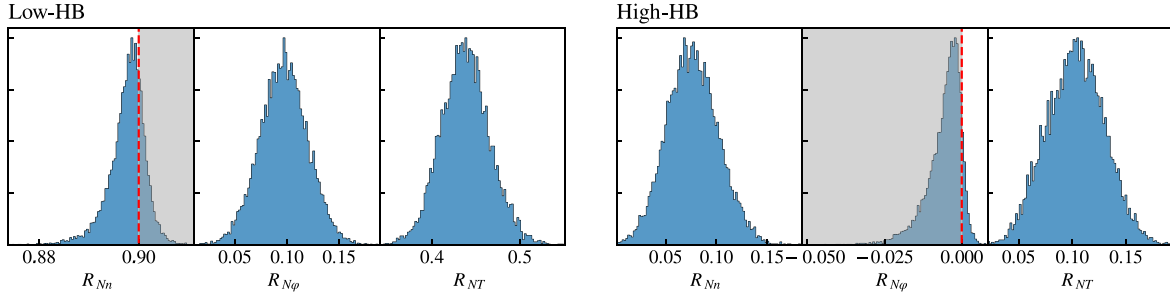


Figure 12. Marginal posteriors of R_{ij} elements in the Low-HB (left panel) and High-HB (right panel) runs. The subscript indices N , n , and T are for $\frac{dN_{H_2}}{dv}$, n_{H_2} , and T_{kin} , respectively. The gray hatched areas and the red vertical dashed lines denote the parameter ranges forbidden by the logistic hyperprior and their boundaries, respectively.

4.8. Verification of the Results of the Hierarchical Analysis

We verify the validity of the HB analyses by investigating the effects of the assumptions in the statistical and physical modelings. In the following, we discuss the effects of the logistic hyperprior, uncertainty in the Φ measurements in the Low-HB result, and the species-to-species variation in the excitation temperatures.

4.8.1. Effect of the Logistic Hyperprior

The present analysis uses logistic hyperprior to enforce $R_{Nn} > 0$, $R_{N\phi} > 0$, $R_{NT} > 0$, and $|R_{ij}| < 0.9$ for all (i, j) in the HB runs. Except for the nonnegative N_{H_2} – n_{H_2} correlation, these constraints are adopted for a computational reason rather than based on the physics of molecular clouds. These arbitrary assumptions can create nonphysical features in the analysis results.

Figure 12 shows the marginal posteriors of the hyperparameters R_{Nn} , $R_{N\phi}$, and R_{NT} in the Low-HB and High-HB runs. If their nonnegative values are enforced by the logistic hyperprior, the function shapes are expected to be truncated or skewed at the boundaries imposed by the hyperprior. Such a skewed shape is obtained for the R_{Nn} PDF of Low-HB. This indicates that the N_{H_2} – n_{H_2} degeneracy was not sufficiently solved even in the HB framework. As mentioned in Section 4.3, the multivariate student prior prefers solutions with higher correlation coefficients (or smaller dispersions) if other conditions are equal. Therefore, the HB analysis tends to create a tight correlation if the input data are insufficient to solve the parameter degeneracy.

The PDF of $R_{N\phi}$ in the High-HB result is skewed near 0, indicating that N_{H_2} and ϕ would be anticorrelated if the logistic hyperprior were absent. The median $\tilde{R}_{N\phi}$ (Table 5) is also slightly negative even with the explicit constraint by the logistic hyperprior. It is difficult to determine whether this anticorrelation is real; artificial N_{H_2} – Φ anticorrelation is easily created in solving the excitation equations, as all observable line intensities are approximated in the form $\propto \Phi \cdot N_{H_2}$. For example, an overestimation in N_{H_2} due to a deficiency in the physical or statistical modeling should be compensated by decreasing Φ . However, we may consider a positive N_{H_2} – Φ correlation to be physically more reasonable, as higher- N_{H_2} regions are likely to be more crowded with dense gas. For example, larger sizes of the subbeam structures such as clumps and filaments should increase both Φ and N_{H_2} , which are more likely to cause a positive N_{H_2} – Φ correlation than a negative correlation. If positive $R_{N\phi}$ is the case in the real clouds in the high-density component, the High-HB analysis possibly

overestimates N_{H_2} (and hence underestimates n_{H_2} and/or T_{kin}) in the high- N_{H_2} regions.

All other PDFs in Figure 12 do not have skewed or truncated posterior PDFs, indicating that their corresponding R_{ij} values are not enforced by the logistic hyperprior. In particular, it is noteworthy that the moderately positive R_{NT} values obtained for all HB analyses are likely to reflect the true physical conditions in the CMZ, rather than being enforced by the statistical modeling.

4.8.2. Uncertainty in the Beam-filling Factor

The median Φ value in the Low-HB result, 0.064, is lower than that in the High-HB result, 0.10, although we reasonably expect a wider spatial distribution for the lower-density component. Indeed, the CO SLED analysis by P18 shows that Φ of the first component is ~ 5 times that in the higher-density components measured for the central starburst region. The smaller Φ in the Low-HB result may indicate an unsuccessful decoupling of N_{H_2} and Φ due to the lack of the absolute intensities of optically thick lines in the Low-density data set.

We simulated the effect of underestimating Φ on the excitation analysis by performing NHB analyses using the Low-density data set for a range of fixed values of Φ . The input data were the median values of the line intensities and intensity ratios. The results are shown in Figure 13(a), where the medians of the marginal posteriors of $\frac{d\langle N_{H_2} \rangle_{\text{beam}}}{dv}$, n_{H_2} , and T_{kin} are plotted as a function of Φ in units of $\tilde{\mu}_{\Phi}$ of the Low-HB result ($\Phi_{\text{LowHB}} = 0.064$). The error bars are for the median absolute deviations of the marginal posteriors. Both the median n_{H_2} and T_{kin} do not significantly differ from the Low-HB results, and their dependence on Φ is within ~ 0.2 dex over the Φ/Φ_{LowHB} range of 1–5. This relative insensitivity of the T_{kin} and n_{H_2} estimates to the assumed Φ value is due to the fact that the Low-density set consists of absolute intensities of relatively optically thin lines (^{13}CO and C^{18}O transitions) and intensity ratios of optically thick lines (^{12}CO transitions), none of which depend strongly on Φ . The small variations in T_{kin} and n_{H_2} from Φ/Φ_{LowHB} of 2 to 5 are due to the weak dependence of the intensity ratios among the ^{12}CO transitions on N_{H_2} . The ^{13}CO transitions become moderately optically thick when $\Phi/\Phi_{\text{LowHB}} \leq 2$, causing the increase and decrease in T_{kin} and n_{H_2} , respectively, from Φ/Φ_{LowHB} of 2 to 1. The maximum deviation from the $\Phi = \Phi_{\text{LowHB}}$ case is found at $\Phi/\Phi_{\text{LowHB}} = 2$, at which T_{kin} and n_{H_2} are approximately 0.3 dex lower and 0.3 dex higher than the Low-HB values, respectively. These variations due to the varying Φ are small compared to the width of the posterior resulting from the

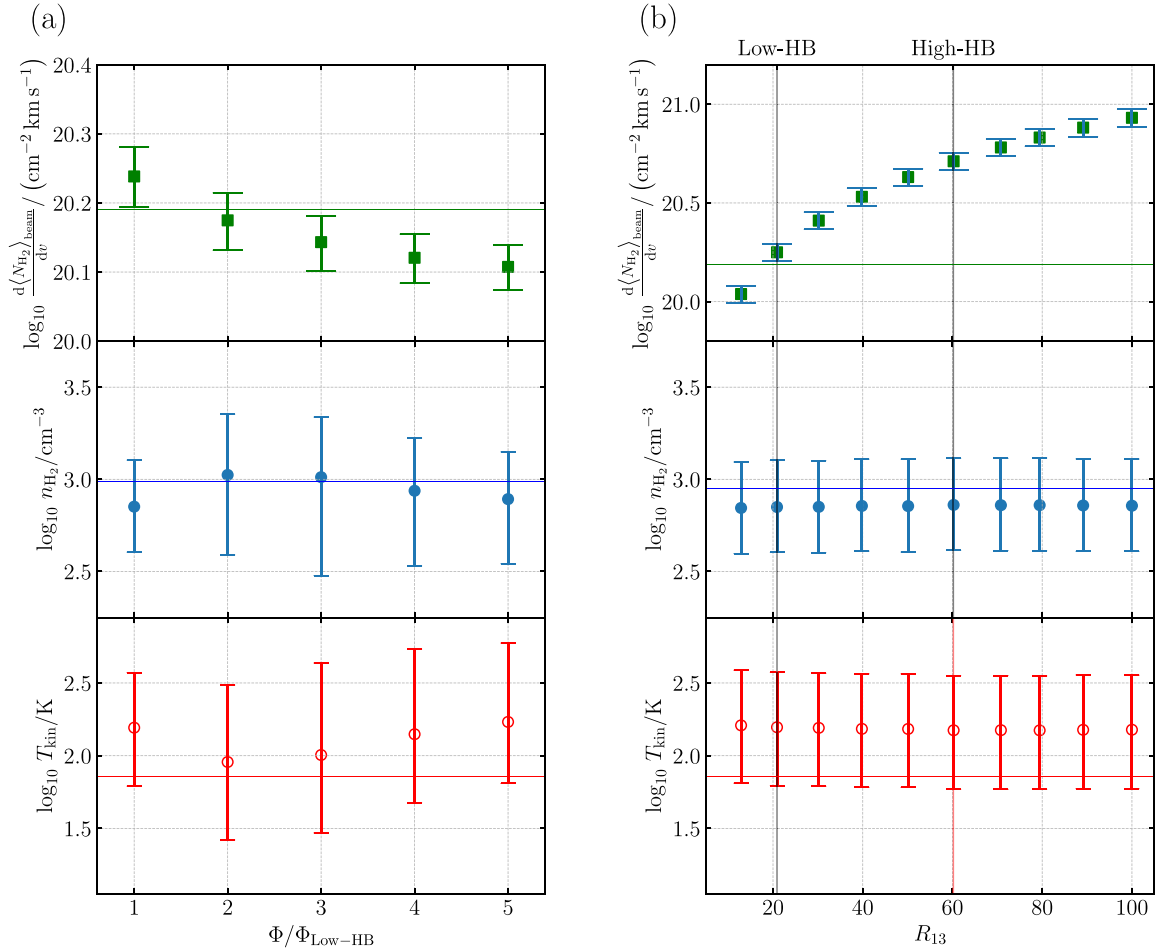


Figure 13. (a) Simulated effect of varying beam-filling factor Φ on the analysis with the Low-density set. The plot shows the median ($\frac{d\langle N_{\text{H}_2} \rangle_{\text{beam}}}{dv}$, n_{H_2} , T_{kin}) of the nonhierarchical posterior PDF calculated with the median intensities and intensity ratios of the Low-density set, where Φ is fixed. The error bars show the median absolute deviations of the marginal posteriors. The horizontal axis is Φ in units of $\tilde{\mu}_\Phi$ of the Low-HB analysis ($\Phi_{\text{LowH}} = 0.064$). The median $\frac{d\langle N_{\text{H}_2} \rangle_{\text{beam}}}{dv}$, n_{H_2} , and T_{kin} ($\tilde{\mu}_{\langle N \rangle}$, $\tilde{\mu}_n$, and $\tilde{\mu}_T$) from the Low-HB analysis are shown by horizontal lines. (b) Same as (a), but for varying fixed R_{13} . The R_{13} value assumed in the Low-HB analysis and $\tilde{\mu}_R$ obtained from the High-HB analysis are indicated by the vertical lines.

uncertainties in the input intensities, and therefore their effect on the final result should not be significant.

The assumption is that Φ has a small effect on $\langle N_{\text{H}_2} \rangle_{\text{beam}}$, as the ^{13}CO transitions become moderately optically thick for small Φ . $\langle N_{\text{H}_2} \rangle_{\text{beam}}$ is a factor of ~ 1.5 lower than the value with $\Phi = \Phi_{\text{Low-HB}}$ when $\Phi/\Phi_{\text{Low-HB}} = 5$. This could be a source of the uncertainty in the mass estimate of the low-density component, along with the uncertainties in $x_{\text{mol}}(\text{CO})$ and R_{13} .

4.8.3. Uncertainty in the $[^{12}\text{C}]/[^{13}\text{C}]$ Isotopic Abundance

The Low-HB analysis adopted R_{13} of 21 (Martín et al. 2019), but the reported $[^{12}\text{C}]/[^{13}\text{C}]$ ratio measured using the CO isotopologues ranges from 14 to 100 (Martín et al. 2021 and references therein). Figure 13(b) shows the variation of the median T_{kin} and n_{H_2} values calculated using the NHB analysis for varying fixed values of R_{13} , using the same analysis setup as in the previous subsection (Section 4.8.2), except that the beam-filling factor Φ is fixed at 0.064 to examine the effect of varying R_{13} independently from the effect of Φ . The $[^{13}\text{CO}]/[^{12}\text{C}^{18}\text{O}]$ abundance ratio is fixed at 6.1. This result shows that the T_{kin} and n_{H_2} values do not significantly vary within the reported R_{13} range in the literature. This insensitivity

of the excitation analysis to R_{13} is readily understood as a consequence of the omission of the absolute intensity scales of the ^{12}CO transitions in the present analysis. The R_{13} assumption has a relatively minor effect on the intensity ratios between the CO 1–0, 2–1, and 3–2 transitions via the photon-trapping effect, similar to the effect of Φ on the Low-HB analysis. Their effects are sufficiently small compared with the credible intervals from the uncertainty of the input data.

The assumption for R_{13} affects estimates of N_{H_2} and the mass of the low-density component, as N_{H_2} is approximately linearly scaled by $R_{13}^{-1}N_{^{13}\text{CO}}$. We will examine the validity of the derived total mass by comparing it with the masses based on the CO SLED and the dust SED in a later section (Section 5.2.1).

4.8.4. Species-to-species Variation in Excitation

As mentioned in Section 3.3, different lines in the High-density data set may be in different excitation conditions depending on their physical and chemical characteristics. To see this species-to-species variation, we performed nonhierarchical analyses using single molecular species toward the GMC6 and TH2 positions. We selected two transitions from six

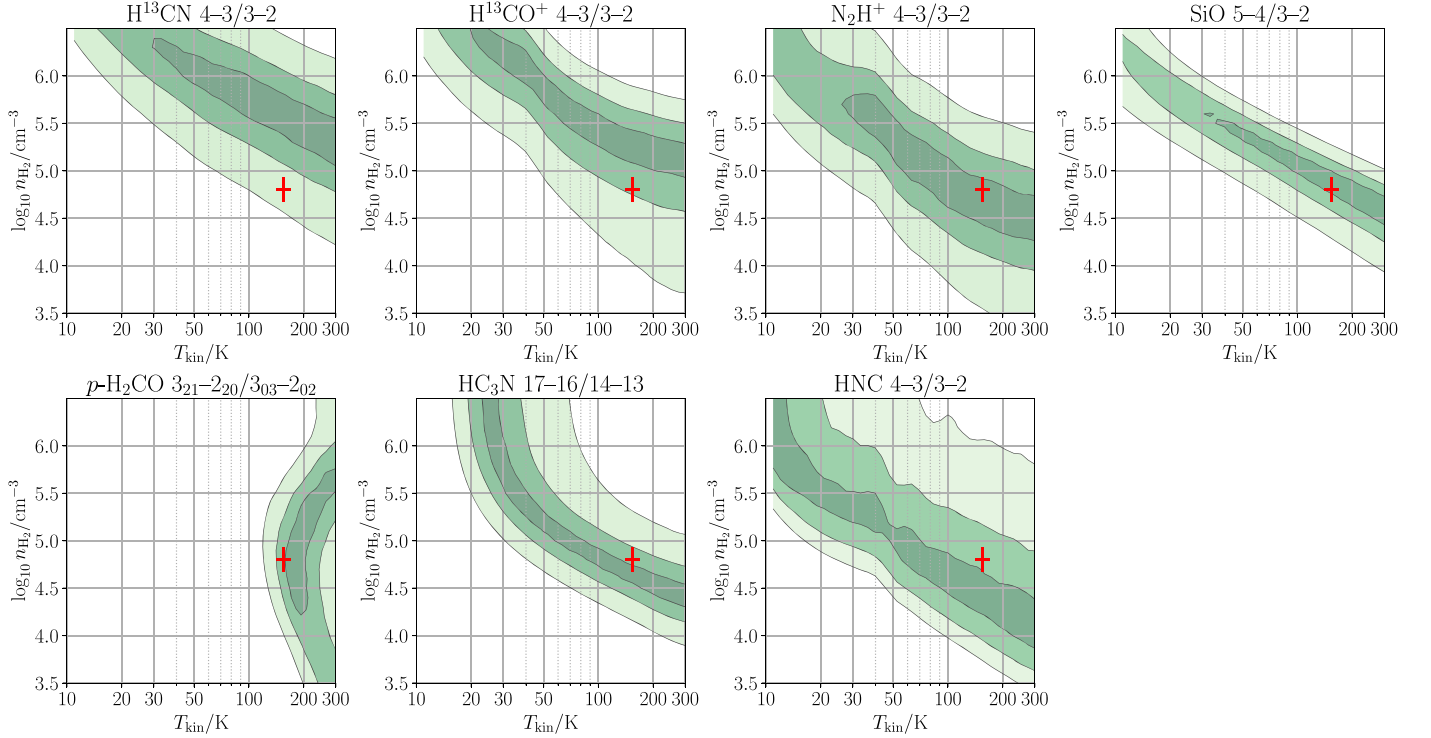


Figure 14. Comparison of the simple LVG results using different molecular species. The colored contours indicate the $(T_{\text{kin}}, n_{\text{H}_2})$ ranges calculated from the intensity ratios of individual molecular lines using simple LVG analysis. The transitions used in the analysis are indicated in the panel captions. The contours show 30%, 50%, and 80% credible intervals, calculated by assuming 15% relative uncertainties for all input line intensities. The T_{kin} and n_{H_2} values and their 50%-percentile errors from the High-HB analysis are indicated by cross marks.

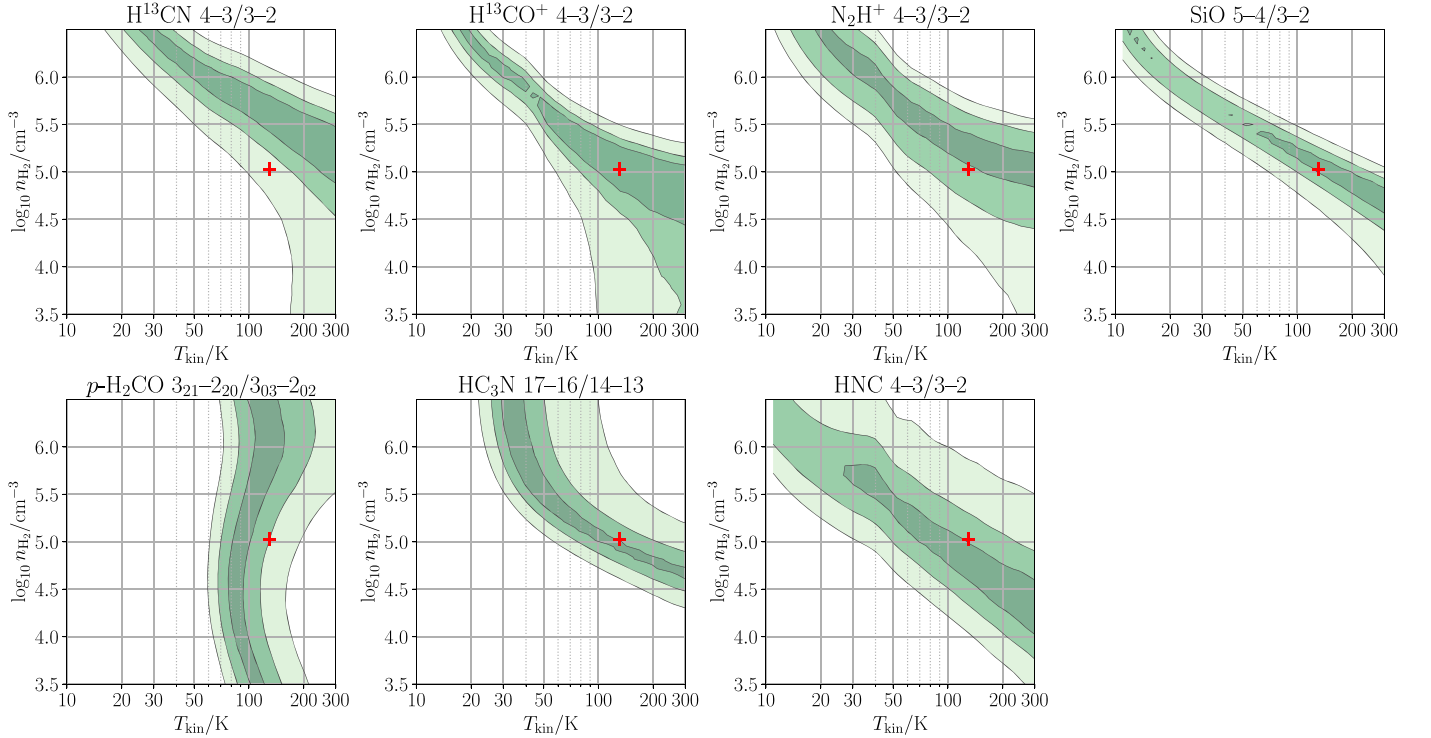


Figure 15. Same as Figure 14 but at the TH2 position.

different species (H^{13}CN , H^{13}CO^+ , SiO , N_2H^+ , HC_3N , $p-\text{H}_2\text{CO}$, and HNC), and ran independent analyses using their intensity ratio for each species assuming a 15% relative uncertainty for each line intensity. Spaxels at 200 km s^{-1} and 275 km s^{-1} are used for the GMC6 and TH2 positions,

respectively. Figures 14 and 15 show the posterior PDFs projected onto the $T_{\text{kin}}-n_{\text{H}_2}$ plane, with the 50% credible intervals of $(T_{\text{kin}}, n_{\text{H}_2})$ of the High-HB results. The transitions used are indicated by the panel captions. The posterior PDFs are calculated over the T_{kin} and n_{H_2} ranges of [10 K, 300 K] and

[$10^{3.5} \text{ cm}^{-3}$, $10^{6.5} \text{ cm}^{-3}$], respectively. The variation ranges of the molecular column densities ($=dN_{\text{H}_2}/dv \cdot x_{\text{mol}}(\text{X})$) are conservatively assumed to be ± 0.5 dex from the values in the High-HB result, as the photon-trapping effect affects the intensity ratios for optically thick cases. Nevertheless, we note that the changes in the intensity ratios due to the column density variation is at most comparable to the relative uncertainties of the intensities, 15%, even for the optically thickest transitions compared in Figures 14 and 15, i.e., HNC 3–2 and 4–3.

Comparison among the six analyses presented in Figures 14 and 15 shows that the H^{13}CN lines yield consistently higher T_{kin} and/or n_{H_2} values than the High-HB result toward both positions. The analysis with H^{13}CO^+ lines also results in slightly higher $T_{\text{kin}}/n_{\text{H}_2}$ toward GMC6. The 50%-credible intervals for other molecules are consistent with each other and with the High-HB result. This consistency is noteworthy because they consist of tracers of a wide variety of physical environments: a fast shock tracer (SiO), mild shock tracers (HC_3N and $p - \text{H}_2\text{CO}$; Jorgensen et al. 2004; Requena-Torres et al. 2006; Tafalla et al. 2010; T18), and quiescent gas tracers (HCO^+ and N_2H^+). The lack of a clear species-to-species difference in the physical conditions (except for HCN) may indicate that the variety in the chemical/physical environments is smoothed out in the spatial scale of our analysis ($1''.6 = 27 \text{ pc}$).

The higher excitation of the H^{13}CN lines could be understood as the consequence of their outstandingly high n_{crit} . The n_{crit} of H^{13}CN 3–2 and 4–3 are $\sim 10^{7.0} \text{ cm}^{-3}$ and $10^{7.2} \text{ cm}^{-3}$, respectively, whereas those of the highest transitions of other species used in the High-HB analysis are mostly in a relatively narrow range from $10^{6.4} \text{ cm}^{-3}$ to $10^{6.6} \text{ cm}^{-3}$ (except for HC_3N 17–16, whose n_{crit} is $10^{5.6} \text{ cm}^{-3}$); it is possible that the H^{13}CN lines are more affected by the highest-excitation component in the CO SLED (Pérez-Beaupuits et al. 2018) than other lines. We may also consider the IR-pumping effect for the HCN excitation (Sakamoto et al. 2010; Mills et al. 2013; Veach et al. 2013; Aalto et al. 2015), as vibrationally excited HCN, HNC, and HC_3N lines are detected by ALCHEMI and previous observations (Mangum et al. 2019; Rico-Villas et al. 2020; Martín et al. 2021). However, HNC and HC_3N do not show higher excitation than other molecular species. As the IR-pumping effect is stronger for HNC than for HCN (Behrens et al. 2022), this indicates that the IR-pumping effect does not dominate the molecular excitation on the spatial scale of the ALCHEMI data.

4.8.5. Summary of the Verification of the Analysis

The following summarizes caveats on the reliability of the Low-HB and High-HB results described in this and the previous subsections.

1. The High-HB analysis is likely to provide more accurate physical conditions of the high-density component than the Min-HB analysis; in particular, the narrow variable range of T_{kin} in the Min-HB result is possibly due to insufficient constraints from input data (Sections 4.6, 4.8.1).
2. The strong N_{H_2} – n_{H_2} correlation in the Low-HB results is at least partly due to the parameter degeneracy in the excitation analysis (Section 4.8.1). The Low-HB result is

also likely to underestimate Φ by a factor of a few, which may cause a $\lesssim 0.3$ dex underestimation in n_{H_2} and $\lesssim 0.3$ dex overestimation in T_{kin} (Section 4.8.2).

3. The assumption for the fixed R_{13} value in the Low-HB analysis does not significantly affect the output n_{H_2} and T_{kin} for the R_{13} range of 14–100 (Section 4.8.3). The High-HB analysis derived the R_{13} values ranging from ~ 45 to ~ 60 , which is 2–3 times higher than the Low-HB value and the values in Martín et al. (2021). These high R_{13} values result from our adoption of a one-zone approximation, which yielded higher optical depths for the HCN, HCO^+ , and CS transitions than Martín et al. (2021), who performed independent fittings for each species (Section 4.7).
4. Local N_{H_2} – T_{kin} (and n_{H_2} – T_{kin}) anticorrelation among high-velocity spaxels for the Low-HB and High-HB results is possibly an artifact created by insufficient resolution of the parameter degeneracy. Nonetheless, the similarity between the Low-HB and High-HB T_{kin} images may suggest that their overall T_{kin} distributions are real (Section 4.3).
5. The High-HB analysis is likely to underestimate Φ (and hence overestimate N_{H_2}) in high- N_{H_2} regions, which possibly causes an underestimation of n_{H_2} and/or T_{kin} there (Section 4.8.1).
6. The IR-pumping effect is unlikely to significantly affect the High-HB results (Section 4.8.4).
7. The absolute N_{H_2} and $\langle N_{\text{H}_2} \rangle_{\text{beam}}$ values linearly depend on the assumed abundances of CO and HNC ($x_{\text{mol}}(^{12}\text{CO}) = 10^{-4}$ and $x_{\text{mol}}(\text{HNC}) = 4 \times 10^{-8}$ in the present analysis), which requires caution when comparing them with other measurements of N_{H_2} and gas mass (Sections 3.5, 4.8.3). The uncertainties in Φ and R_{13} in the Low-HB analysis are additional sources of uncertainty in the mass estimate for the low-density component (Sections 4.8.2, 4.8.3). We will show that the present analysis provides molecular gas mass consistent with previous results based on CO SLED and dust SED analyses in Section 5.2.1).

5. Discussion

5.1. Comparison with Excitation Analyses in Previous Studies

Measurements of T_{kin} and n_{H_2} toward the NGC 253 CMZ were performed in previous studies through analysis of H_2CO transitions (Mangum et al. 2019), CO SLEDs (R14; P18), and NH_3 inversion transitions (Takano et al. 2002; Ott et al. 2005; Takano et al. 2005; Mangum et al. 2013; Gorski et al. 2017), as well as in other ALCHEMI studies (Holdship et al. 2021; Behrens et al. 2022; Humire et al. 2022; Huang et al. 2023). This subsection compares our results of n_{H_2} and T_{kin} measurements with those previous results.

5.1.1. $p - \text{H}_2\text{CO}$ Results

A GMC-scale T_{kin} measurement toward the CMZ of NGC 253 was performed using multitransition H_2CO lines by Mangum et al. (2019). Their results show that warm gas with T_{kin} ranging from 50 to $\gtrsim 150 \text{ K}$ is extended on $\gtrsim 5''$ scales, which is primarily traced by the $p - \text{H}_2\text{CO}$ 3₂₁–2₂₀ and 3₀₃–2₀₂ transitions. The High-HB results in the present study are well

consistent with this warm component, as a natural consequence that the High-density data set contains the same $p - \text{H}_2\text{CO}$ lines as in Mangum et al. (2019). The widespread distribution of the low-excitation $p - \text{H}_2\text{CO}$ lines in Mangum et al. (2019) and the ALCHEMI data supports our assumption that they are not localized to specific environments such as hot cores and outflows and hence can be used as T_{kin} probes on GMC scales, similar to the situation in the GC (Ao et al. 2013; Ginsburg et al. 2016). It is also noteworthy that this warm gas is the lowest- T_{kin} component identified by the multitransition H_2CO study. Their relatively low upper-state energies ($E_u/k_B = 21$ K and 68 K for $3_{21}-2_{20}$ and $3_{03}-2_{02}$, respectively) confirm that colder gas than detected with the High-HB analysis, if any, is unlikely to be a major dense-gas component of the CMZ of NGC 253.

5.1.2. CO SLED Analyses

Two CO SLED analyses toward the CMZ of NGC 253 were reported in the literature: R14 using ^{12}CO lines up to the 13–12 transition and ^{13}CO lines up to the 6–5 transition toward the central $32''.5$ region, and P18 using ^{12}CO lines up to the 19–18 transition toward the central $40''$ region. The two analyses consistently show the presence of three CO components. The low- and high-density components in the present analysis should approximately correspond to the first and second CO components, respectively. The results for the lowest-density component of the two CO SLED analyses are approximately consistent with each other and with the Low-HB result, as reasonably expected, as all three results are primarily determined by up to the 3–2 transitions of CO. The T_{kin} , n_{H_2} values of the first component are 60 K, $10^{3.5} \text{ cm}^{-3}$ in R14, and 90 ± 10 K, $10^{3.2 \pm 0.1} \text{ cm}^{-3}$ in P18. The mass-weighted average of the Low-HB result over the central $40''$ diameter region is T_{kin} , $n_{\text{H}_2} = 120$ K, $10^{3.4} \text{ cm}^{-3}$. The higher T_{kin} in the Low-HB result than the CO SLED could be explained by the contribution from the second CO component.

For the second CO component, R14 provides the best-fit T_{kin} and n_{H_2} values of 40 K and $10^{4.5} \text{ cm}^{-3}$, respectively, whereas P18 provides T_{kin} , $n_{\text{H}_2} = 50 \pm 3$ K, $(3.2 \pm 0.8) \times 10^5 \text{ cm}^{-3}$. The High-HB result yields T_{kin} , $n_{\text{H}_2} = 100$ K, $10^{4.4} \text{ cm}^{-3}$ for the central $40''$ region, which does not critically differ from the R14 result; although the T_{kin} of the High-HB result is more than a factor of 2 higher than the best-fit R14 result, it is within the uncertainty due to $T_{\text{kin}}-n_{\text{H}_2}$ degeneracy of their solution (presented in Figure 2 in their paper). The difference between the P18 and High-HB results is greater than the uncertainties estimated by P18, though no degeneracy plot is provided in their paper. However, the observed ^{12}CO 10–9/9–8 and 11–10/10–9 brightness temperature ratios in P18, which are 0.64 ± 0.09 and 0.60 ± 0.09 , respectively, are similar to those calculated from the High-HB results, which are 0.77 and 0.65, respectively; those three CO transitions are dominated by the second CO component in P18. Hence, we may consider the $T_{\text{kin}}-n_{\text{H}_2}$ degeneracy in the CO SLED analysis as a possible cause of the inconsistency between the P18 and High-HB results, too. The higher- T_{kin} solution is preferred by the multitransition $p - \text{H}_2\text{CO}$ study (Mangum et al. 2019), as discussed above. The $p - \text{H}_2\text{CO}$ results in Figures 14 and 15 indicate that the T_{kin} of the high-density gas cannot be substantially lower than ~ 100 K. The High-density data set and the CO SLEDs by R14 and P18 can be consistently

fitted by assuming that warm ($T_{\text{kin}} \sim 10^2$ K) and moderately dense ($n_{\text{H}_2} \sim \text{a few } 10^4 \text{ cm}^{-3}$) components dominate the second CO component. Therefore, the High-HB result should more accurately represent the physical conditions of the second CO component or the high-density component in the present analysis.

5.1.3. NH_3 Inversion Transition Study

Measurements of T_{kin} were also performed by using the NH_3 inversion lines (Takano et al. 2002, 2005; Ott et al. 2005; Mangum et al. 2013; Gorski et al. 2017, and references therein), most of which show multitemperature components. The NH_3 analysis consistently shows a warm gas component with $T_{\text{kin}} \sim 70\text{--}150$ K, though the number of the components and their T_{kin} values differ depending on transitions used, calculation methods, and position/velocities. Cross comparison between the NH_3 studies and the present analysis is not straightforward as n_{H_2} is poorly constrained by the NH_3 inversion lines while the low- and high-density components in the present analysis are degenerate in the T_{kin} range. We confirm that the $T_{\text{kin}} \sim 80\text{--}100$ K of the Low-HB and High-HB results are approximately consistent with that of this warm NH_3 component. The cold NH_3 gas with T_{kin} of 20–50 K reported in a few studies (Takano et al. 2002, 2005; Mangum et al. 2013) is not consistent with either typical T_{kin} values of the low- or high-density components. This cold gas component might represent the regions offset from the dynamical center by $\gtrsim 10''$ along the major axis, where $T_{\text{kin}} \sim 10^{1.5-1.7}$ K in the Low-HB result (see Figure 5).

5.1.4. Other ALCHEMI Studies

Measurements of n_{H_2} were performed using various molecular transitions in previous ALCHEMI studies toward representative GMC positions (Holdship et al. 2021; Behrens et al. 2022; Humire et al. 2022; Huang et al. 2023). Figure 16 presents scatter plots comparing the n_{H_2} measurements from the High-HB result with those from the analyses of HCN and HNC (Behrens et al. 2022), SiO and HNCO (Huang et al. 2023), C_2H , (Holdship et al. 2021) and H_3O^+ and SO (Holdship et al. 2022). They all adopt the nonhierarchical Bayesian framework as the statistical modeling method. Holdship et al. (2022) and Behrens et al. (2022) use chemical modeling in addition to radiative transfer modeling for parameter inference. The inner GMCs in the central starburst region and the outer GMCs in the outskirts of the CMZ are denoted by different symbols in Figure 16. Although many of these previous analyses estimate T_{kin} simultaneously with n_{H_2} , we do not compare the T_{kin} results, as their error bars are too large to make meaningful comparisons with the High-HB result.

Figure 16 shows that the majority of the n_{H_2} values measured by Behrens et al. (2022), Holdship et al. (2021), and Holdship et al. (2022) agree with the High-HB result within the error bars, except for a few GMCs with $\gtrsim 0.5\text{--}1$ dex higher n_{H_2} than the High-HB results. Hence, their analyses are likely to probe the approximately same n_{H_2} range as the High-HB analysis. The HNCO result by Huang et al. (2023) for the outer GMCs also agrees with the High-HB n_{H_2} values. However, the HNCO-based n_{H_2} values are significantly higher than the High-HB values for the inner GMCs. This inconsistency for the inner GMCs can be attributed to a larger contribution from the highest-excitation component in the HNCO analysis in

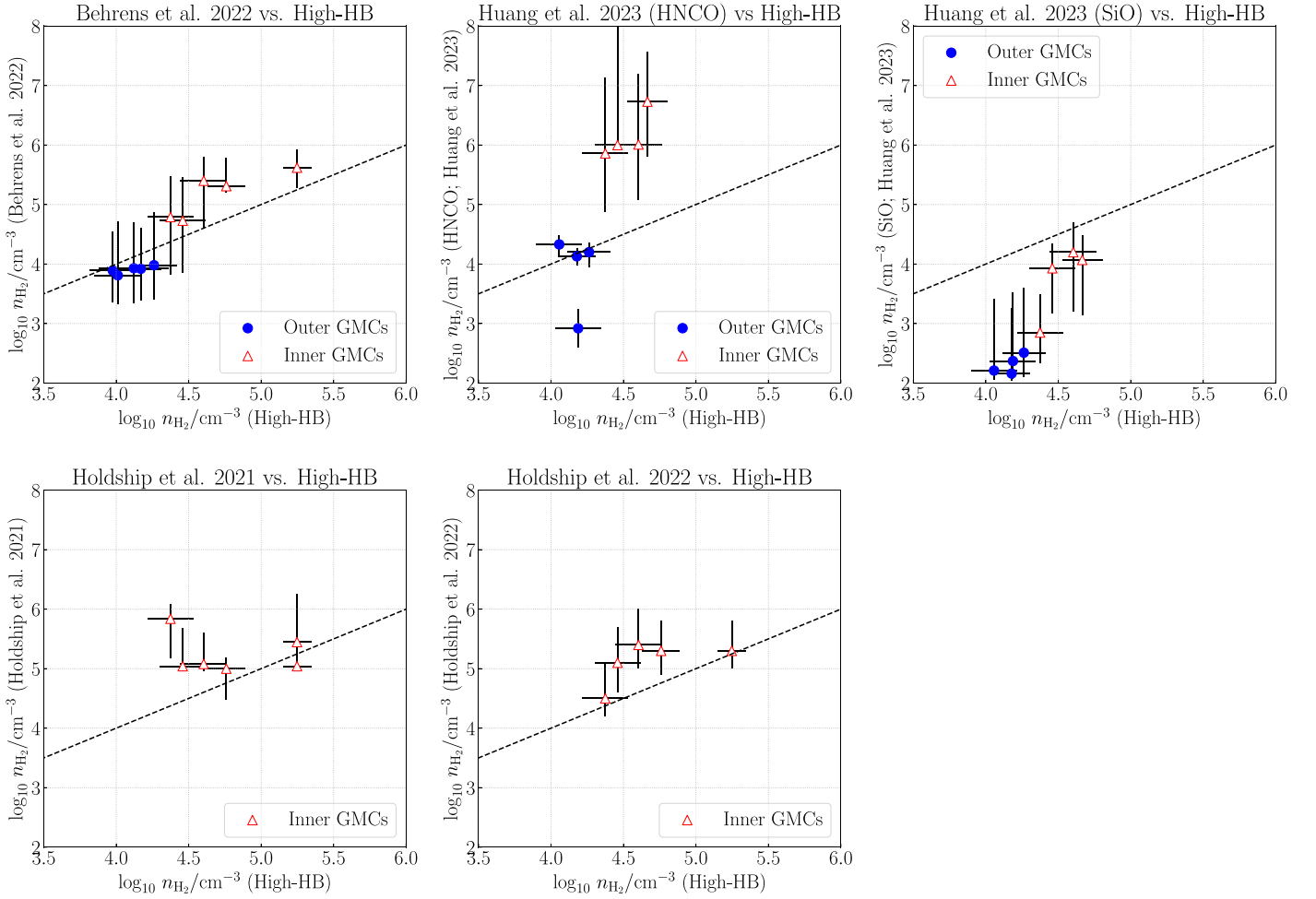


Figure 16. Scatter plots of n_{H_2} at the GMC positions from the High-HB results vs. those from other ALCHEMI analyses (Holdship et al. 2021; Behrens et al. 2022; Huang et al. 2023). The HNCO and SiO results by Huang et al. (2023) are presented in separate panels. The GMCs inside and outside the central starburst region (the inner and outer GMCs in the text, respectively) are denoted by open rectangles and filled circles, respectively. The dashed lines are the $y = x$ lines.

Huang et al. (2023). They used transitions with up to E_u/k_B of 126 K, whereas the High-density data set excludes transitions with $E_u/k_B > 70$ K to avoid confusion from the highest-excitation component. Indeed, intense emission from the high- J ($J \geq 12$ –11) HNCO transition with $E_u/k_B \gtrsim 80$ K is limited to the vicinity of the inner GMC where hot molecular gas associated with the starburst is expected, whereas the lower- J ($J \leq 10$ –9) transitions are widespread over the entire CMZ (Huang et al. 2023). Thus, the above three n_{H_2} measurements are consistent with the High-HB result except for the overlap of the central highest-excitation component in the HNCO results, despite the difference in the tracer lines and the parameter inference method.

On the other hand, Figure 16 shows that the SiO result by Huang et al. (2023) gives significantly lower n_{H_2} than the High-HB and other ALCHEMI results across all GMCs. Their T_{kin} ranges from 100 to 700 K, which is substantially higher than the High-HB result. Humire et al. (2022) reported the detection of methanol emission from gas with $T_{\text{kin}}, n_{\text{H}_2} \sim 25$ K, $10^{8.4} \text{ cm}^{-3}$ near the northeastern end of the CMZ. These low- n_{H_2} –high- T_{kin} or high- n_{H_2} –low- T_{kin} gas components that are visible in particular species are difficult to detect with the High-HB analysis, which assumes a nonnegative n_{H_2} – T_{kin}

correlation and the one-zone LVG modeling. However, it is likely that such gas components occupy a minor fraction of the dense-gas mass in the NGC 253 CMZ, as discussed above (Sections 5.1.1, 5.1.2).

Comparison between the present analysis and Huang et al. (2023) allows for an assessment of the widespread shock chemistry in the NGC 253 CMZ. Huang et al. (2023) discuss multiple origins of the shocked gas, which can be classified into SF-related (starburst scenario and sporadic SF episode scenario) and non-SF-related (cloud–cloud collision scenario) origins. The above multicomponent HNCO emission confirms the coexistence of such a multicomponent shocked gas. The low- J HNCO transition represents the same high-density component as that analyzed in the High-HB analysis. The high-density tracer molecules (SiO, p – H_2CO , and HC_3N) in this widespread shocked gas increase with increasing galactic radius (Section 4.7). This spatial distribution suggests that they originate from shocked gas of non-SF origin, i.e., shock associated with cloud–cloud collisions or SN-driven shocks. The high- J HNCO transitions represent the highest-excitation component in the CO SLEDs. Their spatial distribution is restricted to the inner GMCs, indicating that this component is associated with active SF there.

Table 6
Molecular Gas Properties and Star Formation Rates of the NGC 253 CMZ and the GC

			NGC 253 CMZ	GC ($ l < 1^\circ$, $ b < 0.5^\circ$)	Notes
Low-density component	\bar{n}_{H_2}	(cm^{-3})	$10^{3.3}$	10^3	^a
	\bar{T}_{kin}	(K)	85	30	^a
	M_{gas}	($10^8 M_\odot$)	1.6	0.29	^{a,c}
High-density component	\bar{n}_{H_2}	(cm^{-3})	$10^{4.4} / 10^{4.1}$	$10^{4.2} / 10^{4.0}$	^b
	\bar{T}_{kin}	(K)	109 / 106	83 / 93	^b
	M_{gas}	($10^8 M_\odot$)	1.1 / 0.59	0.040 / 0.029	^{b,c}
Total	M_{gas}	($10^8 M_\odot$)	2.7/2.2	0.33/0.32	^b
f_{DG}^*			0.40 / 0.27	0.13 / 0.09	^b
SFR		($M_\odot \text{ yr}^{-1}$)	2.8	0.012	^d
SFE		(10^{-8} yr^{-1})	1.0 / 1.3	0.036 / 0.038	^b
SFE _{DG}		(10^{-8} yr^{-1})	2.5 / 4.7	0.30 / 0.41	^b

Notes.

^a From the Low-HB results and Tanaka et al. (2021) for the NGC 253 CMZ and the GC, respectively.

^b Two estimates from different analyses are given for each of the NGC 253 CMZ and the GC, denoted as X/Y ; X is from the High-HB and T18 results and Y is from the Min-HB and GC-HB results.

^c M_{gas} of the GC is derived from the dust and molecular line data in Marsh et al. (2017), Ginsburg et al. (2016), and T18. See Section 5.2.1 for details.

^d From free-free emission at ~ 30 GHz, taken from Ott et al. (2005) and Longmore et al. (2013) for NGC 253 and the GC, respectively.

5.2. NGC 253 versus GC

In the following, we compare the primary molecular gas properties of the NGC 253 CMZ and the GC, such as the masses, SFRs, and dense-gas mass fraction (f_{DG}^*). The dense-gas mass fraction is defined as the mass ratio of the high-density component to the total mass; the asterisked symbol is used to underline the difference from the commonly used definition based on the HCN/CO luminosity ratio (e.g., Gao & Solomon 2004). In addition to these integral quantities, we will use the spatially resolved information to explore the difference characterizing the centers of the two galaxies. We introduce a new parameter, the modified dense-gas fraction $f_{\text{DG}}^*(n)$, in Section 5.2.5. This parameter represents f_{DG}^* redefined as a function of the threshold n_{H_2} defining the “dense gas.” We mainly refer to the Low-HB, High-HB, and T18 results in the discussion, but also use the Min-HB and GC-HB results where the precise comparison between the two regions is necessary.

5.2.1. Molecular Gas Mass and Dense-gas Mass Fraction

Table 6 tabulates the mass estimates of the low- and high-density components for the NGC 253 CMZ and the GC, along with their respective typical n_{H_2} and T_{kin} . The averaged n_{H_2} and T_{kin} of the Low-HB and High-HB results are shown for the NGC 253 CMZ. The T_{kin} and n_{H_2} values are taken from Tanaka et al. (2021) for the low-density component of the GC, and calculated based on the T18 result for the high-density component.

The low- and high-density component masses for the NGC 253 CMZ are obtained by integrating $\langle N_{\text{H}_2} \rangle_{\text{beam}}$ for the Low-HB and High-HB results, respectively. The total molecular gas mass, i.e., the sum of the low- and high-density gas masses, is $2 \times 10^8 M_\odot$ on the assumption that the overlap between the gas traced by the Low-HB and High-HB analyses is negligible. This is consistent with the mass estimates from multicomponent dust SED analysis ($3 \times 10^8 M_\odot$ in the central $30'' \times 16''$ region from Weiß et al. (2008) and $4.5 \times 10^8 M_\odot$ within the central $40''$ diameter from P18) considering uncertainties in the CO and HNC abundances and dust-to-gas ratio.

For the GC, the low- and high-density gas masses were calculated using the ^{13}CO 2–1 flux (Ginsburg et al. 2016) and $\langle N_{\text{H}_2} \rangle_{\text{beam}}$ maps by T18, respectively; the ^{13}CO 2–1-to-mass scaling factor was calculated assuming $T_{\text{kin}} = 30$ K, $n_{\text{H}_2} = 10^3 \text{ cm}^{-3}$, and $[^{13}\text{CO}]/[\text{H}_2] = 10^{-5.34}$ (Tanaka et al. 2018). The difference in the spatial coverage between T18 and the ^{13}CO 2–1 data was corrected by extrapolating them to the entire GC ($|l| \leq 1^\circ$, $|b| \leq 0.5^\circ$) on the assumption of constant dust-to-gas ratio each for the low- and high-density components. The HiGAL column density map (Marsh et al. 2017) was used as the reference dust mass distribution. The sum of the low-density and high-density gas masses, $3.3 \times 10^7 M_\odot$, was confirmed to be the same as that obtained by integrating the HiGAL map.

The dense-gas mass fractions f_{DG}^* of the NGC 253 and the GC are also compared in the table. The boundary of n_{H_2} separating the low- and high-density components is $\sim 10^{3.8} \text{ cm}^{-3}$ for the NGC 253 CMZ (Section 4.5). The n_{H_2} boundary for the GC can be assumed as $\sim 10^{3.5} \text{ cm}^{-3}$, as the average n_{H_2} of the GC is ~ 0.3 dex lower than that of the NGC 253 CMZ for both the low- and high-density components. This assumption is supported by the comparison of the n_{H_2} frequency histograms based on the measurements using CO lines (Nagai et al. 2007) and high-density tracer lines (T18) for the GC. The f_{DG}^* value of 0.40 from the High-HB result is consistent with those based on the CO SLED and dust SED, which are 0.29 ± 0.09 and 0.4 ± 0.2 , respectively (P18), which supports our assumption that $x_{\text{mol}}(\text{CO}) = 10^{-4}$ and $x_{\text{mol}}(\text{HNC}) = 4 \times 10^{-8}$.

The above results confirm the previous results showing that the NGC 253 CMZ is approximately an order of magnitude larger than the GC in mass both for the low- and high-density components (Paglione et al. 1995; Sakamoto et al. 2011; Leroy et al. 2015). The dense-gas mass fraction f_{DG}^* in NGC 253 CMZ is ~ 3 times that in the GC.

Table 6 also shows mass estimates and averaged T_{kin} and n_{H_2} calculated using the Min-HB and GC-HB results, which yield dense-gas masses that are a factor of 0.54 smaller and 1.4 larger than the High-HB and GC-HB results for the NGC 253 CMZ and the GC, respectively. The inconsistency between the dense-gas masses from the High-HB and Min-HB results should mainly originate from the different N_{H_2} tracers used in them (HNC 3–2 and ^{13}CO 2–1 in the High-HB and Min-HB analysis, respectively) as mentioned in Section 4.6. The f_{DG}^* value of 0.27 for the NGC 253 CMZ is lower than that based on the High-HB result, but still consistent with that from the CO SLED and dust SED (P18). The f_{DG}^* ratio between the Min-HB and GC-HB results is 1.7, which is a factor of 2 smaller than that from the High-HB and T18 results.

5.2.2. HCN/Dense-gas Mass Conversion Factor

The mass estimate with the High-HB result yields the ^{12}CO -to- H_2 conversion factor $X(\text{CO})$ of $0.7 \times 10^{20} \text{ cm}^{-2}/(\text{K km s}^{-1})$ for all of the CO 1–0, 2–1, and 3–2 transitions. This is lower than the canonical value of $2 \times 10^{20} \text{ cm}^{-2}/(\text{K km s}^{-1})$ as expected for starburst galaxies (Bolatto et al. 2013), and within the range of $X(\text{CO})$ estimated for the NGC 253 CMZ, $(0.3\text{--}4) \times 10^{20} \text{ cm}^{-2}/(\text{K km s}^{-1})$ (Mauersberger et al. 1996; Martín et al. 2010; Weiß et al. 2008). The HCN 1–0-to- H_2 conversion factor for the high-density component, $X(\text{HCN})$, is $2 \times 10^{20} \text{ cm}^{-2}/(\text{K km s}^{-1})$. This $X(\text{HCN})$ value translates into the HCN luminosity-to-dense-gas-mass conversion factor $\alpha(\text{HCN})$ of $4 M_\odot \text{ pc}^{-2}(\text{K km s}^{-1})^{-1}$, which is a factor of 2.5–3.5 lower than frequent values in extragalactic surveys ($10\text{--}14 M_\odot \text{ pc}^{-2}(\text{K km s}^{-1})^{-1}$; Gao & Solomon 2004; Onus et al. 2018; Neumann et al. 2023).

It is noteworthy that the above conversion factors for the NGC 253 CMZ are consistent with those calculated for the GC using the T18 result: $X(\text{CO}) = 0.6 \times 10^{20} \text{ cm}^{-2}/(\text{K km s}^{-1})$, and $X(\text{HCN}) = 2 \times 10^{20} \text{ cm}^{-2}/(\text{K km s}^{-1})$. This consistency confirms that f_{DG} defined as the HCN/CO luminosity ratio is indeed a good measure of f_{DG}^* based on the mass estimates. However, we note that the High-HB result contains a wide range of n_{H_2} from $10^{3.2} \text{ cm}^{-3}$ to $10^{5.8} \text{ cm}^{-3}$ as shown in Figure 9, and $\sim 70\%$ of the total mass is constituted by the spaxel with $n_{\text{H}_2} < 3 \times 10^4 \text{ cm}^{-3}$. Furthermore, the actual HCN 1–0 emitting gas in the NGC 253 CMZ contains a significant amount of even lower- n_{H_2} gas, as 35% of the HCN 1–0 flux originates outside the coverage of the High-HB analysis as we have seen in Section 4.1. Therefore, our n_{H_2} measurement is consistent with the recent arguments against HCN 1–0 luminosity being a reliable tracer of molecular gas mass with $n_{\text{H}_2} \sim 3 \times 10^4 \text{ cm}^{-3}$ (e.g., Onus et al. 2018; Jones et al. 2023).

5.2.3. Star Formation Rates and Star Formation Efficiencies

We show the SFRs of the NGC 253 and MW CMZs taken from the literature, which are measured using the free-free emission in the ~ 30 GHz band (Longmore et al. 2013; Ott et al. 2005) in Table 6. Two SFEs were calculated by dividing the SFR by the mass of either the total molecular gas or the dense molecular gas; we denote the latter as SFE_{DG} . The SFE of NGC 253 is ~ 30 times that of the GC, whose difference is substantially greater than the factor of 2–3 difference in f_{DG}^* between them. The SFE_{DG} of NGC 253 is more than an order of magnitude higher than that of the GC. This difference is significant even when the uncertainty in the mass estimates, which is a factor of $\sim 2\text{--}3$ in P18, is considered.

These results do not conform with a simple picture that the SFR is scaled by the mass of the dense-gas component, at least between the NGC 253 CMZ and the GC. A similar result is reported for the comparison between the GC and the circumnuclear ring of M83 (Callanan et al. 2021); their difference in the dense-gas mass based on the HCN 1–0 luminosity is a factor of ~ 2 , in spite of the order-of-magnitude higher SFR of the M83 circumnuclear ring.

5.2.4. Frequency Distributions of N_{H_2} , n_{H_2} , and T_{kin}

Figure 17 compares the histograms of $\langle N_{\text{H}_2} \rangle_{\text{beam}}$ -weighted frequencies of N_{H_2} , T_{kin} , and n_{H_2} of the high-density components of NGC 253 and the GC. The comparison is made using two analysis pairs: High-HB versus T18 (upper

row of the figure) and Min-HB versus GC-HB (lower row of the figure). In the High-HB versus T18 comparison, the N_{H_2} histogram of the NGC 253 CMZ has a shallower declining slope from the peak at $\sim 10^{21.5} \text{ cm}^{-2}(\text{km s}^{-1})^{-1}$ to the high N_{H_2} end at $\sim 10^{23} \text{ cm}^{-2}(\text{km s}^{-1})^{-1}$. A similar trend is identified in the n_{H_2} histograms. The n_{H_2} frequency of NGC 253 has a wider distribution toward high n_{H_2} values up to 10^6 cm^{-3} , whereas that of the GC declines more steeply and vanishes at $n_{\text{H}_2} \sim 10^5 \text{ cm}^{-3}$. We fit the n_{H_2} histograms from the High-HB and T18 analyses with a log-normal function, $f(n_{\text{H}_2}) \propto \exp[-(\log_{10} n_{\text{H}_2}/\text{cm}^{-3} - \bar{n})^2/(2\Delta_n^2)]$, for $n_{\text{H}_2} \geq 10^4 \text{ cm}^{-3}$ and show the results in Figure 17. The scaling parameter Δ_n is a factor of ~ 2.5 larger for the High-HB histogram than for the T18 histogram, although the two have a similar mean of $10^{4.1\text{--}4.2} \text{ cm}^{-3}$. The Min-HB versus GC-HB comparison leads to the same conclusion; both N_{H_2} and n_{H_2} distributions show broader extensions toward high values for NGC 253 than the GC. Though the n_{H_2} distributions in the Min-HB and GC-HB results are systematically shifted from the High-HB and T18 histograms by ~ -0.4 dex, respectively, it does not affect their relative difference. The presence of broader high- N_{H_2} and high- n_{H_2} tails in NGC 253 is noteworthy because the approximately order-of-magnitude lower linear resolution for NGC 253 limits the sensitivity to high- N_{H_2} / n_{H_2} peaks due to stronger beam smearing. The actual difference between the NGC 253 CMZ and the GC could be larger than detected when compared at the same spatial scales.

On the other hand, the T_{kin} histogram of the GC shows higher frequencies for $T_{\text{kin}} \gtrsim 10^{2.2} \text{ K}$ than the NGC 253 histogram in both the High-HB versus T18 and Min-HB versus GC-HB comparisons. This lower frequency of high- T_{kin} spaxels in the NGC 253 CMZ is consistent with the heavier beam smearing for the NGC 253 CMZ, and therefore it is unclear whether they differ significantly in T_{kin} when compared on the same size scale. The lack of obvious T_{kin} enhancement in NGC 253 may indicate the enormous difference between NGC 253 and the GC in SFR does not significantly affect the heating budget of the high-density component.

5.2.5. Modified Dense-gas Mass Fraction and SF Threshold Density

The difference between the n_{H_2} histograms of the NGC 253 and the GC seen in Section 5.2.4 could be translated into the difference in the dense-gas mass fractions with varying thresholds of the definition of “dense gas.” We show the inverse cumulative form of the n_{H_2} histograms in Figure 18. Note that this inverse cumulative function represents the dense-gas mass fraction with varying threshold n_{H_2} (except for the contribution from the low-density component), which we define as the modified dense-gas mass fraction $f_{\text{DG}}^*(n)$; i.e.,

$$f_{\text{DG}}^*(n) \equiv \frac{\sum_{n_{\text{H}_2,i} > n} \langle N_{\text{H}_2} \rangle_{\text{beam},i}}{\sum \langle N_{\text{H}_2} \rangle_{\text{beam},i}}, \quad (4)$$

where subscript i indexes the spaxels in the high-density component. In the $f_{\text{DG}}^*(n)$ plot with the High-HB and T18 results (panel (a)), the NGC 253 and the GC show a similar $f_{\text{DG}}^*(n)$ profile in $n_{\text{H}_2} \lesssim 10^{4.5} \text{ cm}^{-3}$. However, $f_{\text{DG}}^*(n)$ in the GC shows a steep decline in $\gtrsim 10^{4.5} \text{ cm}^{-3}$, reaching zero at $n_{\text{H}_2} \sim 10^5 \text{ cm}^{-3}$, while the NGC 253 CMZ plot maintains an approximately constant shallow slope in the range of $n_{\text{H}_2} = 10^{4.5\text{--}6.0} \text{ cm}^{-3}$. The $f_{\text{DG}}^*(n)$ ratio between the GC to

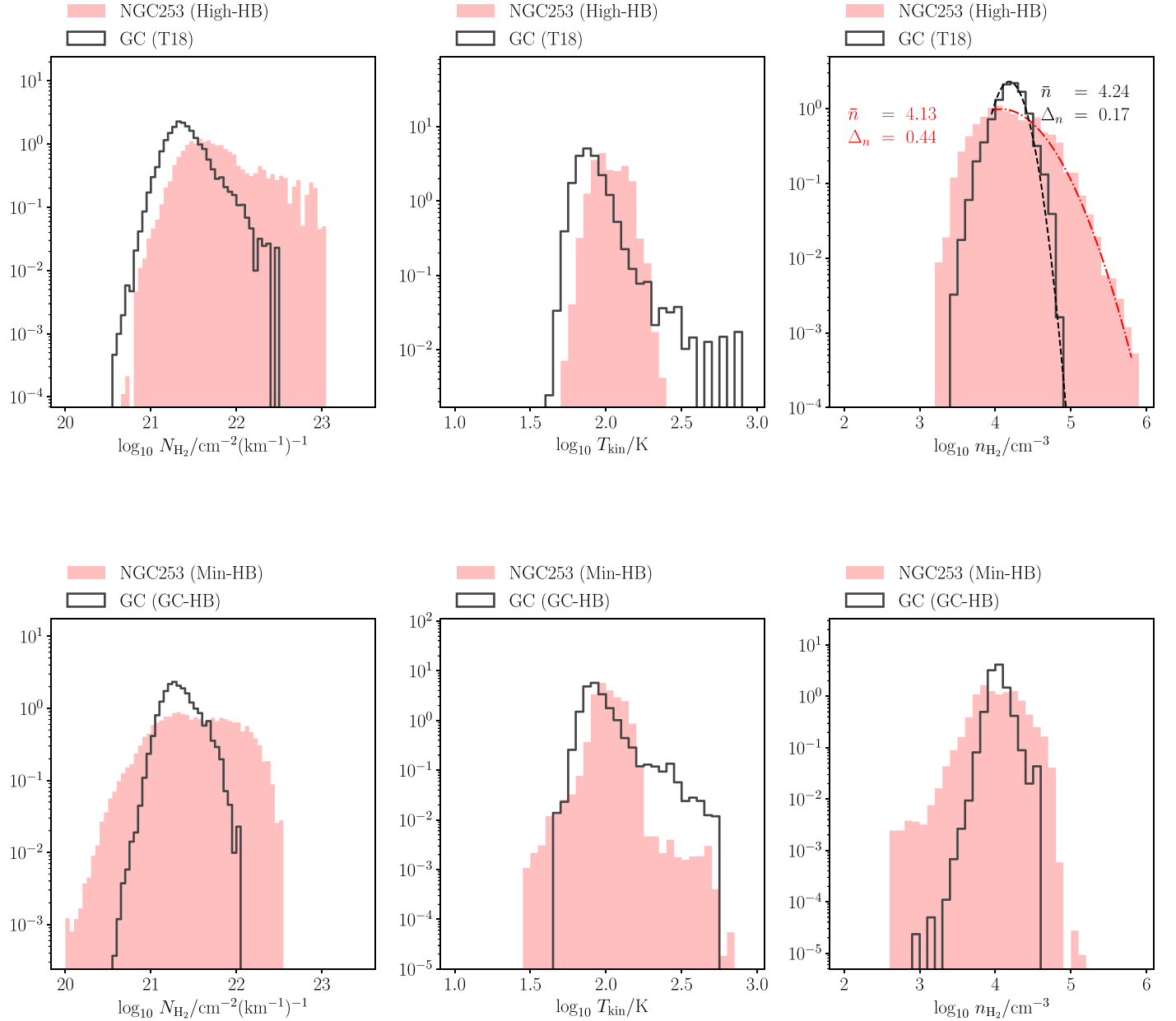


Figure 17. Frequency histograms of N_{H_2} , T_{kin} , and n_{H_2} for NGC 253 (red hatched) and the GC (open). All frequencies are weighted by $\langle N_{\text{H}_2} \rangle_{\text{beam}}$ and normalized so that the integral is unity. The upper row uses the High-HB and T18 results for NGC 253 and the GC, respectively, and the lower uses the Min-HB and GC-HB results. The results of log-normal fitting are shown for the n_{H_2} histograms of the High-HB and T18 results.

the NGC 253 CMZ reaches 0.1, i.e., the same as their SFE_{DG} ratio, at $n_{\text{H}_2} = 10^{4.6} \text{ cm}^{-3}$. Comparison using the Min-HB and GC-HB results (panel (b)) leads to a similar result, except for the threshold n_{H_2} at which the $f_{\text{DG}}^*(n)$ ratio reaches 0.1 lies within the range of $10^{4.3-4.5} \text{ cm}^{-3}$. Hence, if there exists a threshold n_{H_2} that defines the dense gas consumed for SF, it is likely in $\sim 10^{4.3-4.6} \text{ cm}^{-3}$. The rich abundance of the gas exceeding this threshold n_{H_2} in the NGC 253 CMZ, or its scarcity in the GC, could be the critical difference characterizing the centers of the two galaxies.

We caution that the above analysis compares results that differ in spatial resolution by an order of magnitude. Figure 18 also shows the $f_{\text{DG}}^*(n)$ plots where the GC results are smoothed to the working resolution for the NGC 253 CMZ,

i.e., 27 pc and 20 km s^{-1} in the space and velocity. The drop of the resolution-matched $f_{\text{DG}}^*(n)$ in the GC data both for the T18 and GC-HB results (panels (c) and (d), respectively) are steeper than in the nonsmoothed data. The threshold n_{H_2} is estimated to be $\sim 10^{4.4} \text{ cm}^{-3}$ from the High-HB versus T18 comparison, and $\sim 10^{4.2} \text{ cm}^{-3}$ from the Min-HB versus GC-HB comparison. They are $\sim 0.2-0.3$ dex lower than the values without resolution matching, demonstrating that the n_{H_2} estimate is sensitive to the working resolution of the analysis. Conversely, the $f_{\text{DG}}^*(n)$ plot for the NGC 253 CMZ is expected to become shallower if measured at the resolution of the T18, i.e., 2.4 pc and 10 km s^{-1} in the space and velocity, which would yield a higher threshold n_{H_2} than that without resolution matching. By taking this resolution dependence into account, we conservatively conclude that the threshold density is $\sim 10^{4.2-4.6} \text{ cm}^{-3}$.

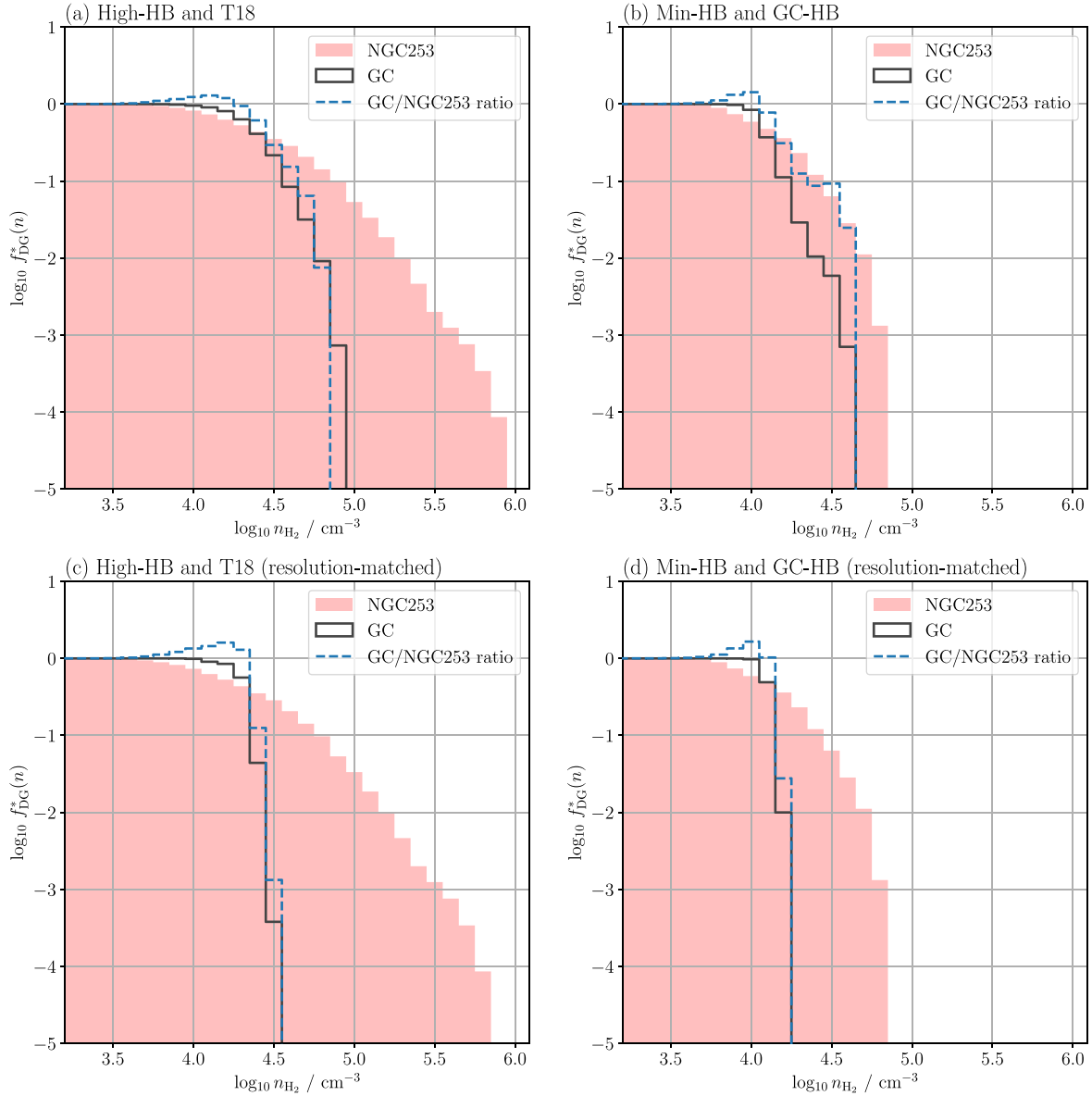


Figure 18. (a) Inverse cumulative histograms of n_{H_2} for NGC 253 (red hatched) and the GC (black solid) using the High-HB and T18 results, respectively. The dashed line shows the frequency ratio of the GC to NGC 253. (b) same as a, but using the T18 results smoothed to the same P - P - V resolution as the High-HB result. (c) Same as (a), but using the Min-HB and GC-HB result. (d) Same as (c), but using the GC-HB results smoothed to the same P - P - V resolution as the Min-HB result.

5.3. Origin of the Contrasting SF Activities in the NGC 253 CMZ and the GC

The above comparison of $f_{\text{DG}}^*(n)$ between the NGC 253 CMZ and the GC (Section 5.2.5) suggests that the n_{H_2} defining the dense gas consumed for SF be 0.4–0.8 dex higher than the boundary separating the low- and high-density components that are traced by low- J CO and HCN transitions. This is consistent with the actual distribution of embedded SF in the NGC 253 CMZ and the GC. Figure 19 shows N_{H_2} - n_{H_2} scatter plots for the high-density component of NGC 253 using the High-HB result, where the spaxels associated with H40 α features (Mills et al. 2021) are colored red. Figure 19 shows that the H40 α features appear exclusively in $n_{\text{H}_2} \gtrsim 10^{4.5} \text{ cm}^{-3}$ regions, which is approximately consistent with the above threshold n_{H_2} obtained from the $f_{\text{DG}}^*(n)$ plots of the High-HB and T18 results. A similar result was obtained for the GC; Tanaka et al. (2020) found that SF signatures (extended green objects, SF masers,

and compact infrared sources) are primarily associated with dens-gas clumps with low virial parameter of <6 , whose typical density is $n_{\text{H}_2} > 10^{4.6} \text{ cm}^{-3}$. This comparison may not be a rigorous one, as we apply different SF tracers and different spatial and velocity resolutions for NGC 253 and the GC, and hence it does not necessarily indicate the presence of a common threshold n_{H_2} of $10^{4.5-4.6} \text{ cm}^{-3}$ in the centers of the two galaxies. Nonetheless, the above results show that embedded star-forming regions are not uniformly distributed throughout the entire high-density components. Instead, they are confined to the highest-density portion of the high-density component, which qualitatively corroborates our findings.

We note that it is not obvious that we can assume a common threshold n_{H_2} for the centers of the two galaxies with different physical environments. The turbulent cloud model predicts that the critical n_{H_2} to initiate gravitational collapse is not universal but depends on the degree of turbulence and magnetic field

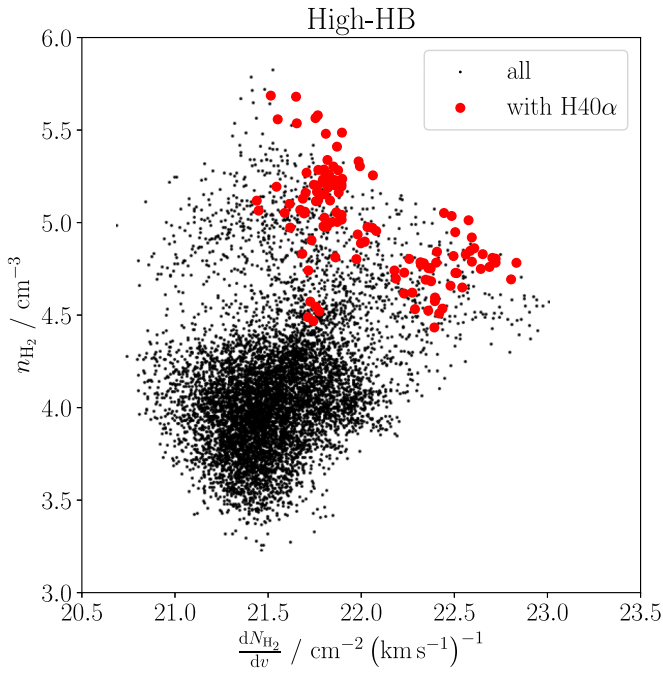


Figure 19. Scatter plot of n_{H_2} vs. dN_{H_2}/dv from the High-HB results. The spaxels associated with compact H40 α emission features (Mills et al. 2021) are colored red.

strength (Krumholz & McKee 2005; Padoan & Nordlund 2011). Krieger et al. (2020) showed that the degree of turbulence measured by velocity dispersion and virial parameter in NGC 253 is similar to those in the GC when compared with high- N_{H_2} regions ($N_{\text{H}_2} \gtrsim 10^{22} \text{ cm}^{-3}$), where SF takes place. However, the magnetic field strength in the literature is slightly higher for the NGC 253 CMZ ($160 \pm 20 \mu\text{G}$; Heesen et al. 2011) than the GC ($\geq 50 \mu\text{G}$; Crocker et al. 2010), potentially resulting in an elevated critical n_{H_2} in the NGC 253 CMZ. In addition, the CR ionization rates reported for the dense clouds in the NGC 253 CMZ, $\sim 10^{-14} \sim 10^{-12} \text{ s}^{-1}$ (Harada et al. 2021; Holdship et al. 2021, 2022; Behrens et al. 2022), tend to be higher than those reported for the GC, $10^{-16} \sim 10^{-14} \text{ s}^{-1}$ (Oka et al. 2005, 2019; Willis et al. 2020), also suggesting a more hostile SF environment in the NGC 253 CMZ. Therefore, it is not evident whether our results indicate a common SF threshold n_{H_2} of $\sim 10^{4.2-4.6} \text{ cm}^{-3}$ in the NGC 253 CMZ and the GC. Nevertheless, we could safely consider that the higher $f_{\text{DG}}^*(n)$ in n_{H_2} above this density range in the NGC 253 CMZ plays a critical role in overcoming the disadvantageous conditions and promoting starburst. We emphasize that this difference in the $f_{\text{DG}}^*(n)$ profile between the NGC 253 CMZ and the GC was not measurable from analysis of the luminosities without spatial information, and it provides a new clue to understanding the low $\text{SFE}_{\text{dense}}$ in the GC, and more generally, the origins of the dispersion in the SFR/HCN ratio among galaxies (Usero et al. 2015; Bigiel et al. 2016; Neumann et al. 2023).

The origin of the broad $f_{\text{DG}}^*(n)$ profile in the NGC 253 CMZ could be caused by the higher turbulent pressure within the GMCs. Krieger et al. 2020 show the velocity dispersion σ_v within the NGC 253 CMZ clouds is by a factor of 2–3 larger than that within the GC clouds over a wide range of spatial scale from 1 to 100 pc except for the highest N_{H_2} region. The turbulent cloud model predicts that such an elevated degree of turbulence broadens the PDF of n_{H_2} (Krumholz & McKee 2005;

Neumann et al. 2023) as we observed in the NGC 253 CMZ. However, the turbulent cloud model also predicts that this broadening of the n_{H_2} PDF is counteracted by an increase in the critical n_{H_2} for gravitational instability, resulting in a net decrease in SFE . The high $\text{SFE}_{\text{dense}}$ in the NGC 253 CMZ contradicts this model prediction and the actually observed anticorrelation between σ_v and the SFR/HCN ratio among galaxies (e.g., Neumann et al. 2023). Alternatively, we may attribute the different $f_{\text{DG}}^*(n)$ in the NGC 253 CMZ and the GC to their different SF phases (Callanan et al. 2021). In this line of theory, the GC could be considered to have undergone a past active phase suggested by several observations (e.g., Tanaka et al. 2007; Yusef-Zadeh et al. 2009), during which dense gas has been depleted. Meanwhile, observations suggest that the formation of new star-forming dense clouds is hindered by frequent destructive cloud–cloud collisions (Tanaka et al. 2018; Enokiya et al. 2021). The depletion of dense gas in the present-day GC could be attributed to a combination of these two effects.

6. Summary and Conclusions

We have performed a spatially resolved excitation analysis of the CMZ of the starburst galaxy NGC 253 by exploiting the rich data set of the ALCHEMI line survey. On the basis of the comparison with the similar analysis performed for the quiescent CMZ of the Milky Way, we attempted to find the difference in the physical condition parameters of the molecular clouds that distinguish the starburst and quiescent galactic centers. We applied the non-LTE analysis to three different sets of input lines (High-density, Low-density, and Minimal data sets) from the ALCHEMI data by employing two different statistical modeling approaches, namely, the hierarchical Bayesian (HB) and nonhierarchical Bayesian (NHB) models. These modeling processes allowed the derivation of the full P – P – V distributions of the fundamental physical condition parameters, including N_{H_2} , T_{kin} , and n_{H_2} , delineated at spatial and velocity resolutions of 27 pc and 20 km s^{-1} , respectively. The main results are summarized below.

1. The main HB analyses using the Low- and High-density data sets (Low-HB and High-HB analyses) confirmed that the NGC 253 CMZ contains at least two molecular cloud components: the low-density component ($T_{\text{kin}} = 85 \text{ K}$, $n_{\text{H}_2} = 10^{3.3} \text{ cm}^{-3}$) mainly traced by low- J ($J \leq 3$) transitions of CO and its isotopologues, and the high-density component ($T_{\text{kin}} = 110 \text{ K}$, $n_{\text{H}_2} = 10^{4.5} \text{ cm}^{-3}$) traced by low-excitation ($E_u/k_B \lesssim 70 \text{ K}$) transitions of high-density tracer species. The low- and high-density components correspond to the first and second excitation components detected in previous dust SED and CO SLED studies, respectively (Sections 3.1, 5.1.2). The two components are found to be spatially mixed in the 27 pc resolution, exhibiting a strong spaxel-to-spaxel correlation in the N_{H_2} distribution across the entire analyzed region (Section 4.5).
2. The physically unreasonable parameter distributions due to the severe parameter degeneracy in the NHB analysis, such as the anticorrelations in N_{H_2} versus T_{kin} and n_{H_2} versus T_{kin} , were successfully suppressed in the HB analysis for both the Low-density and High-density data sets. The NHB analysis also yielded $N_{\text{H}_2}/n_{\text{H}_2}$ values that were too low to fit the r – σ_v relationship for the NGC 253

- CMZ. Hence, the HB analysis was able to provide more realistic P – P – V distributions of the physical condition parameters than the standard NHB analysis (Section 4.2).
3. Molecular gas with high T_{kin} and n_{H_2} is concentrated in the starburst region within the innermost $\sim 10''$ radius, where typical $(T_{\text{kin}}, n_{\text{H}_2})$ are $(100\text{--}200\text{ K}, 10^{3.0\text{--}3.6}\text{ cm}^{-3})$ and $(100\text{--}150\text{ K}, 10^{4.5\text{--}5.5}\text{ cm}^{-3})$ in the low- and high-density components, respectively (Section 4.3). High-velocity warm gas was found associated with this region at velocities separated from the main velocity component by $\sim \pm 100\text{ km s}^{-1}$, indicating the presence of SF-driven shocks. A few high- T_{kin} and high- n_{H_2} spots were detected outside the central starburst region, which may indicate interaction with shocks of non-SF origins, such as the large-scale molecular outflows and cloud–cloud collisions (Section 4.4).
 4. The fractional abundances of tracers of shocks and high-temperature molecular gas (SiO, HC_3N , and $p\text{--H}_2\text{CO}$) show outwardly increasing distributions from the central $\pm 10''$ region to the outskirts of the CMZ (Section 4.7). This indicates that the low-excitation transitions of these species trace shocks of non-SF origin (Section 5.1.4).
 5. The $^{12}\text{C}/^{13}\text{C}$ isotopic abundance (R_{13}) was fixed at 21 in the Low-HB analysis, based on the $^{12}\text{C}^{18}\text{O}/^{13}\text{C}^{18}\text{O}$ measurement by Martín et al. (2019). However, the High-HB analysis yielded R_{13} ranging from ~ 45 to ~ 60 , which is 2–3 times that of the Low-HB value and the values estimated from the ALCHEMI data by Martín et al. (2021). This difference with the previous results is caused by the one-zone approximation adopted in our analysis, which leads to higher optical depths for the HCN, HCO^+ , and CS transitions than Martín et al. (2021), who performed independent fittings for each species (Section 4.7).
 6. The Low-HB analysis possibly overestimates the correlation coefficient between N_{H_2} and n_{H_2} , due to insufficient resolution of their degeneracy in the excitation analysis (Section 4.8.1). The difference among the physical conditions traced by different molecular species in the High-density data set was confirmed to be insignificant, though HCN lines are somewhat biased to high- T_{kin} and/or high- n_{H_2} regions compared to other species (Section 4.8.4). Other caveats of the Low-HB and High-HB results are summarized in Section 4.8.5.
 7. The n_{H_2} and T_{kin} values from the Low-HB and High-HB results are confirmed to be approximately consistent with the previous measurement in the literature (Section 5.1). The difference from the CO SLED results (R14 and P18) can be reasonably explained by the parameter degeneracy in the CO SLED analyses (Section 5.1.2). The shocked gas of SF origin in the central starburst and a few cold gas features detected in the previous ALCHEMI paper and the NH_3 inversion transition studies are possibly missed in our analysis, due to the selection of the input data set and the one-zone LVG assumption employed in the HB analysis (Sections 5.1.3, 5.1.4).
 8. The masses of the low-density and high-density components were estimated to be $1.6 \times 10^8 M_\odot$ and $0.50 \times 10^8 M_\odot$, respectively. The dense-gas mass fraction (f_{DG}^*) of 0.24 is approximately twice that of the GC with the n_{H_2} separating the high- and low-density components being $\sim 10^{3.5\text{--}3.8}\text{ cm}^{-3}$. Their values depend on the assumed abundances of CO, ^{13}CO , and HNC, but are consistent with previous results from the CO SLED and dust SED analyses (Section 4.5).
 9. The Low-HB result yields the CO-to- H_2 conversion factor for the NGC 253 CMZ is $X(\text{CO})$ to be $0.7 \times 10^{20}\text{ cm}^{-2}/(\text{K km s}^{-1})$ for all of the 1–0, 2–1, and 3–2 transitions. The HCN 1–0-to- H_2 conversion factor for the high-density component is $2 \times 10^{20}\text{ cm}^{-2}/(\text{K km s}^{-1})$. They are consistent with those calculated for the GC, confirming that the dense-gas fraction (f_{DG}) defined as the HCN 1–0/CO 1–0 flux ratio serves as a good measure of f_{DG}^* based on the mass estimate. However, $\gtrsim 70\%$ of the mass of the high-density component is constituted by the spaxels with $n_{\text{H}_2} < 3 \times 10^4\text{ cm}^{-3}$, being consistent with the arguments against the reliability of the HCN 1–0 as an accurate measure of the dense-gas mass consumed for SF (Section 5.2.2).
 10. The star formation efficiency for the high-density component ($\text{SFE}_{\text{DG}} \equiv \text{SFR}/\text{high-density gas mass}$) is approximately 10 times that of the GC. This difference is approximately an order of magnitude larger than their difference in f_{DG}^* , confirming that SFE cannot be solely determined by f_{DG}^* or f_{DG} (Section 5.2.3).
 11. The n_{H_2} frequency histogram of the NGC 253 CMZ derived from the High-HB result exhibits a 2.5 times broader profile toward higher n_{H_2} values than that of the GC using the T18 result, though they have similar mean n_{H_2} of $10^{4.1\text{--}4.2}\text{ cm}^{-3}$ (Section 5.2.4). The modified dense-gas mass fraction $f_{\text{DG}}^*(n)$, which is f_{DG}^* redefined as a function of the threshold n_{H_2} defining the “dense gas,” declines with an approximately constant shallow slope in the range of $n_{\text{H}_2} \sim 10^{4.5\text{--}6.0}\text{ cm}^{-3}$ for the NGC 253 CMZ, whereas that of the GC steeply declines at $n_{\text{H}_2} \gtrsim 10^{4.5}\text{ cm}^{-3}$, reaching 0 at $n_{\text{H}_2} \sim 10^{5.0}\text{ cm}^{-3}$. When aligning the resolution of the GC data to that of the NGC 253 CMZ data, $f_{\text{DG}}^*(n)$ drops more steeply at a lower n_{H_2} of $\sim 10^{4.4}\text{ cm}^{-3}$ (Section 5.2.5).
 12. The above results were confirmed to be qualitatively unchanged when we used the results of the supplementary analysis with the transitions commonly included in the data set of the ALCHEMI and T18 (the Minimal data set) for both the NGC 253 and the GC, where bias from the selection of the tracer lines is absent (Sections 5.2.4, 5.2.5).
 13. The $f_{\text{DG}}^*(n)$ ratio between the GC to the NGC 253 CMZ reaches 0.1, i.e., the same as their SFE_{DG} ratio, at $n_{\text{H}_2} = 10^{4.2\text{--}4.6}\text{ cm}^{-3}$, where the threshold n_{H_2} value depends on the resolution and the selection of the data set (Section 5.2.5). Signatures of massive star formation are associated with regions above this threshold n_{H_2} both in NGC 253 and the GC. It is not evident whether this threshold n_{H_2} immediately translates into the universal n_{H_2} threshold assumed in the scaling relation between the dense-gas mass and SFR. Nevertheless, the rich abundance of dense gas with $n_{\text{H}_2} \gtrsim 10^{4.2\text{--}4.6}\text{ cm}^{-3}$ in the NGC 253 CMZ is likely to play a critical role in promoting starburst (Section 5.3).
 14. The origin of the broader profile of $f_{\text{DG}}^*(n)$ in the NGC 253 than the GC is potentially linked to the higher degree of turbulence in the former. However, the elevated $\text{SFE}_{\text{dense}}$ in the NGC 253 CMZ contradicts the prediction

of the turbulent cloud model. Alternatively, we may speculate that the GC has consumed the dense gas during a past active SF phase, while the formation of new dense clouds is hindered by frequent destructive cloud–cloud collisions, resulting in the depletion of the dense gas (Section 5.3).

Acknowledgments

The authors are grateful to the anonymous referee for valuable comments that helped to improve the quality of this paper.

This paper makes use of the following ALMA data: ADS/JAO.ALMA#2017.1.00161.L.

ALMA is a partnership of ESO (representing its member states), NSF (USA), and NINS (Japan), together with NRC (Canada), MOST and ASIAA (Taiwan), and KASI (Republic of Korea), in cooperation with the Republic of Chile. The Joint ALMA Observatory is operated by ESO, AUI/NRAO and NAOJ.

K.T. was supported by the ALMA Japan Research Grant of NAOJ ALMA Project, NAOJ-ALMA-300. S.V., M.B., K.-Y.H., and J.B. acknowledge support from the European Research Council (ERC) under the European Union’s Horizon 2020 research and innovation program MOPPEX 833460. K.S. acknowledges the support from the Ministry of Science and Technology (MOST) of Taiwan through the grant MOST 111-2112-M-001-039. V.M.R. has received support from the project RYC2020-029387-I funded by MCIN/AEI /10.13039/501100011033. H.K. and T.T. were supported by JSPS KAKENHI grant No. 20H00172 and the NAOJ ALMA Scientific Research grant No. 2020-15A. L.C. acknowledges financial support through the Spanish grant PID2019-105552RB-C41 funded by MCIN/AEI/10.13039/501100011033.

Facility: ALMA.

Appendix A

Probability Functions in the HB Analysis

The likelihood function $\Pr(\mathcal{V}|\mathcal{P}, \mathcal{E})$ is

$$\Pr(\mathcal{V}|\mathcal{P}, \mathcal{E}) = \prod_{i,k} \exp \left[-\frac{1}{2} \left(\frac{\epsilon_{ik} \cdot F_k(\mathbf{p}_i) - v_{ik}}{\delta_k} \right)^2 \right], \quad (\text{A1})$$

where $F_k(\mathbf{p})$ is the model intensity/ratio of the k th line calculated using the parameter \mathbf{p} and δ_k is the rms noise level of the k th line intensity/ratio. Equation (A1) implicitly assumes that v_{ik} includes additive uncertainty of $\sim \mathcal{N}(0, \delta_k^2)$ and δ_k is uniform across all spaxels.

The prior function $\Pr(\mathcal{P}, \mathcal{E}|\theta)$ gives *a priori* PDF of \mathcal{P} and \mathcal{E} , which is parameterized by $\theta = \{\boldsymbol{\mu}, \Sigma, \boldsymbol{\sigma}\}$;

$$\Pr(\mathcal{P}, \mathcal{E}|\theta) = \prod_i \Pr(\mathbf{p}_i|\boldsymbol{\mu}, \Sigma) \Pr(\epsilon_i|\boldsymbol{\sigma}). \quad (\text{A2})$$

We adopt the following truncated multivariate student prior and log-normal prior for \mathcal{P} and \mathcal{E} , respectively;

$$\Pr(\mathbf{p}_i|\boldsymbol{\mu}, \Sigma) = T_\nu(\mathbf{p}_i|\boldsymbol{\mu}, \Sigma) R(\mathbf{p}_i), \quad (\text{A3})$$

$$\Pr(\epsilon_i|\boldsymbol{\sigma}) = \prod_k L(\epsilon_{ik}|0, \sigma_k^2) \cdot R(\epsilon_i). \quad (\text{A4})$$

where $T_\nu(\cdot|\boldsymbol{\mu}, \Sigma)$ denotes the multivariate student function with shape parameter ν , location vector $\boldsymbol{\mu}$, and scale matrix Σ , and

$L(\cdot|0, \sigma^2)$ the log-normal function with location 0 and dispersion σ^2 . We fix ν at 2 in the present analysis. The function $R(\cdot)$ is a product of logistic functions for individual elements of the parameters, adopted to prevent them from diverging to extremely large or small values. The details of the logistic priors are provided in Appendix C.

The hyperprior function $\Pr(\theta)$ gives the prior probability of θ . We employ mainly noninformative functions for the hyperprior and additional functions to limit the variable ranges of a few specific elements of θ ;

$$\Pr(\theta) = F_{ss}(S, R) \cdot R(\theta), \quad (\text{A5})$$

where $F_{ss}(S, R)$ is the separate-strategy prior (Barnard et al. 2000), which gives a uniform PDF for a symmetric nonnegative definite matrix. Matrices S and R are the scaling diagonal matrix and correlation matrix obtained from the decomposition $\Sigma = SRS$, respectively, i.e., $R_{ij} = \Sigma_{ij}/\sqrt{\Sigma_{ii}\Sigma_{jj}}$ and $S_{ij} = \delta_{ij}\sqrt{\Sigma_{ii}}$, with δ_{ij} being the Kronecker delta. The function $R(\theta)$ represents the logistic hyperpriors introduced to explicitly forbid possible artificial correlations among the parameters.

Function $R(\cdot)$ in Equations (A3), (A4), and (A5) is a product of logistic functions. Let x be an element of \mathcal{P} , \mathcal{E} , or θ , and the upper and lower limits can be set by logistic PDFs,

$$R_{x,\text{upper}}(x) = \left[1 + \exp \left(\frac{x - x_{\text{max}}}{k} \right) \right]^{-1} \quad (\text{A6})$$

and

$$R_{x,\text{lower}}(x) = \left[1 + \exp \left(-\frac{x - x_{\text{min}}}{k} \right) \right]^{-1}, \quad (\text{A7})$$

respectively, where the scale parameter $k > 0$ is taken to be sufficiently small. We use these logistic (hyper-)prior functions to limit the variable ranges of the (hyper-)parameters to physically reasonable values or to prevent the prior functions (Equations (A3) and (A4)) from being too steep. Details of the range limits of the (hyper-)parameters are given in Appendix C.

Appendix B

Probability Functions in the Nonhierarchical Analysis

The NHB analysis uses the same log-normal and logistic priors as the HB analysis for \mathcal{E} and \mathcal{P} , respectively;

$$\Pr(\mathcal{P}, \mathcal{E}) = \prod_{i,k} L(\epsilon_{ik}|0, \sigma_c^2) \cdot \prod_i R(\mathbf{p}_i). \quad (\text{B1})$$

The difference from the hierarchical prior (Equation (A2)) is that $\Pr(\mathcal{P}, \mathcal{E})$ is not parameterized by variable hyperparameters. We fix $\sigma_c = 0.1$ for all i, j , i.e., assume relative uncertainties of $\sim 1 \pm \sigma_c$ for all line intensities. The variable ranges of \mathcal{P} are chosen to be sufficiently wide to cover reasonable parameter values observed in molecular clouds, within which we obtain the marginal posterior function for \mathcal{P} as

$$\begin{aligned} \Pr(\mathcal{P}|\mathcal{V}) &= \int d\mathcal{E} \cdot \Pr(\mathcal{P}, \mathcal{E}|\mathcal{V}) \\ &\sim \int d\mathcal{E} \cdot \Pr(\mathcal{V}|\mathcal{P}, \mathcal{E}) \prod_{i,k} L(\epsilon_{ik}|0, \sigma_c^2), \end{aligned} \quad (\text{B2})$$

which is identical to the likelihood function where input line intensities have relative uncertainties. Hence, the NHB analysis is equivalent to the standard maximum-likelihood analysis with finite parameter ranges.

Appendix C Range Limits

We impose limitations to the variable ranges of several (hyper-) parameters using the logistic (hyper-)priors (Equations (A6) and (A7)). Table 7 shows the upper/lower-limit values applied in the present analysis. The limits to the \mathbf{p} vector are introduced to prevent the parameters from diverging to physically unrealistic values in usual molecular clouds. These limits are of significant importance in the NHB analysis but have almost no effect on the hierarchical analysis, in which the variable ranges of \mathbf{p} are controlled by the prior and hyperprior functions.

The limits of the off-diagonal elements of the R matrix are interpreted as the prior correlation coefficients among the parameters. We introduced the limits to R for two purposes. One is to forbid artificial anticorrelations between ϕ and N_{H_2} , n_{H_2} and N_{H_2} , and n_{H_2} and T_{kin} . These parameters are strongly degenerate in the excitation equations, and the NHB analysis tends to create anticorrelations among them. We limit the R elements for these parameter pairs to be nonnegative. The assumption of nonnegative ϕ - N_{H_2} and n_{H_2} - N_{H_2} correlations is physically reasonable, as it is likely that high- N_{H_2} clouds consist of high- n_{H_2} and are in crowded regions rather than regions isolated from the extended molecular gas. The nonnegative n_{H_2} - T_{kin} correlation may not be obvious, but we adopted this assumption based on the results of the GC. The comparison between the results by Nagai et al. (2007) and T18 has shown that both T_{kin} and n_{H_2} in the high-excitation component are higher than in the low-excitation component. T18 has also shown the absence of strong anticorrelation between T_{kin} and n_{H_2} on 2 pc scales. However, this does not necessarily indicate that the same applies to the low-excitation component of the CMZ of NGC 253. It should be noted that this range-limiting hyperprior might

Table 7
Range Limits of Parameters and Hyperparameters

		Minimum	Maximum
(parameter ^a)	dN_{H_2}/dv	19	23
	T_{kin}	1	3
	n_{H_2}	1	7
	$x_{\text{mol}}(\text{X})$	-10	-5
	R_{13}	1	2
	ϕ	-3	2
(hyperparameter ^b)	$R_{i,j}$	-0.9	0.9
	$R_{N,n}$	0	...
	$R_{N,\phi}$	0	...
	$R_{T,n}$	0	...

Notes.

^a All parameters are in base-10 logarithms.

^b Subscript indices N , n , and T denote elements for N_{H_2} , n_{H_2} , and T_{kin} , respectively.

overcompensate for the correlations that may be present in real molecular clouds.

The other purpose of limiting the variable ranges of the hyperparameters is to prevent the parameters from having too strong (anti)correlation, as a strong (anti)correlation makes the log-student prior of \mathbf{p} extremely narrow, resulting in highly inefficient MCMC even though the hybrid MCMC technique is employed. We limit $|R_{ij}| < 0.9$ for all parameter pairs to prevent the prior function from being too narrow.

Appendix D Integrated Intensity Images

Figure 20 shows the integrated intensity images of the transitions used as the inputs for the analysis. All the images are re-gridded to a $0''.45$ grid spacing and integrated over the v_{LSR} range of $[0\ 500]$ km s^{-1} after filtering of low-S/N spaxels described in Section 3.2,3.3. We refer readers to Section 3 and Martín et al. (2021) for a more detailed data description.

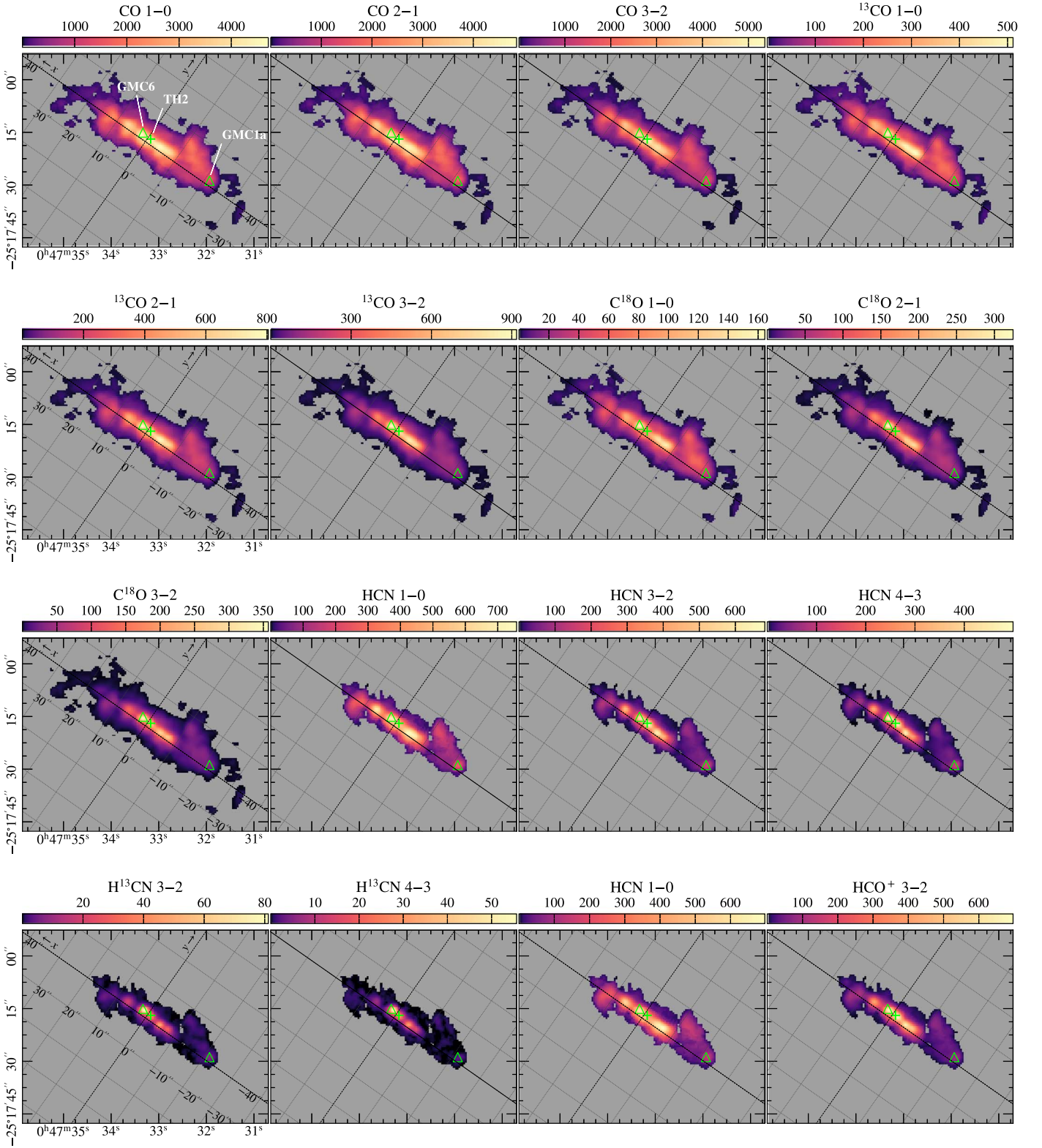


Figure 20. Integrated intensity images of the input transitions in the scale of $\int T_{\text{MB}} dv$ (K km s^{-1}). The major and minor axis coordinates (x - y coordinates) and the positions of TH2, GMC6, and GMC1a are shown for convenience in comparison with Figures 5–7 and 11.

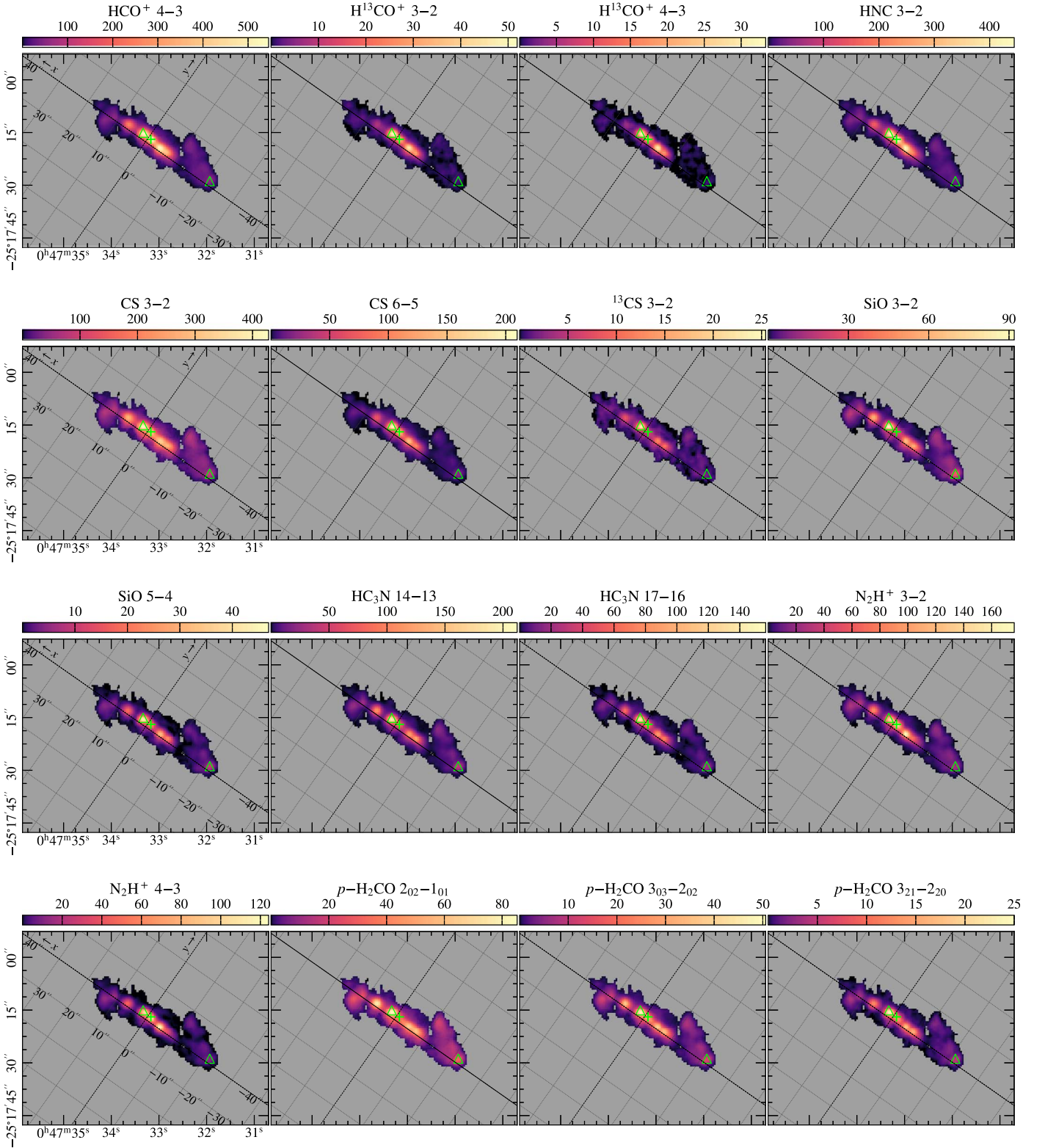


Figure 20. (Continued.)

Appendix E MCMC Results

Figure 21 shows MCMC trace plots of dN_{H_2}/dv , n_{H_2} , T_{kin} , ϕ , and R_{13} at GMC6 for the first 10^4 MCMC steps in the

Low-HB and High-HB runs. Each panel shows two different MCMC runs starting from different initial parameters. In these runs, approximately 10^3 burn-in steps were necessary before convergence; after that, the MCMC reaches convergence with sufficient parameter coverage and density. The

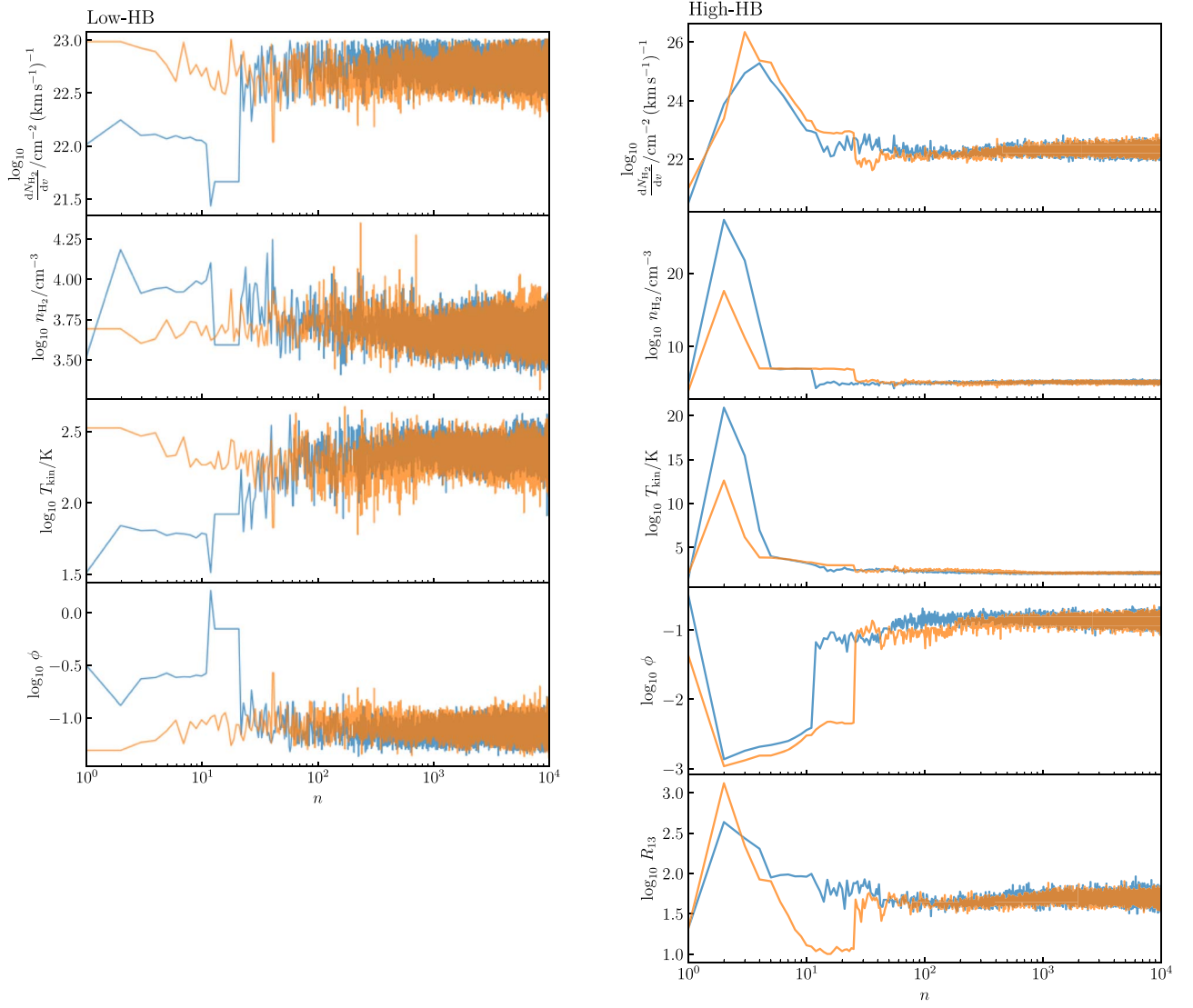


Figure 21. MCMC trace plots of the Low-HB (left) and High-HB (right) runs at GMC6, showing parameter values (dN_{H_2}/dv , n_{H_2} , T_{kin} , ϕ , and R_{13}) against MCMC step number, n , for the first 10^4 steps. Results with two different initial parameters are overlaid on each panel. The Low-HB plot lacks R_{13} , whose value is constant in the analysis.

convergent values are consistent irrespective of the initial parameters. We ran more than a few 10^4 steps after convergence in each run.

Figure 22 shows an example of the marginal posteriors of dN_{H_2}/dv , n_{H_2} , T_{kin} , ϕ , and R_{13} at GMC6 for the Low-HB and High-HB runs.

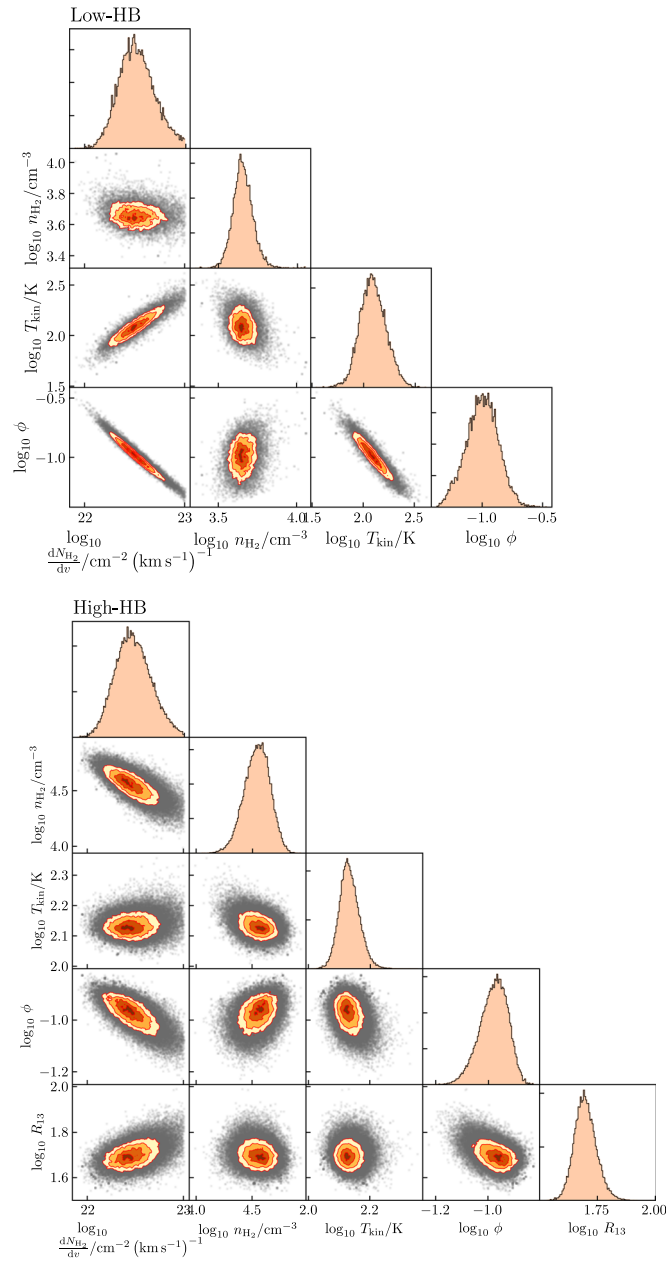


Figure 22. MCMC corner plots of the Low-HB (upper panel) and High-HB (lower panel) runs at GMC6. Each panel shows 1D (diagonal panels) or 2D histograms (off-diagonal panels) of the marginal posterior PDF. The colored contours overlaid on the scatter plots are drawn at 30%, 50%, 80%, and 95% credible intervals.

Appendix F Optical Depths

We performed a pixel-wise calculation of the optical depths of the transitions based on the LVG method, using the parameters from the Low-HB and High-HB analyses. The

calculation was performed for spaxels at which all of the N_{H_2} , T_{kin} , n_{H_2} , R_{13} , and x_{mol} values were determined with uncertainties less than 0.3 dex. Figure 23 shows the spaxel-based frequency distributions of the calculated optical depths.

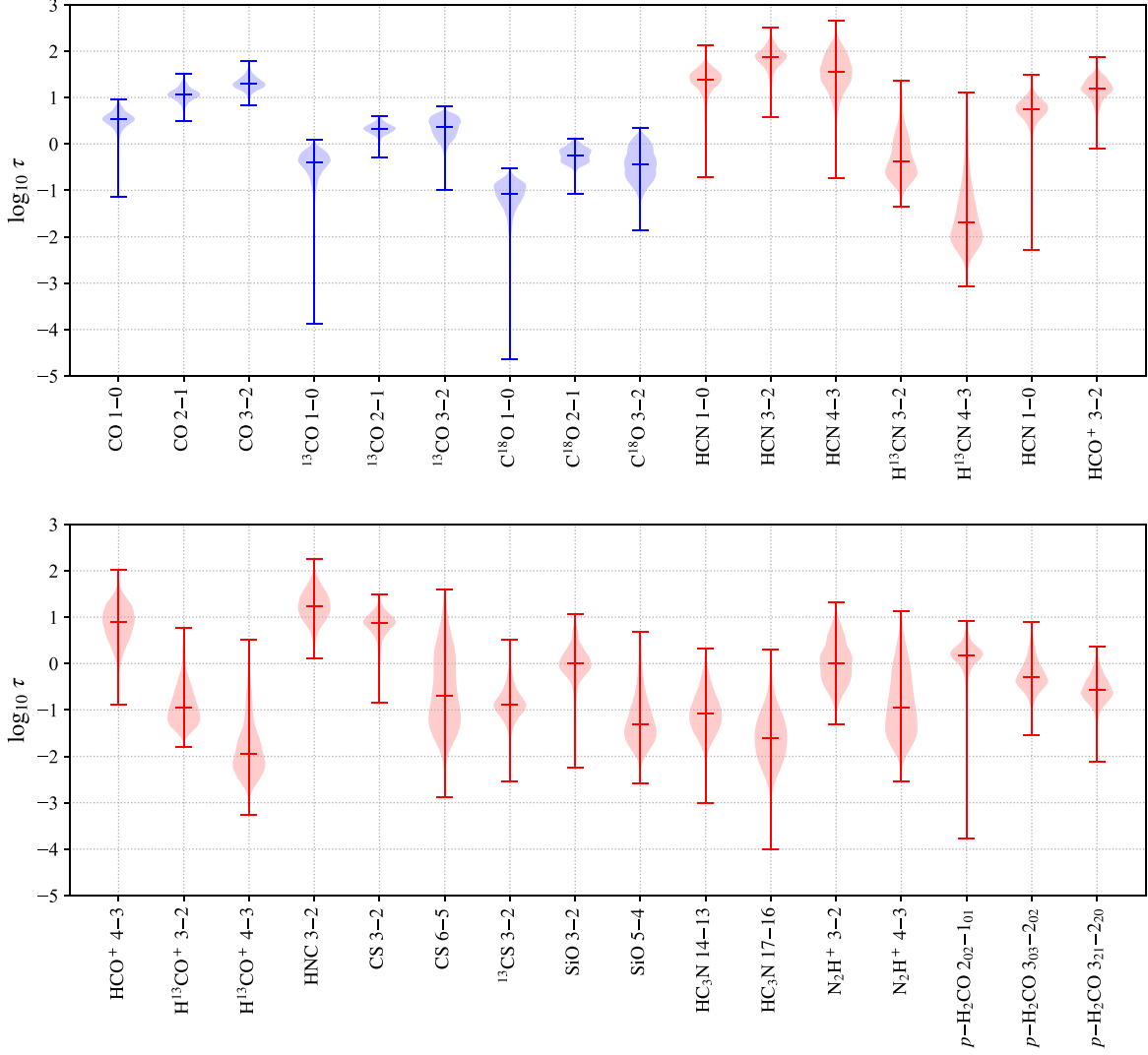


Figure 23. Optical depths evaluated from the parameters obtained from the Low-HB and High-HB analyses. The violin plots show spaxel-based frequency distributions, with bars indicating the frequency minima, medians, and maxima. Transitions in the Low-density and High-density data sets are colored blue and red, respectively.

Appendix G

Results of the Nonhierarchical Analyses and the Hierarchical Analysis for the GC

The P - P and P - P - V distribution of $\langle N_{\text{H}_2} \rangle_{\text{beam}}$, n_{H_2} , and T_{kin} for the Low-NHB, High-NHB, and the GC-HB analyses are shown in Figures 24, 25, and 26, respectively.

Figure 27 shows spaxel-by-spaxel scatter plots of the $\langle N_{\text{H}_2} \rangle_{\text{beam}}$, n_{H_2} , and T_{kin} of the GC-HB results versus the T18 results.

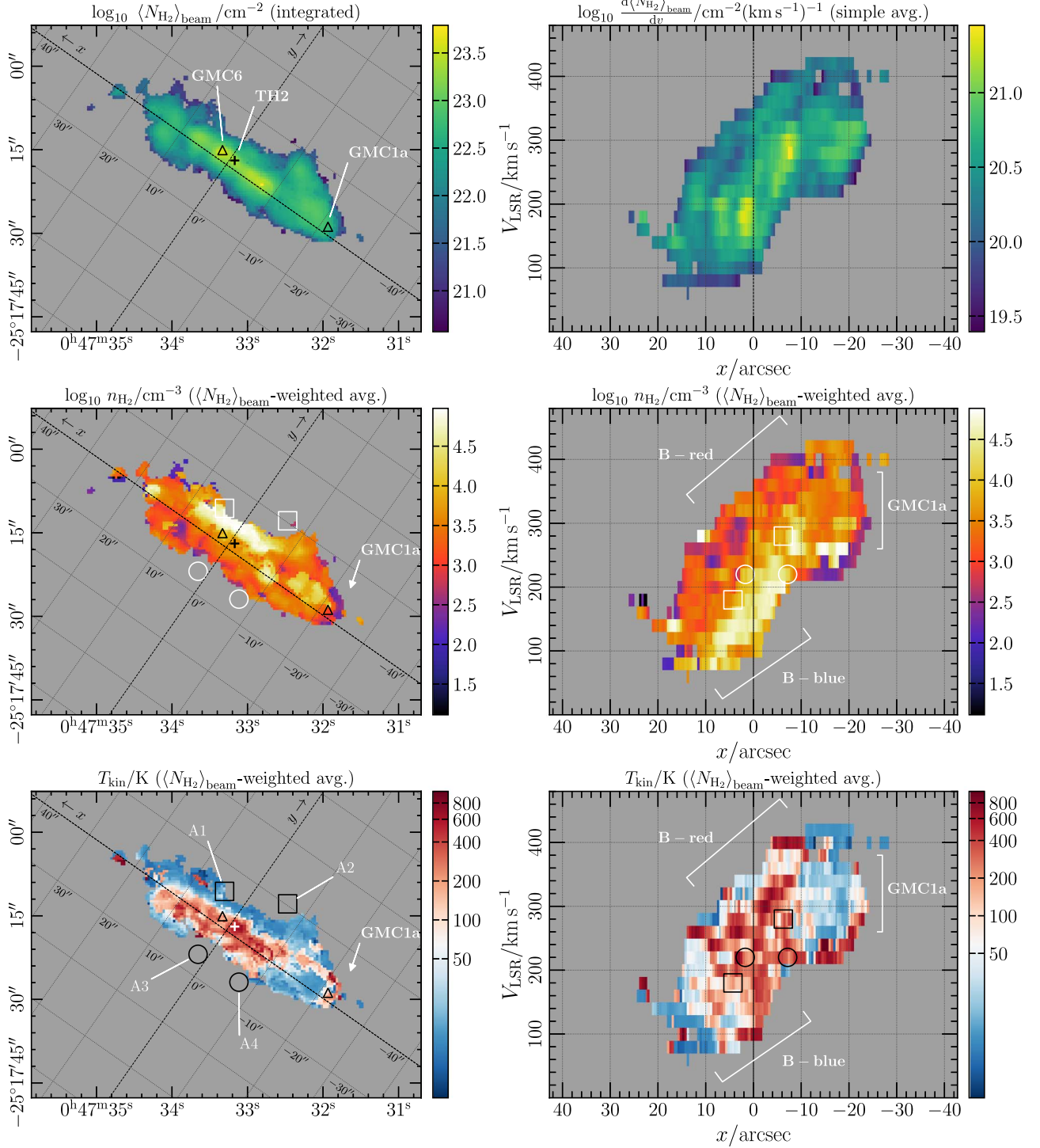
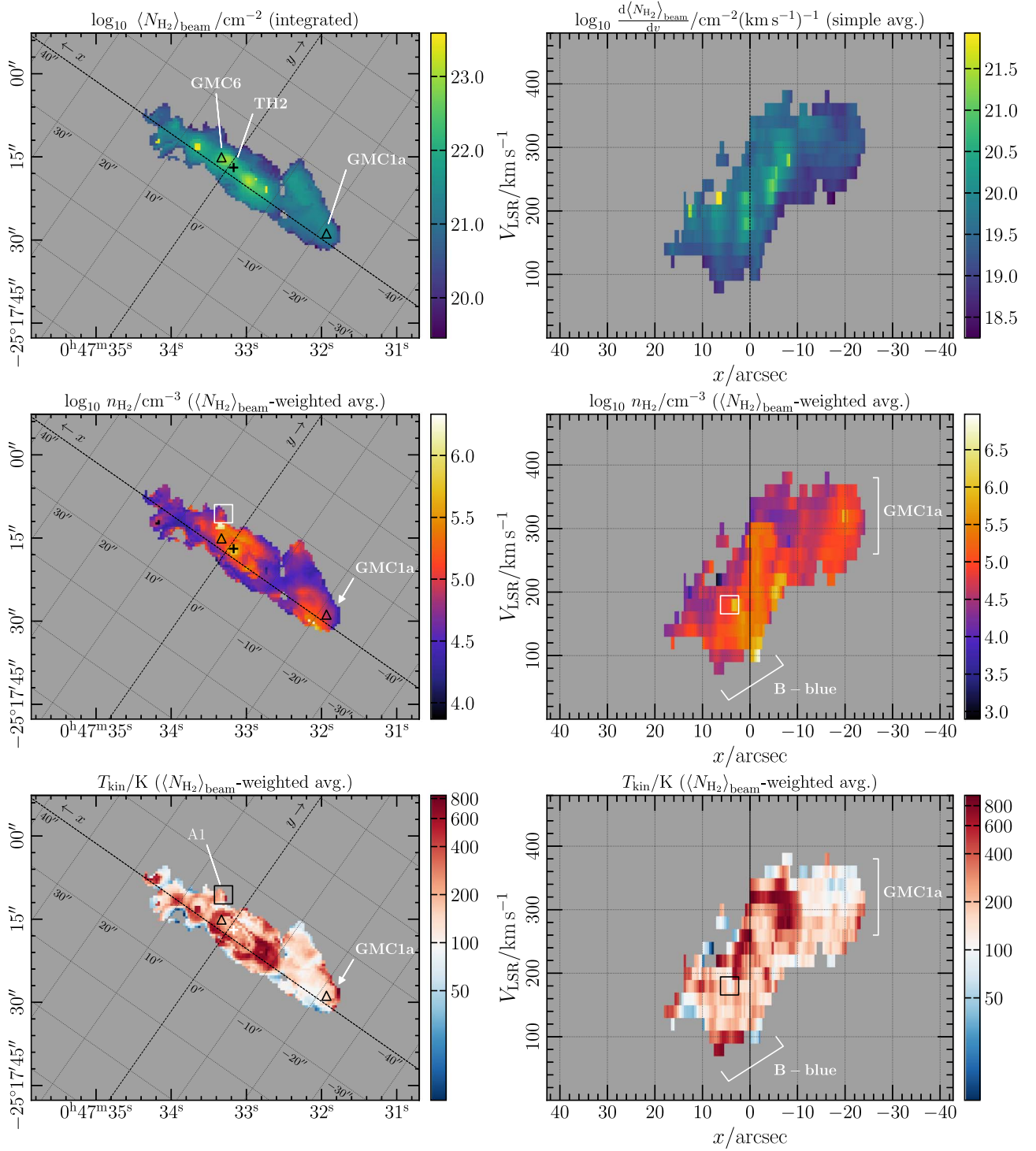


Figure 24. Same as Figure 5, but for the Low-NHB result.

**Figure 25.** Same as Figure 5, but for the High-NHB result.

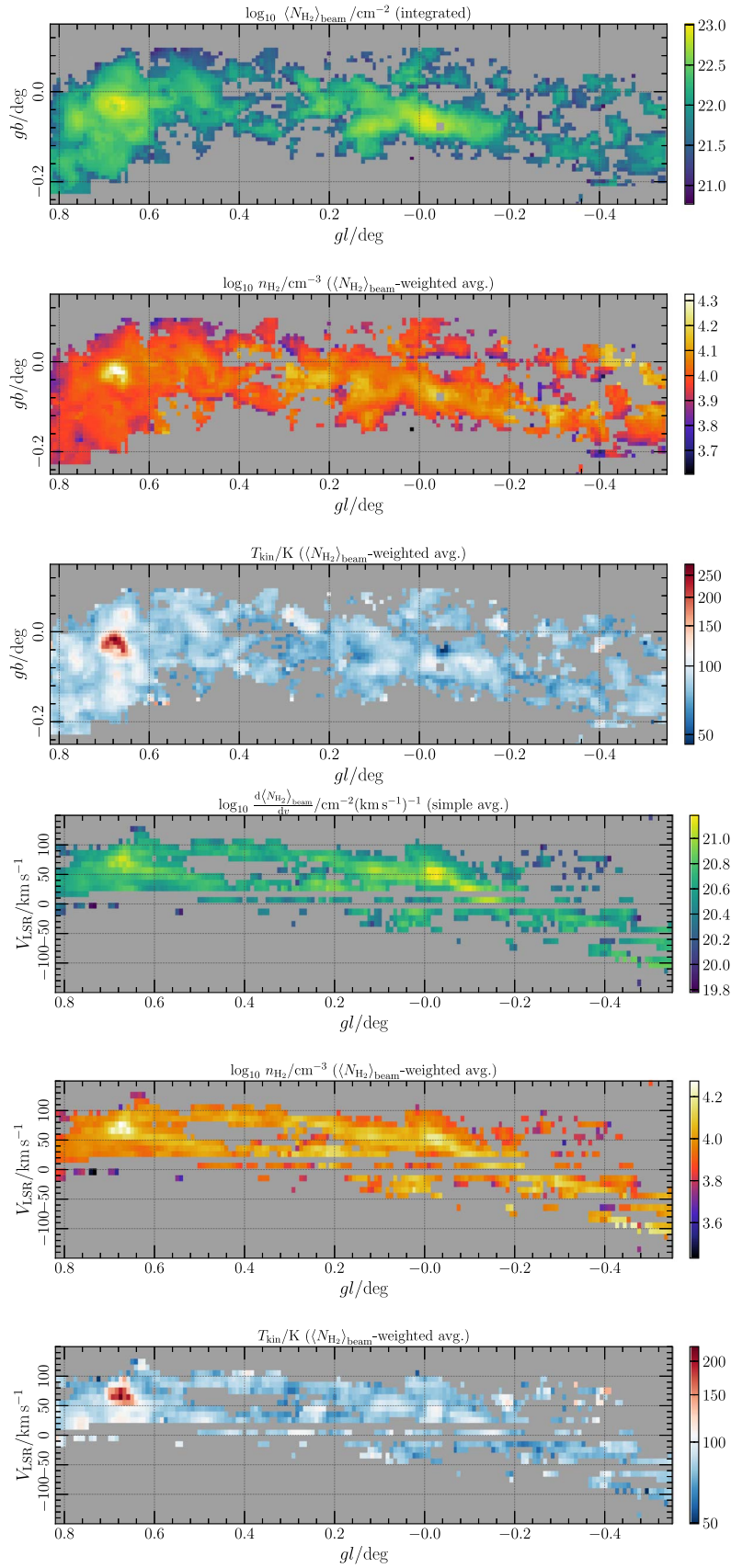


Figure 26. Same as Figure 5, but for the GC-HB result.

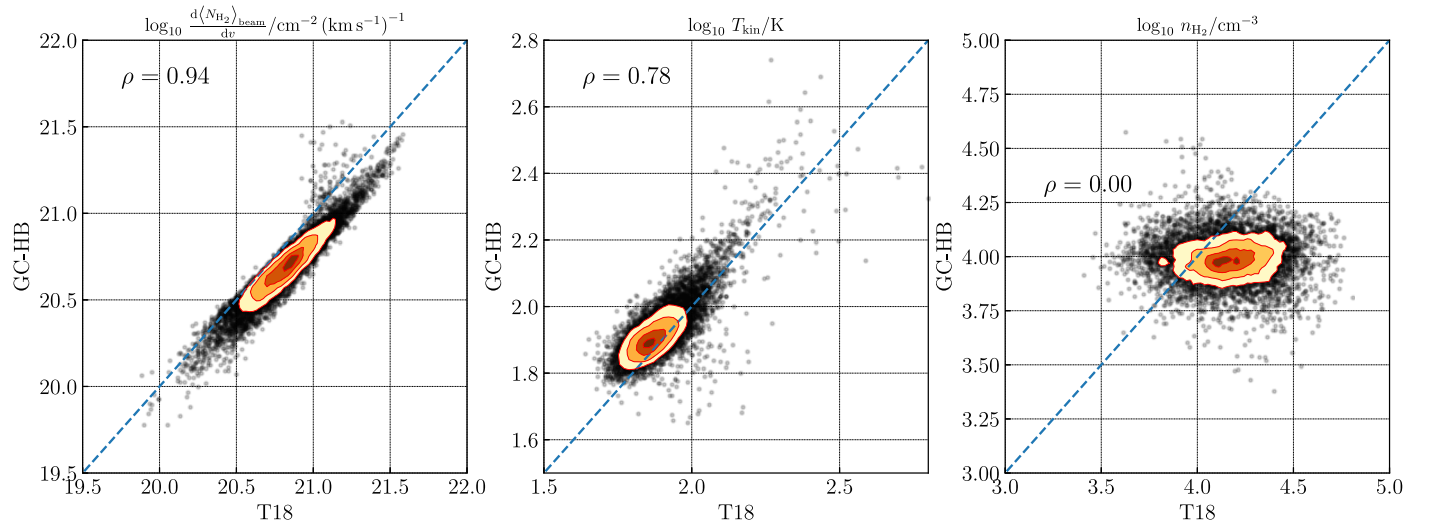


Figure 27. Same as Figure 8 but for the T18 results vs. GC-HB results.

ORCID iDs

Kunihiko Tanaka <https://orcid.org/0000-0001-8153-1986>
 Jeffrey G. Mangum <https://orcid.org/0000-0003-1183-9293>
 Serena Viti <https://orcid.org/0000-0001-8504-8844>
 Sergio Martín <https://orcid.org/0000-0001-9281-2919>
 Nanase Harada <https://orcid.org/0000-0002-6824-6627>
 Kazushi Sakamoto <https://orcid.org/0000-0001-5187-2288>
 Sebastien Muller <https://orcid.org/0000-0002-9931-1313>
 Yuki Yoshimura <https://orcid.org/0000-0002-1413-1963>
 Kouichiro Nakanishi <https://orcid.org/0000-0002-6939-0372>
 Rubén Herrero-Illana <https://orcid.org/0000-0002-7758-8717>
 Kimberly L. Emig <https://orcid.org/0000-0001-6527-6954>
 Hiroyuki Kaneko <https://orcid.org/0000-0002-2699-4862>
 Tomoka Tosaki <https://orcid.org/0000-0001-9016-2641>
 Erica Behrens <https://orcid.org/0000-0002-2333-5474>
 Víctor M. Rivilla <https://orcid.org/0000-0002-2887-5859>
 Laura Colzi <https://orcid.org/0000-0001-8064-6394>
 Yuri Nishimura <https://orcid.org/0000-0003-0563-067X>
 P. K. Humire <https://orcid.org/0000-0003-3537-4849>
 Mathilde Bouvier <https://orcid.org/0000-0003-0167-0746>
 Ko-Yun Huang <https://orcid.org/0000-0002-1227-8435>
 Joshua Butterworth <https://orcid.org/0000-0002-5353-1775>
 David S. Meier <https://orcid.org/0000-0001-9436-9471>
 Paul P. van der Werf <https://orcid.org/0000-0001-5434-5942>

References

- Aalto, S., García-Burillo, S., Muller, S., et al. 2015, *A&A*, **574**, 85
 Ao, Y., Henkel, C., Menten, K. M., et al. 2013, *A&A*, **550**, A135
 Arai, H., Nagai, M., Fujita, S., et al. 2016, *PASJ*, **68**, 2
 Bailin, J., Bell, E. F., Chappell, S. N., Radburn-Smith, D. J., & de Jong, R. S. 2011, *ApJ*, **736**, 24
 Balança, C., Dayou, F., Faure, A., Wiesenfeld, L., & Feautrier, N. 2018, *MNRAS*, **479**, 2692
 Barnard, J., McCulloch, R., & Meng, X.-L. 2000, *Statistica Sinica*, **10**, 1281
 Barnes, A. T., Kauffmann, J., Bigiel, F., et al. 2020, *MNRAS*, **497**, 1972
 Barrientos, A., Holdship, J., Solar, M., et al. 2021, *ExA*, **52**, 157
 Behrens, E., Mangum, J. G., Holdship, J., et al. 2022, *ApJ*, **939**, 119
 Belloche, A., Müller, H., Menten, K. M., Schilke, P., & Comito, C. 2013, *A&A*, **559**, A47
 Bigiel, F., Leroy, A. K., Jiménez-Donaire, M. J., et al. 2016, *ApJL*, **822**, L26
 Bolatto, A. D., Wolfire, M. G., & Leroy, A. K. 2013, *ARA&A*, **51**, 207
 Callanan, D., Longmore, S. N., Kruijssen, J. M., et al. 2021, *MNRAS*, **505**, 4310
 Crocker, R. M., Jones, D. I., Melia, F., Ott, J., & Protheroe, R. J. 2010, *Natur*, **463**, 65
 Dahmen, G., Hüttemeister, S., Wilson, T. L., & Mauersberger, R. 1998, *A&A*, **331**, 959
 Duane, S., Kennedy, A. D., Pendleton, B. J., & Roweth, D. 1987, *PhLB*, **195**, 216
 Dumouchel, F., Faure, A., & Lique, F. 2010, *MNRAS*, **406**, 2488
 Enokiya, R., Torii, K., & Fukui, Y. 2021, *PASJ*, **73**, 75E
 Faure, A., Lique, F., & Wiesenfeld, L. 2016, *MNRAS*, **460**, 2103
 Flower, D. R. 1999, *MNRAS*, **305**, 651
 Gallagher, M. J., Leroy, A. K., Bigiel, F., et al. 2018, *ApJ*, **858**, 90
 Gao, Y., & Solomon, P. M. 2004, *ApJ*, **606**, 271
 Ginsburg, A., Henkel, C., Ao, Y., et al. 2016, *A&A*, **586**, 50
 Goldreich, P., & Kwan, J. 1974, *ApJ*, **190**, 27
 Gorski, M., Ott, J., Rand, R., et al. 2017, *ApJ*, **842**, 124
 Goto, M., Usuda, T., Nagata, T., et al. 2008, *ApJ*, **688**, 306
 Gravity Collaboration, Abuter, R., Amorim, A., et al. 2019, *A&A*, **625**, L10
 Green, S., & Thaddeus, P. 1974, *ApJ*, **191**, 653
 Haasler, D., Rivilla, V. M., Martín, S., et al. 2022, *A&A*, **659**, A158
 Harada, N., Martín, S., Mangum, J. G., et al. 2021, *ApJ*, **923**, 24
 Harada, N., Martín, S., Mangum, J. G., et al. 2022, *ApJ*, **938**, 80
 Heesen, V., Beck, R., Krause, M., & Dettmar, R. J. 2011, *A&A*, **535**, A79
 Henkel, C., Mauersberger, R., Wiklind, T., et al. 1993, *A&A*, **268**, L17
 Holdship, J., Mangum, J. G., Viti, S., et al. 2022, *ApJ*, **931**, 89
 Holdship, J., Viti, S., Martín, S., et al. 2021, *A&A*, **654**, A55
 Huang, K. Y., Viti, S., Holdship, J., et al. 2023, *A&A*, **675**, 151
 Humire, P. K., Henkel, C., Hernández-Gómez, A., et al. 2022, *A&A*, **663**, A33
 Jiménez-Donaire, M. J., Bigiel, F., Leroy, A. K., et al. 2019, *ApJ*, **880**, 127
 Jones, G. H., Clark, P. C., Glover, S. C., & Hacar, A. 2023, *MNRAS*, **520**, 1005
 Jones, P. A., Burton, M. G., Cunningham, M. R., et al. 2012, *MNRAS*, **419**, 2961
 Jorgensen, J. K., Hogerheijde, M. R., van Dishoeck, E. F., Blake, G. A., & Schoier, F. L. 2004, *A&A*, **413**, 993
 Kauffmann, J., Goldsmith, P. F., Melnick, G., et al. 2017, *A&A*, **605**, 5
 Kauffmann, J., Pillai, T., & Goldsmith, P. F. 2013, *ApJ*, **779**, 185
 Kelly, C., Shetty, R., Stutz, A. M., et al. 2012, *ApJ*, **752**, 55
 Krieger, N., Bolatto, A. D., Koch, E. W., et al. 2020, *ApJ*, **899**, 158
 Krieger, N., Ott, J., Beuther, H., et al. 2017, *ApJ*, **850**, 77
 Krumholz, M. R., & McKee, C. F. 2005, *ApJ*, **630**, 250
 Lada, C. J., Forbrich, J., Lombardi, M., & Alves, J. F. 2012, *ApJ*, **745**, 190
 Langer, W. D., & Penzias, A. A. 1990, *ApJ*, **357**, 477
 Langer, W. D., & Penzias, A. A. 1993, *ApJ*, **408**, 539
 Leroy, A. K., Bolatto, A. D., Ostriker, E. C., et al. 2015, *ApJ*, **801**, 25
 Leroy, A. K., Bolatto, A. D., Ostriker, E. C., et al. 2018, *ApJ*, **869**, 126
 Licquia, T. C., & Newman, J. A. 2015, *ApJ*, **806**, 96
 Longmore, S. N., Bally, J., Testi, L., et al. 2013, *MNRAS*, **429**, 987
 Mangum, J., Darling, J., Henkel, C., et al. 2013, *ApJ*, **779**, 33
 Mangum, J., Ginsburg, A. G., Henkel, C., et al. 2019, *ApJ*, **871**, 170
 Marsh, K. A., Whitworth, A. P., Lomax, O., et al. 2017, *MNRAS*, **471**, 2730

- Martín, S., Aladro, R., Martín-Pintado, J., & Mauersberger, R. 2010, *A&A*, **522**, 62
- Martín, S., Mangum, J. G., Harada, N., et al. 2021, *A&A*, **656**, A46
- Martín, S., Muller, S., Henkel, C., et al. 2019, *A&A*, **624**, 125
- Mauersberger, R., Henkel, C., Wielebinski, R., Wiklind, T., & Reuter, H. P. 1996, *A&A*, **305**, 421
- Mills, E. A., Butterfield, N., Ludovici, D. A., et al. 2015, *ApJ*, **805**, 72
- Mills, E. A., Ginsburg, A., Immer, K., et al. 2018, *ApJ*, **868**, 7
- Mills, E. A., Gorski, M., Emig, K. L., et al. 2021, *ApJ*, **919**, 105
- Mills, E. A., Güsten, R., Requena-Torres, M. A., & Morris, M. R. 2013, *ApJ*, **779**, 47
- Nagai, M., Tanaka, K., Kamegai, K., & Oka, T. 2007, *PASJ*, **59**, 25
- Neumann, L., Gallagher, M. J., Bigiel, F., et al. 2023, *MNRAS*, **521**, 3348
- Oka, T., Geballe, T. R., Goto, M., et al. 2019, *ApJ*, **883**, 54
- Oka, T., Geballe, T. R., Goto, M., Usuda, T., & McCall, B. J. 2005, *ApJ*, **632**, 882
- Onus, A., Krumholz, M. R., & Federrath, C. 2018, *MNRAS*, **479**, 1702
- Ott, J., Weiß, A., Henkel, C., & Walter, F. 2005, in AIP Conf. Proc. 783, THE EVOLUTION OF STARBURSTS: The 331st Wilhelm and Else Heraeus Seminar, ed. S. Hüttemeister et al. (Melville, NY: AIP), 141
- Padoan, P., & Nordlund, Å. 2011, *ApJ*, **730**, 40
- Paglionie, T. A. D., Tosaki, T., & Jackson, J. M. 1995, *ApJL*, **454**, 117
- Pérez-Beaupuits, J. P., Güsten, R., Harris, A., et al. 2018, *ApJ*, **860**, 23
- Rathborne, J. M., Longmore, S. N., Jackson, J. M., et al. 2014, *ApJL*, **795**, L25
- Rekola, R., Richer, M. G., McCall, M. L., et al. 2005, *MNRAS*, **361**, 330
- Requena-Torres, M. A., Martín-Pintado, J., Roldán-Franco, N. J., et al. 2006, *A&A*, **455**, 971
- Rico-Villas, F., Martín-Pintado, J., González-Alfonso, E., Martín, S., & Rivilla, V. M. 2020, *MNRAS*, **491**, 4573
- Rosenberg, M. J., Kazandjian, M. V., Van Der Werf, P. P., et al. 2014, *A&A*, **564**, 126
- Sakamoto, K., Aalto, S., Evans, A. S., Wiedner, M. C., & Wilner, D. J. 2010, *ApJL*, **725**, 228
- Sakamoto, K., Mao, R. Q., Matsushita, S., et al. 2011, *ApJ*, **735**, 19
- Schöier, F. L., van der Tak, F. F. S., van Dishoeck, E. F., & Black, J. H. 2005, *A&A*, **432**, 369
- Shetty, R., Beaumont, C. N., Burton, M. G., Kelly, C., & Klessen, R. S. 2012, *MNRAS*, **425**, 720
- Shirley, Y. L. 2015, *PASP*, **127**, 299
- Solomon, P. M., Downes, D., & Radford, S. J. E. 1992, *ApJL*, **398**, L29
- Tafalla, M., Santiago-García, J., Hacar, A., & Bachiller, R. 2010, *A&A*, **522**, A91
- Takano, S., Hofner, P., Winnewisser, G., Nakai, N., & Kawaguchi, K. 2005, *PASJ*, **57**, 549
- Takano, S., Nakai, N., & Kawaguchi, K. 2002, *PASJ*, **54**, 195
- Tanaka, K., Kamegai, K., Nagai, M., & Oka, T. 2007, *PASJ*, **59**, 323
- Tanaka, K., Nagai, M., & Kamegai, K. 2021, *ApJ*, **915**, 79
- Tanaka, K., Nagai, M., Kamegai, K., Iino, T., & Sakai, T. 2018, *ApJS*, **236**, 40
- Tanaka, K., Nagai, M., Kamegai, K., Iino, T., & Sakai, T. 2020, *ApJ*, **903**, 111
- Tang, X. D., Henkel, C., Menten, K. M., et al. 2019, *A&A*, **629**, 6
- Tsuboi, M., Handa, T., & Ukita, N. 1999, *ApJS*, **120**, 1
- Turner, B. E., Chan, K.-W., Green, S., & Lubowich, D. A. 1992, *ApJ*, **399**, 114
- Turner, J. L., & Ho, P. T. P. 1985, *ApJL*, **299**, 77
- Ulvestad, J. A. S. U., & Antonucci, R. O. R. J. A. 1997, *ApJ*, **488**, 621
- Usero, A., Leroy, A. K., Walter, F., et al. 2015, *AJ*, **150**, 115
- Veatch, T. J., Groppi, C. E., & Hedden, A. 2013, *ApJL*, **765**, L34
- Weiß, A., Kovács, A., Güsten, R., et al. 2008, *A&A*, **490**, 77
- Wiesenfeld, L., & Faure, A. 2013, *MNRAS*, **432**, 2573
- Willis, E. R., Garrod, R. T., Belloche, A., et al. 2020, *A&A*, **636**, 29
- Yang, B., Stancil, P. C., Balakrishnan, N., & Forrey, R. C. 2010, *ApJ*, **718**, 1062
- Yusef-Zadeh, F., Hewitt, J. W., Arendt, R. G., et al. 2009, *ApJ*, **702**, 178